UNIVERSITY OF CAPE TOWN

# Studies of the $W^{\pm}W^{\pm}$ scattering process in $pp$ collisions at the once and future ATLAS detector


*Author:*
Raynette VAN TONDER

*Supervisor:*
Dr. Sahal YACOOB

*Co-Supervisor:*
Dr. Andrew HAMILTON


*A thesis submitted in fulfilment of the requirements for the degree of Master in Science*

*in the*


UCT-ATLAS group
Department of Physics


September 1, 2017

# Declaration of Authorship

I, Raynette VAN TONDER, declare that this thesis titled, "Studies of the $W^{\pm}W^{\pm}$ scattering process in $pp$ collisions at the once and future ATLAS detector" and the work presented in it are my own. I confirm that:

- This work was done wholly or mainly while in candidature for a research degree at this University.
- Where any part of this thesis has previously been submitted for a degree or any other qualification at this University or any other institution, this has been clearly stated.
- Where I have consulted the published work of others, this is always clearly attributed.
- Where I have quoted from the work of others, the source is always given. With the exception of such quotations, this thesis is entirely my own work.
- I have acknowledged all main sources of help.
- Where the thesis is based on work done by myself jointly with others, I have made clear exactly what was done by others and what I have contributed myself.

Signed by candidate

Signed: Signature Removed

Date: 03.09.2017

*"She died a famous*
*woman denying*
*her wounds*
*denying*
*her wounds came from the same*
*source as her power"*

Adrienne Rich, Power

UNIVERSITY OF CAPE TOWN

# *Abstract*

Faculty of Science
Department of Physics

Master in Science

**Studies of the $W^{\pm}W^{\pm}$ scattering process in $pp$ collisions at the once and future ATLAS detector**

by Raynette VAN TONDER

This thesis investigates two topics, both concerning the rare Standard Model process known as $W^{\pm}W^{\pm}$ production. Firstly, this thesis considers the $W^{\pm}W^{\pm}$ production process at $\sqrt{s} = 13\,\text{TeV}$ with $L = 28\,\text{fb}^{-1}$ of data. Specifically, the $b$-tagged control region was examined, which tests the modelling of the non-prompt leptons originating from hadronic decays in a phase space where $t\bar{t} \rightarrow W^{+}W^{-}b\bar{b} \rightarrow l^{+}l^{-}\nu\nu b\bar{b}$ is the dominant process. Current studies of this control region are still ongoing for the Run II $W^{\pm}W^{\pm}jj$-EW analysis. In addition, this thesis investigates the prospects of a $W^{\pm}W^{\pm}$ measurement during the High-Luminosity Large Hadron Collider physics program with the upgraded ATLAS detector. The significance of the $W^{\pm}W^{\pm}$ measurement at $\sqrt{s} = 14\,\text{TeV}$ with an integrated luminosity of $L = 3000\,\text{fb}^{-1}$ was estimated to be at most 16.4 standard deviations. Furthermore, the gain in significance as well as the precision of the measurement of the cross section obtained with the extended tracking system are presented and compared with respect to the current coverage within $|\eta| \leq 2.7$. It is determined that the significance improves by 16% with the extension of the inner tracking system to include forward tracking for jets, electrons and muons up to a pseudorapidity of $|\eta| \leq 4.0$. In addition, the precision of the measurement of the cross section was estimated to be 5%, however this value can also be improved by 14% with the increased pseudorapidity coverage.

# *Acknowledgements*

The completion of this thesis would not have been possible without the insights and encouragement of various individuals and groups, whom I would like to thank.

Firstly, I would like to express my sincerest gratitude to my supervisors, Dr. Sahal Yacoob and Dr. Andrew Hamilton. Sahal, thank you for your guidance, advice and for teaching me the necessary skills for this research. I would also like to thank you for your useful feedback on all my research endeavours. Andrew, thank you for your enthusiastic particle physics lectures during undergrad and patient guidance during this research. Informal chats with you convinced me not to pay any heed to the voices of other people and to continue studying physics. I also extend special thanks to Dr. Claire Lee for working with me on the High-Luminosity studies. Your GIF responses to e-mails brightened my days.

Furthermore, I would like to thank my CERN summer internship supervisors, Dr. Alina Corso Radu and Dr. Isabel Trigger. As a summer student, I learnt an incredible amount topics concerning the day-to-day research activities at CERN. Notably, to think before a git commit and that the user's manuals for particle detectors really should have the phrase "don't panic" written somewhere.

To my lecturers at the UCT Physics Department, thank you for your patience, answering naive questions and handing over a box of tissues on some occasions. To my fellow students at the Physics Department, thank you for the silly moments of hilarity that made me burst out into uncontrolled laughter. I hope our worldlines cross again one day.

I would also like to take this opportunity to thank the University of Cape Town Postgraduate Funding Office for funding this research. In addition, I would like to show my appreciation for the SA-CERN collaboration for funding research trips to CERN and conferences, notably ATLAS Muon Week.

A multitude of completely unexpected events can, and will, occur during the course of one and a half years. I have learned that anything can be overcome, as long as somewhere in the world someone exists who can be called after midnight. I am fortunate to have several of these people in my life. Jean and Martin, thank you for the great company, good food and constant encouragement. Megan, Zubeida, Xolisile, Boreadi and Alexios, thank you for listening to late night rants and dragging me away from my desk for a proper cup of tea. You are my closest friends. I carry your hearts in mine.

Lastly, I would like to thank my parents, Lorette and Raymond, for support, care and weekly sanity-check phone calls throughout the course of my studies. To my dear Loraynne and Celeste, thank you for being the best little sisters someone could hope for. Finally, to my whole family, thank you for always believing in me and rooting for my success.

# Contents

# List of Figures

# List of Tables

# List of Abbreviations

| | |
|---|---|
| **BEH** | **B**rout-**E**nglert-**H**iggs |
| **CMS** | **C**ompact **M**uon **S**olenoid |
| **CR** | **C**ontrol **R**egion |
| **CSC** | **C**athode **S**trip **C**hamber |
| **ELisA** | **E**lectronic **l**ogbook for the **i**nformation **s**torage of **A**TLAS experiment |
| **EWK** | **E**lectro**wea**k |
| **FEB** | **F**ront-**e**nd **B**oard |
| **FTK** | **F**ast **T**rac**K**er |
| **HL-LHC** | **H**igh-**L**uminosity **LHC** |
| **HV** | **H**igh **V**oltage |
| **ID** | **I**nner **D**etector |
| **ITk** | **I**nner **T**rac**k**er |
| **LHC** | **L**arge **H**adron **C**ollider |
| **LO** | **L**eading **O**rder |
| **MC** | **M**onte **C**arlo |
| **MDT** | **M**onitored **D**rift **T**ube |
| **mis-ID** | mis-**id**entification |
| **MM** | **M**icro**m**egas |
| **MS** | **M**uon **S**pectrometer |
| **MVC** | **M**odel-**V**iew-**C**ontroller |
| **NLO** | **N**ext-to-**l**eading-**o**rder |
| **NSW** | **N**ew **S**mall **W**heel |
| **PDF** | **P**arton **D**istribution **F**unction |
| **PS** | **P**roton **S**ynchrotron |
| **QCD** | **Q**uantum **C**hromo**d**ynamics |
| **QED** | **Q**uantum **E**lectro**d**ynamics |
| **QFT** | **Q**uantum **F**ield **T**heory |
| **QGC** | **Q**uartic **G**uage **C**oupling |
| **RPC** | **R**esistive **P**late **C**hamber |
| **SA** | **S**ystem **A**ffected |
| **SCT** | **S**emi-**C**onductor **T**racker |
| **SM** | **S**tandard **M**odel of Particle Physics |
| **sTGC** | **s**mall-strip **T**hin **G**as **C**hamber |
| **SW** | **S**mall **W**heel |
| **TGC** | **T**riple **G**auge **C**oupling |
| **tgc** | **T**hin **G**ap **C**hamber |
| **TRT** | **T**ransition **R**adiation **T**racker |
| **VBS** | **V**ector **B**oson **S**cattering |

*Aan Lenie, my liewe oumagrootjie.*
*Om jou te kon geken het was ′n eer en ′n voorreg.*

# Chapter 1

# Introduction

An interesting feature arises with the calculation of the longitudinal scattering amplitude for the WW scattering process. In the absence of a Standard Model (SM) Higgs boson, the scattering amplitude grows as a function of centre of mass energy squared until unitarity is eventually violated at approximately $1\,\mathrm{TeV}$ [1] [2] [3]. The longitudinal WW scattering amplitude can be regulated with the addition of a Higgs scalar if and only if the recently discovered Higgs boson is indeed the Higgs boson predicted by the SM [4]. Vector Boson Scattering (VBS) therefore provides a unique window to study the nature of the mechanism of electroweak symmetry breaking and is also a promising process to probe resonances beyond the SM.

One of the best channels to investigate VBS is same sign W boson scattering [5]. This incredibly rare SM process has a unique experimental signature and is characterised by the presence of two high energy forward jets and a lepton pair of the same electric charge. Both ATLAS and CMS reported evidence of this rare SM process by studying proton-proton collision data at $\sqrt{s} = 8\,\mathrm{TeV}$ in 2014. ATLAS measured the cross section for electroweak $W^{\pm}W^{\pm}jj$-EW production was measured to be $\sigma = 1.3 \pm 0.4\,\mathrm{fb}$ at a significance level of 3.6 standard deviations [6] [7], while CMS measured $\sigma = 4.0^{+2.4}_{-2.0}\,\mathrm{fb}$ at an observed significance level of 2 standard deviations [8]. More recently, CMS reported another measurement with proton-proton collision data at $\sqrt{s} = 13\,\mathrm{TeV}$. The measured cross section for this study was found to be $\sigma^{fid} = 3.83 \pm 0.66\,\mathrm{fb}$ with a observed significance of 5.5 standard deviations [9]. On the other hand, the ATLAS analysis of the $W^{\pm}W^{\pm}jj$-EW measurement is still in the process of validating the measurement. The aim of the current analysis is to make use of data from $pp$ collisions at a higher centre of mass energy than the previous study and observe an excess of data events over the expected background processes at a significance level of 5 standard deviations, which would provide corroborative evidence for same sign W boson scattering.

Since it is still unclear whether the Higgs boson fully unitarizes the WW longitudinal scattering amplitude at high energies or whether other physics processes are involved [1] [2] [3], the study of the $W^{\pm}W^{\pm}jj$-EW process is an important task that will be refined during later runs of the Large Hadron Collider (LHC) through to the High-Luminosity LHC (HL-LHC) physics program. Besides operating at an increased centre of mass energy of $14\,\mathrm{TeV}$, the HL-LHC will also produce an integrated luminosity of $L = 3000\,\mathrm{fb}^{-1}$ of proton-proton collision data [10]. The increased radiation and pileup environment associated with the HL-LHC will result in occupancies and

radiation damage to sub-detector electronics beyond the nominal design values. To cope with this intense radiation environment several upgrades of the ATLAS sub-detectors have been scheduled, which coincides with the three long technical shutdowns of the LHC [11]. Particularly, the extension of the new Inner Detector tracker out to a pseudorapidity coverage of $|\eta| \leq 4.0$ will lead to the improved reconstruction of physics objects, thus greatly enhancing the future $W^{\pm}W^{\pm}jj$-EW measurement. This thesis studies the upgrade of the Muon Spectrometer and two topics related to the $W^{\pm}W^{\pm}jj$-EW process.

First, this thesis studies the upgrade of the Muon Spectrometer. In particular this thesis aims to provide a comprehensive assembly procedure for the assembly of small Thin Gap Chambers (sTGC) of the New Small Wheel (NSW). Since the assembly procedure for the assembly of these chambers has not yet been finalised, a proposed procedure that was developed as a summer student project at CERN through discussions with many experts will be outlined.

This thesis continues by investigating the current $W^{\pm}W^{\pm}jj$-EW analysis by making use of $28\,\mathrm{fb}^{-1}$ of proton-proton collisions data at a centre of mass energy of $\sqrt{s} = 13\,\mathrm{TeV}$ that was collected by the ATLAS detector during 2015 and 2016. Specifically, the $b$-tagged control region of the $W^{\pm}W^{\pm}jj$-EW process will be studied. This region is necessary to test the Monte Carlo (MC) and data-driven techniques used to model fake leptons originating from hadronic decays.

Lastly, this thesis investigates the prospects of a $W^{\pm}W^{\pm}jj$-EW measurement at the HL-LHC with a focus on an extended tracking system. In addition, the possibility of a forward muon-tagger attached to the New Small Wheels of the upgraded Muon Spectrometer, which will increase muon reconstruction capabilities out to a pseudorapidity coverage $|\eta| \leq 4.0$ is also considered. The gain in significance, precision of the measurement of the cross section, event yield and background suppression is reported with respect to the nominal tracking scenario in which the tracking system has a pseudorapidity coverage out to $|\eta| \leq 2.7$.

Chapters of this thesis are structured in the following manner. First, the foundational theoretical background concerning VBS will be discussed in Chapter 2. Chapter 3 gives a description of the LHC as well as the current ATLAS detector. Additionally, the reconstruction algorithms used by ATLAS to identify candidate physics particles will also be introduced. Next, Chapter 4 will briefly discuss the upgrades of the LHC toward the HL-LHC, as well as the upgrades of the ATLAS sub-detectors that will be affected the most by the high radiation and pileup environment. However, the upgrade of the Muon Spectrometer's Small Wheels will rather be described in Chapter 5. The main focus of this chapter will be the construction and assembly of the sTGC chambers for the NSW. Furthermore, Chapter 6 examines the current $13\,\mathrm{TeV}$ analysis of the measurement $W^{\pm}W^{\pm}jj$-EW measurement with a focus on studies concerning the $b$-tagged control region of this analysis. Afterwards, Chapter 7 will then investigate the prospect of a $W^{\pm}W^{\pm}jj$-EW measurement at the HL-LHC using simulated data with a

centre of mass energy of $14\,\mathrm{TeV}$. Investigations will focus mainly on the extension of the Inner Detector tracker to the forward regions of the ATLAS detector, however the effect of a very forward muon-tagger is also examined. Lastly, the final chapter provides a summary of the investigations and results obtained in this thesis.

Additional material relating to the assembly of sTGC chambers as well as the $W^{\pm}W^{\pm}jj$-EW measurement at the HL-LHC is given in Appendix A and B, respectively. Lastly, Appendix C describes the implementation of a logbook based on ELisA for the private usage of the Fast TracKer (FTK) sub-system. This summary was also completed as a CERN summer student project.

# Chapter 2

# Theoretical Background

The SM of Particle Physics is one of the most successful and widely accepted theories in physics. This theory aims to describe all elementary particles in nature as well as their interactions. According to the SM, all matter consists of three kinds of elementary particles: quarks, leptons and the mediators for each interaction. These elementary particles form the basis of the SM, which combines quantum electrodynamics (QED) [12], the Glashow-Weinberg-Salam theory of electroweak processes [13] [14] [15] and quantum chromodynamics (QCD) [16] [17] by combining the principles of quantum mechanics and special relativity to formulate a renormalisable Quantum Field Theory (QFT) [18]. In addition, the electroweak symmetry is broken in the SM by the Brout-Englert-Higgs (BEH) mechanism to allow for massive vector bosons and fermions [19] [20] [21]. A renormalisable QFT does not yet exist for gravitation, it is therefore still unclear whether gravitation can be included in the current framework of the SM. Since the completion of this theory it has successfully met every experimental test, therefore any deviations from the model are expected to be small.

VBS is a useful process to study and may reveal possible deviations from the SM. This process has been identified as a promising process to investigate the nature of electroweak symmetry breaking. The best channel for VBS measurements is same sign W boson scattering: a rare SM process that has a distinctive experimental signature of a same electric charge lepton pair and two high energy forward jets. This chapter will summarise the SM and describe the theoretical formulations of the electroweak theory, followed by electroweak symmetry breaking and the BEH mechanism. The final section of this chapter will discuss VBS processes, different production mechanisms of VBS and how these processes occur at the LHC.

## 2.1 The Standard Model of Particle Physics

In the SM fundamental particles can be categorised according to their spin: fermions carry half integer spin and vector bosons carry integer spin. Fermions can further be divided into leptons and quarks. Leptons will only experience electroweak interactions, while quarks will experience both electroweak and strong interactions. Leptons and quarks can each be classified into three generations. Stable matter in everyday life consists of leptons and quarks of the first generation. On the other hand, particles of the second and third generations are unstable, since these particles have high masses and could decay into lighter, more stable, fermions. A classification of all known elementary particles is shown in Figure 2.1. Each vector boson acts

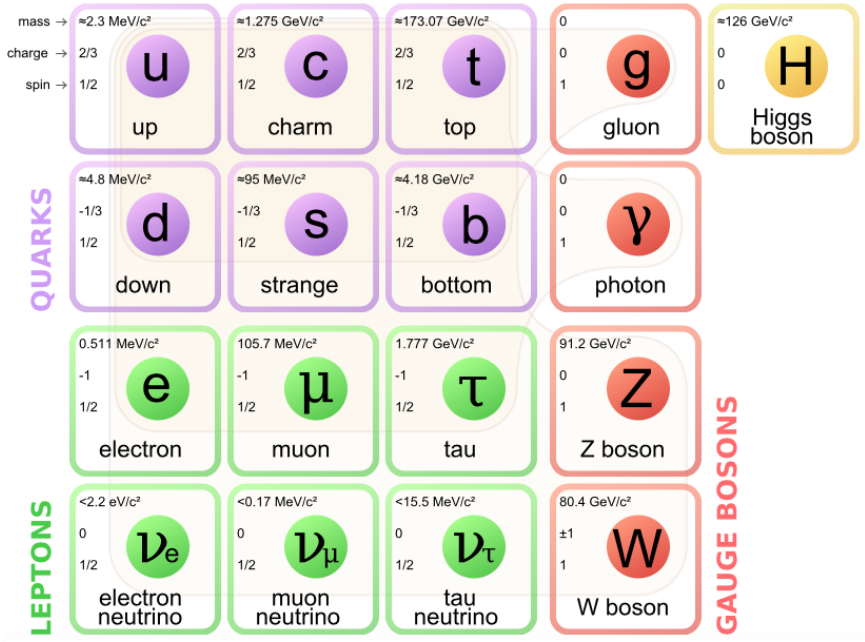


FIGURE 2.1: Classification of elementary particles in the Standard Model [22]. Fermions are divided into quarks (violet) and leptons (green), that can be further divided into three generations (columns). Vector bosons (red) are grouped together with the scalar Higgs (yellow). Each particle's mass, charge and spin is also given.

as a mediator for at least one of the fundamental forces: strong, electromagnetic and weak. A vector boson known as the gluon is the mediator for strong interactions, which are described by QCD. The charge that corresponds to QCD interactions is called colour charge and has three values: red, blue and green. Only particles that have a colour charge will partake in strong interactions, therefore the only particles that will interact strongly are quarks and gluons. On the other hand, only composite colourless particles will be experimentally observable. This infamous problem is known as confinement: a experimentally verified phenomenon where only colourless combinations of quarks and gluons can propagate freely, due to the fact that colour charged particles in free, unbound states have never been observed. Another concept introduced in QCD is asymptotic freedom, where quarks and gluons can become weakly interacting at small distance scales and high energies. Particles carrying electric charge will partake in electromagnetic interactions, which is mediated by the photon, $\gamma$, and described by the famously successful theory of QED. Lastly, the weak force is conveyed by W bosons and Z bosons, which acts on all left handed fermions. In contrast, the Higgs boson is a scalar with spin 0 and is not associated to any force. This boson will be discussed at length in the following sections of this chapter. Vector bosons, as well as the Higgs boson, have been summarised in Table 2.1.

The SM is a gauge theory [23] [24], which requires the SM Lagrangian to

TABLE 2.1: Vector bosons and the Higgs boson [31].

| **Particle** | **Interaction** | **Spin** | **Charge ($e$)** | **Mass (MeV)** |
|---|---|---|---|---|
| $\gamma$ | Electromagnetic | 1 | 0 | 0 |
| $g$ | Strong | 1 | 0 | 0 |
| $W^{\pm}$ | Weak | 1 | $\pm 1$ | $80.385 \pm 0.015$ |
| $Z$ | Weak | 1 | 0 | $91.1876 \pm 0.0021$ |
| $H$ | | 0 | 0 | $125.7 \pm 0.4$ |

be invariant under complex phase transformations of a set of global symmetries. Each global symmetry, by Noether's theorem [25], is connected to an underlying conservation law of nature. Therefore, symmetries such as rotations, translations in space and time and local frame invariance are related to conservation of momentum, space and angular momentum. The local symmetry group that describes the SM is given by:

$$SU(3)_C \times SU(2)_L \times U(1)_Y \tag{2.1}$$

where the strong interaction is represented by the $SU(3)_C$ symmetry group, the $C$ denoting colour charge, while the unified electroweak interaction is represented by the $SU(2)_L \times U(1)_Y$ symmetry group. The charges associated with the $SU(2)_L$ and $U(1)$ symmetries are known as weak isospin, $I_w$ and weak hypercharge, $Y_w$. This symmetry leads to the prediction of massless spin-1 vector bosons. Both mediators for the electromagnetic and strong interactions are indeed massless, however the mediators for the weak interaction, the W and Z bosons, are observed to be very massive. In order to accommodate these massive bosons the electroweak symmetry is spontaneously broken by the presence of a spin-0 field, which leads to the prediction of the Higgs boson.

Recently, a possible candidate for the Higgs boson, which exhibits properties that are consistent with the SM, have been observed by the ATLAS and CMS experiments at the LHC [26] [27]. In the following sections the theoretical formulations of the electroweak theory will be described, as well as electroweak symmetry breaking and the BEH mechanism. The content in the following section is a summary of descriptions found in [28], [29] and [30] and are discussed in much greater detail in these sources.

### 2.1.1 Electroweak theory

First developed by Glashow, Salam and Weinberg in the 1960s, the electroweak theory unified the electromagnetic and weak interactions into one single gauge theory with the symmetry group $SU(2)_L \times U(1)$. Associated with the fundamental representation of this symmetry group are four vector bosons. Three vector bosons, $W^{\mu} = (W^{\mu 1}, W^{\mu 2}, W^{\mu 3})$, are associated with $SU(2)$ and another vector boson, known as $B$, is associated with $U(1)$. Both charged currents (CC) and neutral currents (NC) of the electromagnetic and weak interactions are included in this theory. The weak CC interactions are mediated by the $W^{\pm}$ bosons, which are linear combinations of

the $W^{\mu 1}$ and $W^{\mu 2}$ vector bosons, while the electromagnetic and weak NC interactions, mediated by the photon and the Z boson, are linear combinations of the $W^3$ and $B$ vector bosons. The $W^1$ and $W^2$ bosons are combined linearly in order to represent the physical $W^{\pm}$ bosons in the following manner:

$$W_{\mu}^{\pm} = \frac{1}{\sqrt{2}}(W_{\mu}^{1} \mp iW_{\mu}^{2}). \tag{2.2}$$

The charged currents of the weak interaction will only act on left-handed chiral fermions, while the neutral currents will act on both left-handed and right-handed chiral fermions. With the exception of neutrinos that are always found to be left-handed, physical fermions are mixtures involving both chiralties. For each fermion, there is a weak isospin current, $j_{\mu} = (j_{\mu}^{1}, j_{\mu}^{2}, j_{\mu}^{3})$, that couples to $W^{\mu}$ with a dimensionless coupling constant of strength $g_{\omega}$. The weak charged current is giving by:

$$j_{\mu}^{\pm} = \chi_L \gamma_{\mu} \tau^{\pm} \chi_L \tag{2.3}$$

where $\chi_L$ is a left-handed fermion doublet and $\tau^{\pm}$ are $2 \times 2$ matrices consisting of a linear combination of two Pauli matrices. To ensure a full weak isospin symmetry, a third weak current is also defined:

$$j_{\mu}^{3} = \bar{\chi}_L \gamma_{\mu} \frac{1}{2} \tau^{3} \chi_L. \tag{2.4}$$

The neutral weak current, on the other hand, couples to the isosinglet, B, with a coupling constant of strength $\frac{g'}{2}$. Weak hypercharge is related to electric charge and the third component of weak isospin in the following manner:

$$j_{\mu}^{Y} = 2j_{\mu}^{EM} - 2j_{\mu}^{3} \tag{2.5}$$

where $j_{\mu}^{EM}$ is the electromagnetic current.

By making use of the two coupling constants, $g$ and $g'$, it can be shown that the two neutral states, $W^3$ and B, are mutually orthogonal linear combinations of the fields that mediate the electromagnetic and neutral currents. The neutral states mix in order to create two linear combinations: a massless combination corresponding to the photon, while the massive linear combination corresponds to the $Z^0$. The transformation can be expressed in terms of the two coupling constants, where the fields that mediate the electromagnetic and neutral currents can be denoted as A and Z, respectfully.

$$\begin{pmatrix} Z_{\mu} \\ A_{\mu} \end{pmatrix} = \frac{1}{\sqrt{g^2 + g'^2}} \begin{pmatrix} g & -g' \\ g' & g \end{pmatrix} \begin{pmatrix} W_{\mu}^{3} \\ B_{\mu} \end{pmatrix} \tag{2.6}$$

Equivalently, the transformation may also be expressed as a rotation through the weak mixing angle $\theta_w$, which has been experimentally determined to be approximately $29^{\circ}$.

$$\begin{pmatrix} Z_{\mu} \\ A_{\mu} \end{pmatrix} = \begin{pmatrix} \cos\theta_{\omega} & -\sin\theta_{\omega} \\ \sin\theta_{\omega} & \cos\theta_{\omega} \end{pmatrix} \begin{pmatrix} W_{\mu}^{3} \\ B_{\mu} \end{pmatrix} \tag{2.7}$$

To remain consistent, the unification of the unified electroweak theory with ordinary QED requires that the coupling constants for the charged and neutral currents must be related to the weak mixing as follows:

$$g' = g \tan \theta_\omega \tag{2.8}$$

Using the above-mentioned formulations it is possible to express the interaction Lagrangian for the electroweak theory as:

$$\mathcal{L} = \frac{g}{\sqrt{2}}(j_\mu^- W_+^\mu + j_\mu^+ W_-^\mu) + \frac{g}{\cos\theta_\omega}(j_\mu^3 - \sin^2\theta_\omega j_\mu^{EM}) Z^\mu + g \sin\theta_\omega j_\mu^{EM} A^\mu \tag{2.9}$$

where the terms in this fundamental expression represent, in order, the charged current weak interaction, the neutral current weak interaction and the electromagnetic interaction. Since the final term in the Lagrangian corresponds to the electromagnetic interaction, the constant coefficient of this term should be related to the electric charge. Therefore, the weak mixing angle can be related to the electric charge:

$$g \sin\theta_\omega = \frac{q_e}{\sqrt{\epsilon_0 \frac{hc}{\sqrt{2\pi}}}}. \tag{2.10}$$

With this expression the weak and the electromagnetic interactions have been unified, however the problem of the massive $W^\pm$ and $Z^0$ bosons has still not been solved. The electroweak theory further complicates matters by having different hypercharges for left-handed and right-handed fermions, as well as only left-handed fermions being charged under the $SU(2)_L$ symmetry. However, in order for fermion mass terms to be gauge invariant the transformations of left-handed and right-handed fermions are required to be the same. By requiring the SM Lagrangian to be invariant under transformations of the electroweak symmetry group, fermions are effectively required to be massless! For the massive bosons and fermions to be consistent with the Standard Model, a mechanism is necessary that would break the symmetry of $SU(2)_L \times U(1)$. Since the photon is massless, this mechanism is also required to keep the $U(1)$ symmetry of the electromagnetic interaction intact. The mechanism that solves the above-mentioned issues is known as the BEH mechanism and will be discussed in the following section, which is a summary of the content described in [31], [30] and [28].

### 2.1.2 Spontaneous electroweak symmetry breaking

In the SM, the electroweak symmetry $SU(2)_L \times U(1)$ is broken by the BEH mechanism, which introduces a new, complex scalar field, $\Phi$, with a potential of $V(\Phi)$ [19] [20] [21]. This scalar field transforms as a self-interacting doublet under $SU(2)_L$ with four real degrees of freedom. The scalar field and its potential are shown in Equations 2.11 and 2.12.

$$\Phi = \begin{pmatrix} \phi^+ \\ \phi^0 \end{pmatrix} = \frac{1}{\sqrt{2}} \begin{pmatrix} \phi_1 + i\phi_2 \\ \phi_3 + i\phi_4 \end{pmatrix} \tag{2.11}$$

$$V(\Phi) = -\frac{1}{2}\mu^2(\phi^*\phi) + \frac{\lambda^2}{4}(\phi^*\phi)^2 \tag{2.12}$$

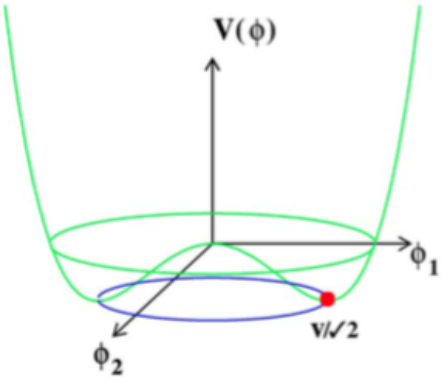


FIGURE 2.2: The BEH potential as a function of $\phi_1$ and $\phi_2$. The blue circle indicates the minima of this potential, located on a circle of radius $\mu/\lambda$. The ground state of this potential is located in the valley and the red dot indicates the choice of gauge [32].

When the quadratic term in this scalar potential is negative, the neutral component of the scalar doublet acquires a non-zero vacuum expectation value (VEV), as stated in [31]. The potential function is shown in Figure 2.2, where it can be seen that the minima of this potential function occur on a circle of radius $\frac{\mu}{\lambda}$ in $\phi$ space. The non-zero expectation value is shown in Equation 2.13, where $\nu = \sqrt{\mu^2/\lambda}$.

$$\Phi_0 = \frac{1}{\sqrt{2}} \begin{pmatrix} 0 \\ \nu \end{pmatrix} \tag{2.13}$$

By expanding about the vacuum expectation value of the field, the perturbations can be viewed as excitations of the particle field.

$$\Phi_0 = \frac{1}{\sqrt{2}} \begin{pmatrix} 0 \\ \nu + H \end{pmatrix} \tag{2.14}$$

where $H = H(x)$ is a real-valued scalar field representing the physical Higgs boson and $H(x) = 0$ is the ground state of the potential. The kinematics and interactions of the scalar field $\Phi$ is described by the Lagrangian

$$\mathcal{L} = \frac{1}{2}(D_\mu \phi)^*(D^\mu \phi) + \frac{1}{2}\mu^2(\phi^*\phi) - \frac{\lambda^2}{4}(\phi^*\phi)^2 \tag{2.15}$$

Assigning the particular ground state shown in Equation 2.14, the SM symmetry of $SU(3)_C \times SU(2)_L \times U(1)_Y$ is broken into $U(1)_{em}$. This effect is known as spontaneous symmetry breaking, since the symmetry of the Lagrangian in Equation 2.15 is not respected by a particular ground state of the system. It is caused when a system tends to its lowest energy state without any external influence, hence "spontaneous". Of the four degrees of freedom associated with the $SU(2)_L \times U(1)_Y$ gauge group, three are spontaneously broken. This implies that these three bosons have non-trivial transformations of the ground state and indicate the existence of three massless scalar particles, known as Goldstone bosons. The existence of one or more

Goldstone bosons is a general phenomenon that always accompanies spontaneous symmetry breaking of a continuous global symmetry [33] [34].

The Higgs field couples to the $W_\mu$ and $B_\mu$ gauge bosons associated with the electroweak symmetry group through the covariant derivative [31]:

$$D_\mu = \left(\partial_\mu + i\frac{g}{2}\sigma^a W_\mu^a + i\frac{g'}{2}YB_\mu\right)\Phi \tag{2.16}$$

where $g$ and $g'$ are the gauge couplings for the $SU(2)$ and $U(1)$ groups and $\sigma^a$, $a = 1, 2, 3$ are the Pauli matrices. As a result the neutral and two charged massless Goldstone degrees of freedom mix with the corresponding broken generators of $SU(2)_L \times U(1)_Y$ and become the longitudinal polarisation modes of the physical vector bosons, Z and W, stated in [31]. The fourth generator remains unbroken, since it is associated with the unbroken gauge symmetry of $U(1)_{em}$ and corresponds to the massless photon. Therefore, from the initial four degrees of freedom of the BEH field, two are absorbed by the $W^\pm$ vector bosons and another one is absorbed by the Z vector boson that become massive, as seen in Equations 2.17 and 2.18, respectively.

$$M_W^2 = \frac{g^2\nu^2}{4} \tag{2.17}$$

$$M_Z^2 = \frac{\left(g'^2 + g^2\right)^2}{\nu}\, 4 \tag{2.18}$$

The final remaining degree of freedom is the physical Higgs boson, a new scalar particle. The Higgs boson is neutral under electromagnetic interactions and transforms as a singlet under the $SU(3)_C$ symmetry, as stated by [31]. The mass of the SM Higgs boson is given by Equation 2.19, where $\lambda$ is the Higgs self-coupling parameter in $V(\Phi)$.

$$m_H = \sqrt{2\lambda}\nu \tag{2.19}$$

The mechanism of electroweak symmetry breaking is closely related to the scattering of massive vector bosons, since it regulates the longitudinally polarised scattering amplitudes of massive vector bosons at high energies and avoids the violation of unitarity in the scattering amplitudes. Therefore, vector boson scattering is a promising process to study the nature of electroweak symmetry breaking. The following section will introduce VBS processes and will also demonstrate the important role that the Higgs boson plays in these processes.

## 2.2 Vector Boson Scattering

The scattering of massive electroweak vector bosons, $VV \to VV$ with $V = W$ or $Z$, is closely related to the mechanism of electroweak symmetry breaking, since the longitudinal polarisation modes of these massive electroweak vector bosons correspond to the Goldstone modes of the broken symmetry [35]. An interesting feature arises with the calculation of the scattering amplitude for WW scattering. In the absence of a SM Higgs boson, the longitudinal polarised scattering amplitude grows as a function of centre-of-mass

energy squared and violates perturbative unitarity at $\sqrt{s} \approx 1\,\text{TeV}$ [1] [2] [3]. With the addition of a Higgs scalar the scattering amplitude of these processes can be regulated at high energies, restoring unitarity, only if the recently discovered Higgs boson behaves as the SM Higgs boson [4]. One type of VBS, W boson scattering, is therefore a process of great interest since the process is linked to the mechanism of electroweak symmetry breaking. In order to demonstrate the unitarity violation of VBS at high energies, the scattering amplitude of the $W^+W^- \to W^+W^-$ process will be discussed as an example, which is a summary of the calculations found in [36] and [37], where the scattering amplitude for this process have been discussed in greater detail.

First, begin by considering the derivation of a covariant form for the longitudinal polarisation 4-vector $\epsilon_L^\mu(p)$ of the W boson, where the leading term is proportional to $p^\mu/m_W$. It can be written as:

$$\epsilon_L^\mu(p) = p^\mu/m_W + \nu^\mu(p) \tag{2.20}$$

where

$$\nu^\mu(p) \simeq -\frac{m_W}{2p^{02}}(p^0, \vec{p}) \sim \mathcal{O}(m_W/E_W). \tag{2.21}$$

Note that the above-mentioned form of $\nu^\mu$ is not covariant. Next, consider the centre of mass frame for the incoming $W^+(p_1)W^-(p_2)$ pair with $\vec{p_1} = -\vec{p_2}$, where $\nu^\mu(p)$ can be expressed as:

$$\nu^\mu(p_1) = -\frac{2m_W}{s}p_2^\mu. \tag{2.22}$$

Likewise, the longitudinal polarisation 4-vector $\epsilon_L^\mu(p_1)$ can be expressed in the following manner:

$$\epsilon_L^\mu(p_1) = \frac{p_1^\mu}{m_W} - \frac{2m_W}{s}p_2^\mu \tag{2.23}$$

and just in the same way,

$$\epsilon_L^\mu(p_2) = \frac{p_2^\mu}{m_W} - \frac{2m_W}{s}p_1^\mu \tag{2.24}$$

in which $s = (p_1 + p_2)$. To obtain the covariant form for the polarisation vectors of the outgoing $W^+(k_1)W^-(k_2)$ pair, simply make the substitution of $(p_1, p_2) \to (k_1, k_2)$.

VBS processes must include quartic gauge coupling vertices, triple gauge coupling vertices, as well as the Higgs exchange and Higgs boson production vertices. The leading order Feynman diagrams contributing to VBS processes are shown in Figure 2.3. Furthermore, by substituting the form of the longitudinal polarisation vectors into the scattering amplitudes for each of these individual contributions, the leading terms of order $\mathcal{O}(E^4/m_W^4)$ for each of the scattering amplitudes can be shown to be:

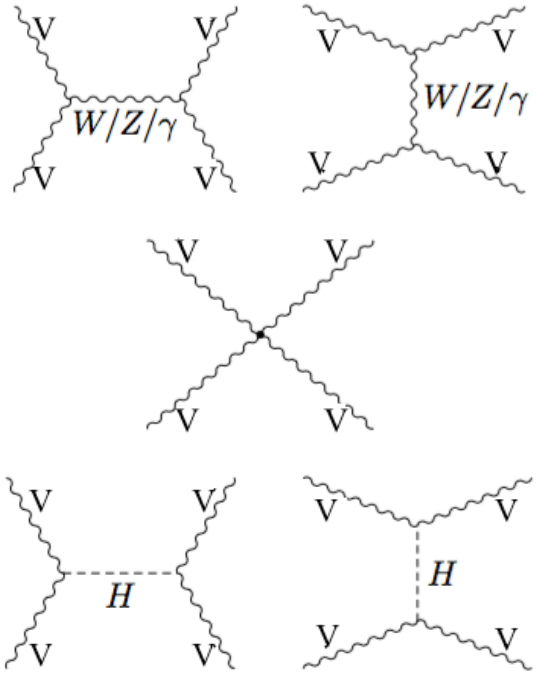


FIGURE 2.3: Leading order Feynman diagrams contributing to VBS processes. The $s$ and $t$ channels for Triple Gauge Couplings (top row), Quartic Gauge Couplings (middle row) and processes involving the Higgs boson (bottom row) are shown.

$$i\mathcal{M}^{s}_{TGC} = -i\frac{g^2}{4m_W^4}[s(t-u) - 3m_W^2(t-u)], \tag{2.25}$$

$$i\mathcal{M}^{t}_{TGC} = -i\frac{g^2}{4m_W^4}\left[t(s-u) - 3m_W^2(s-u) + \frac{8m_W^2}{s}u^2\right], \tag{2.26}$$

$$i\mathcal{M}_{QGC} = i\frac{g^2}{4m_W^4}\left[s^2 + 4st + t^2 - 4m_W^2(s+t) - \frac{8m_W^2}{s}ut\right], \tag{2.27}$$

$$i\mathcal{M}_{Higgs} = -i\frac{C_\nu^2 g^2}{4m_W^4}\left[\frac{(s-2m_W^2)^2}{s-m_h^2} + \frac{(t-2m_W^2)^2}{t-m_h^2}\right]. \tag{2.28}$$

Where the quantities $s$, $u$ and $t$ are Mandelstam variables [38]. A scale factor, $C_\nu^2$, has been added in the term involving contributions from the Higgs boson, which must be set to be 1 in the SM. The terms of the $s$-channel and $t$-channel for the TGC contributions can be combined to obtain

$$i\mathcal{M}_{TGC} = -i\frac{C_\nu^2 g^2}{4m_W^4}\left[s^2 + 4st + t^2 + 3m_W^2 t - 5m_W^2 s + 8m_W^2\frac{t^2}{s}\right] \tag{2.29}$$

which can be summed to the terms involving the QGC contributions to obtain terms proportional to $\mathcal{O}(E^2/m_W^2)$.

$$i\mathcal{M}_{TGC} + i\mathcal{M}_{QGC} = i\frac{g^2}{4m_W^2}(s+t) + \mathcal{O}\left(\left(\frac{s}{m_W^2}\right)^0\right). \tag{2.30}$$

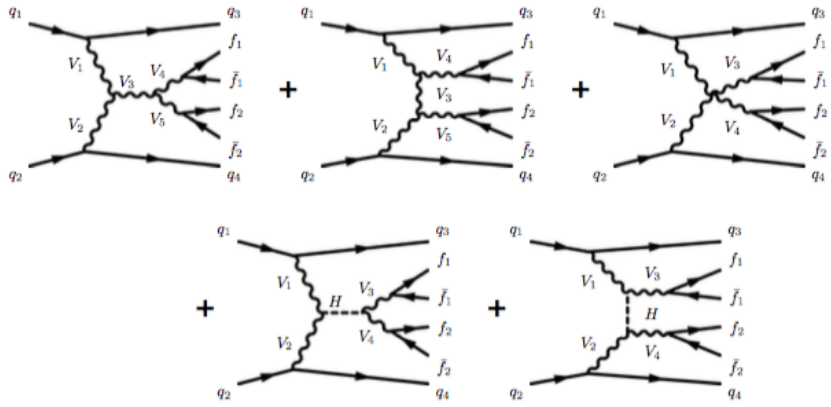

FIGURE 2.4: Representative Feynman diagrams of $VVjj$-EW production. The VBS scattering topology includes either a triple gauge coupling vertex, the t-channel exchange, a quartic boson coupling vertex or a Higgs boson exchange in the s- or t-channels. The lines are labelled by quarks (q), vector bosons (V) and fermions (f) [6].

Without the contribution from the Higgs term, the scattering amplitude from Equation 2.30 would grow as a function of centre-of-mass energy squared $s$ and violates unitarity at $\sqrt{s} \approx 1\,\text{TeV}$. However, in the high energy limit of $s \gg m_h^2, m_W^2$ Equation 2.28 becomes

$$i\mathcal{M}_{Higgs} = -i\frac{C_\nu^2 g^2}{4m_W^4}(s+t) \tag{2.31}$$

which cancels out the term in Equation 2.30, leaving only an $\mathcal{O}((s/m_W^2)^0)$ dependence for the total scattering amplitude. Therefore, the terms increasing with rising energy cancel and leaves a constant term that doesn't violate unitarity, if and only if the Higgs boson behaves as the SM predicts and the scale factor $C_\nu^2$ is equal to exactly 1.

Studying these VBS processes is therefore essential to understanding electroweak symmetry breaking within the SM and can also be used to determine Higgs couplings to gauge bosons. The energy dependence of the VBS cross-section above the Higgs mass scale can be used to test whether the Higgs boson unitarizes the scattering amplitude of VBS processes fully or only partially [39]. Detailed studies of VBS processes will not only aid in gaining a more thorough understanding of the mechanism of electroweak symmetry breaking, but may also be sensitive to signatures of beyond SM physics [36] [40]. The following section will describe VBS at the LHC, which is a summary of discussions found in [6].

### 2.2.1 VBS processes at the LHC

At hadrons colliders like the LHC, VBS can be realised by vector bosons radiated off incoming proton beams, interacting with each other and then subsequently decaying. Multiple processes can produce the same final state of two vector bosons and two jets (VVjj), however it is possible to separate

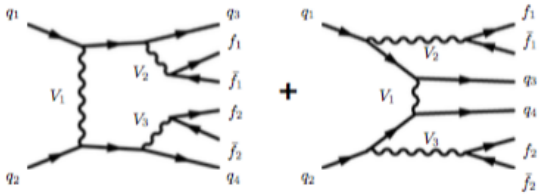

FIGURE 2.5: Representative Feynman diagrams of $VVjj$-EW production without the VBS topology. The lines are labelled by quarks (q), vector bosons (V) and fermions (f) [6].

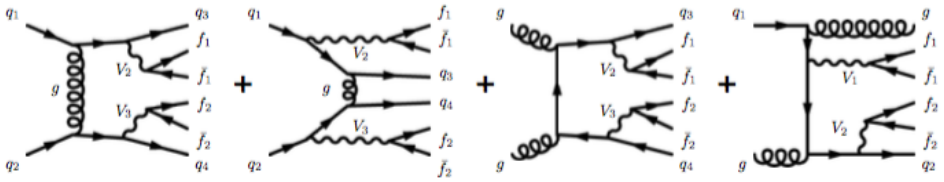

FIGURE 2.6: Representative Feynman diagrams of $VVjj$-QCD production. The lines are labelled by quarks (q), vector bosons (V), fermions (f) and gluons (g) [6].

VBS diagrams with this final state into two main groups: electroweak production consisting of only electroweak-interaction vertices ($VVjj$-EW) and strong production that includes at least one QCD-mediated vertex ($VVjj$-QCD) [6]. The electroweak production processes ($VVjj$-EW) contain purely electroweak mediated processes that are sixth-order in the expansion of the electroweak coupling constant $\alpha_{EW}(\mathcal{O}(\alpha_{EW}^6)$. The scattering of two electroweak bosons occurs via triple or quartic gauge vertices, the $s$- or $t$-channel exchange of a Higgs boson, or a W/Z boson. In addition, the $VVjj$-EW category also include a component of EW non-VBS processes with the same final state, however the two vector bosons do not scatter. Since VBS are not gauge invariant, non-VBS processes with the same final state must be included in the analysis to ensure gauge invariance [41]. On the other hand, the strong production processes contain diagrams that are fourth-order in electroweak interactions and second-order in strong interactions with the strong coupling, $\alpha_s(\mathcal{O}(\alpha_{EW}^4\alpha_s^2)$. These processes can include quark-quark or gluon-gluon scattering together with VV radiation or electroweak VV production. Interference between the QCD and EW mediated processes is expected to be constructive and increase the total cross section in the analysis regions. Representative Feynman diagrams of $VVjj$-EW production are shown in Figure 2.4, with non-VBS production shown in Figure 2.5 and $VVjj$-QCD production shown in Figure 2.6.

Since electroweak production involves the VBS processes of interest, processes must be studied where the strong production cross section does not dominate the electroweak production cross section. Depending on the final state of the VBS process, the relative ratio between electroweak and strong production can differ significantly. Making use of Sherpa [42], the leading-order (LO) production cross sections for $VVjj$-EW and $VVjj$-QCD can be

calculated and compared with different final states, shown in Table 2.2.

TABLE 2.2: Cross sections for electroweak and QCD-mediated VBS processes with different final states at $\sqrt{s} = 8$ TeV [43].

| **Final state** | **Process** | $VVjj$**-EW** | $VVjj$**-QCD** |
|---|---|---|---|
| $l^{\pm}\nu l'^{\pm}\nu' jj$ (same sign) | $W^{\pm}W^{\pm}$ | 19.5 fb | 18.8 fb |
| $l^{\pm}\nu l'^{\mp}\nu' jj$ (opposite sign) | $W^{\pm}W^{\mp}$ | 91.3 fb | 3030 fb |
| $l^{+}l^{-}\nu'\nu' jj$ | ZZ | 2.4 fb | 162 fb |
| $l^{\pm}l^{\mp}l'^{\pm}\nu' jj$ | $W^{\pm}$Z | 30.2 fb | 687 fb |
| $l^{\pm}l^{\mp}l'^{\pm}l'^{\mp}jj$ | ZZ | 1.5 fb | 106 fb |

Two possible processes may be used to study WW scattering: same sign WW scattering, $W^{\pm}W^{\pm}$, and opposite sign WW scattering, $W^{\mp}W^{\pm}$. Even though the predicted electroweak cross section for the opposite sign $W^{\mp}W^{\pm}$ process is far greater than the electroweak cross section for the same sign $W^{\pm}W^{\pm}$ process, the strong scattering cross section completely dominates the former process. On the other hand, the QCD contributions for the $W^{\pm}W^{\pm}$ process are very small. This is due to the fact initial states involving two LO gluons or a quark and a gluon are not present in the $W^{\pm}W^{\pm}$ process [44], which makes the electroweak and strong cross sections for this process roughly of the same order. Therefore, the $W^{\pm}W^{\pm}jj$ production process has the largest cross section ratio of electroweak to strong production [5]. Contributions from the s-channel exchange of a Higgs boson or a vector boson are not present in $W^{\pm}W^{\pm}$ electroweak production, while the t-channel Higgs contribution is allowed and guarantees unitarity for the VBS process. The excellent signal-to-background ratio together with the unique experimental signature of same sign $W^{\pm}W^{\pm}$ scattering, which greatly reduces the Standard Model background processes, makes this process one of the best channels for studying VBS processes at the Large Hadron Collider [45].

# Chapter 3

# The current ATLAS Detector at the LHC

In order to investigate the SM Higgs boson, test the SM and perhaps discover physics beyond the SM, one of the most powerful and largest accelerators in the world has been built. This huge accelerator was commissioned by the European Organisation for Nuclear Research (CERN) and is known as the Large Hadron Collider (LHC). The LHC ring is $27\,\mathrm{km}$ in circumference and is located $100\,\mathrm{m}$ below the Swiss-Franco border, near Geneva [46]. It was designed to collide proton-proton (p-p), as well as lead nuclei (Pb-Pb) and proton-lead (p-Pb) beams. The design centre of mass energy for $pp$ collisions at the LHC is $14\,\mathrm{TeV}$. Two of these high-energy particle beams follow opposing trajectories in separate beam pipes and can collide at four locations around the accelerator ring, which correspond to the four main experiments at the LHC. Each of the experiments at the LHC will be described in the next section, followed by a description of the multi-accelerator complex implemented at the LHC. Next, the ATLAS detector and its main detector sub-system will be introduced, followed by the particle reconstruction and identification algorithms used by ATLAS.

## 3.1 The Large Hadron Collider

An overall view of the four main experiments at the LHC, ATLAS, ALICE, CMS and LHCb, is shown in Figure 3.1. ATLAS [47] and CMS [48] are general purpose detectors built to search for the existence of the Higgs boson, supersymmetry and dark matter candidates. In order for these experiments to verify each other's results, both detectors have complementary designs. ALICE [49] and LHCb [50] are dedicated experiments focussing on specific topics. ALICE studies heavy ion collisions to gain a better understanding of the Quark Gluon Plasma (QGP) –a state of matter where quarks and gluons become deconfined from hadrons and act as quasi-free particles [49]. LHCb has an asymmetrical shape optimised specifically for the detection of B hadrons [50] and focus on measuring CP violation. These measurements might aid in investigating the question of the asymmetry between matter and antimatter observed by cosmologists in the universe. In addition to the main experiments at the LHC, there are also two smaller experiments: TOTEM [51] and LHCf [52]. These experiments make use of detectors located in the forward regions along the beamline to carry out specialised research. TOTEM studies the total $pp$ scattering cross section as well as the proton sub-structure. The experiment provides essential data necessary for monitoring the luminosity at the LHC [51]. LHCf examines the similarities

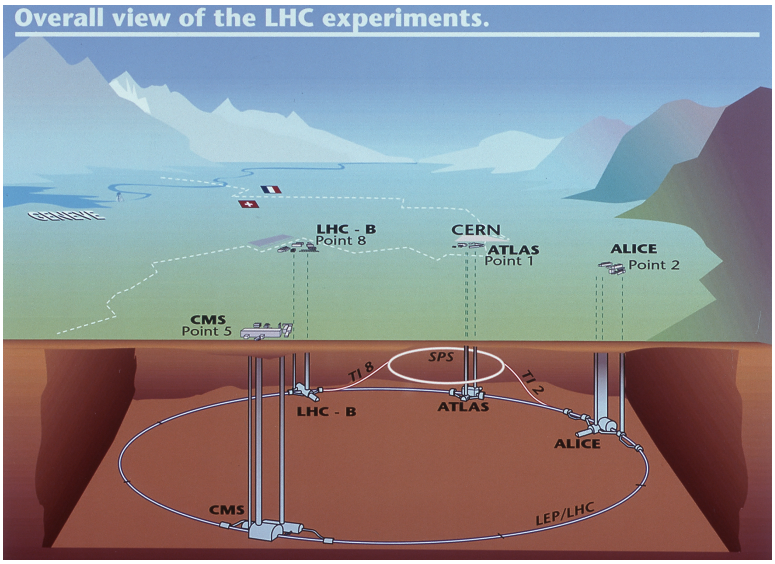


FIGURE 3.1: The four experiments at the LHC [53].

between cascades of particles triggered by cosmic rays in the upper atmosphere and the cascades of particles caused by collisions inside the LHC [52].

Installed inside the tunnel formerly used by the Large Electron-Positron (LEP) collider, the LHC is by design a synchrotron [54]. The synchrotron design not only limits the maximum beam energy of the LHC, but also requires the pre-acceleration of the injected particle beams to a specific energy. Therefore, a multi-stage accelerator complex is used to accelerate particle beams to specific energies at various stages of the process. The accelerator infrastructure at CERN is shown in Figure 3.2 and the following section describing the complex is a summary of [54]. Furthermore, the subsequent section on luminosity is a summary of the concepts described in [55] and [56].

Proton beams are accelerated by the electromagnetic fields inside 16 radio frequency (RF) cavities. Each of these RF cavities operates at a frequency of $400\,\mathrm{MHz}$. Beam paths are kept circular by making use of 1232 superconducting dipole electromagnets with a magnetic field of 8.4 Tesla, while the beams paths are also focussed with the aid of 390 quadrupole magnets. These electromagnets are made from superconducting niobium-titanium (NbTi) Rutherford cables and are kept at a temperature of about 1.9 Kelvin by superfluid helium.

The process begins by producing protons from hydrogen gas with an electric field, which ionises the hydrogen atoms. The proton nuclei beams are released into the Linear Accelerator (LINAC) and once $50\,\mathrm{MeV}$ has been reached, the beams are injected through a series of circular accelerators. The first stage is the Proton Synchrotron Booster (PSB) which accelerates protons to an energy of 1.4 Gev. Afterwards, proton beams are further accelerated to an energy of 25 GeV in the Proton Synchrotron (PS). At this

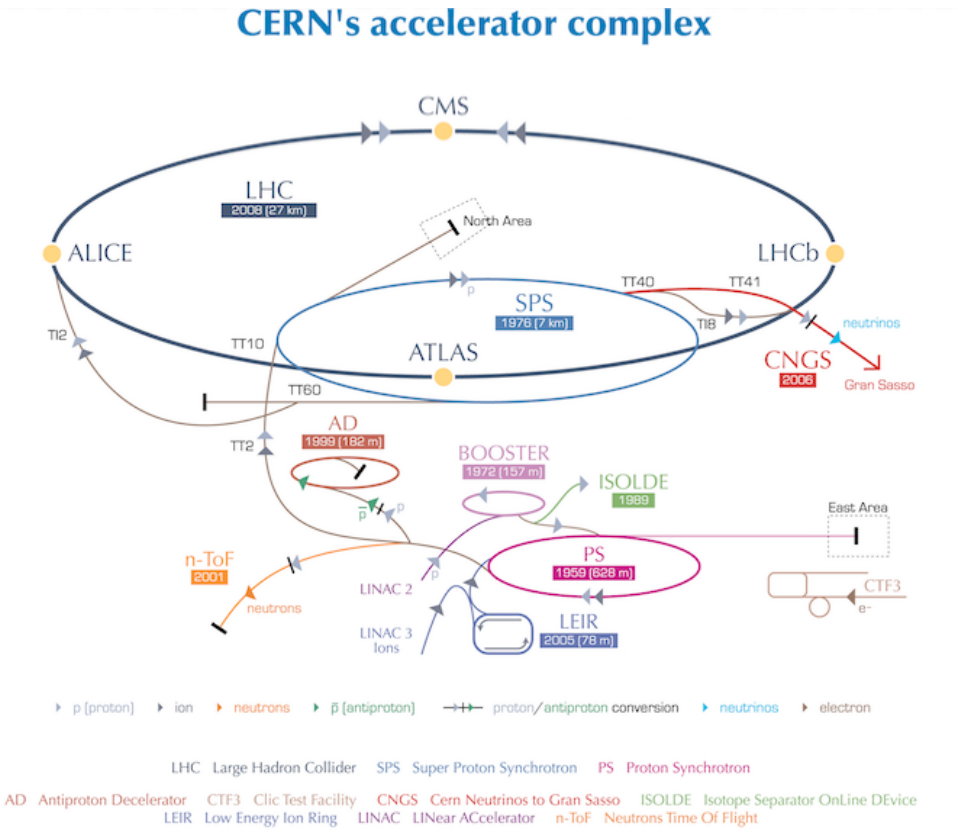


FIGURE 3.2: The accelerator complex at CERN [57].

stage of the complex, protons are ordered into discrete packets known as bunches due to the oscillating electric field inside the RF cavities. Beams leaving the PS are ordered into 72 bunches of protons with a duration of 4 ns and a spacing of 25 ns, which are then followed by 12 empty bunches. The final stage is known as the Super Proton Synchrotron (SPS). It increases the energy of the beam from the initial energy of 25 GeV to an approximate energy of 450 GeV after which, the proton beams are finally injected into the LHC where the final stage of acceleration will be done. Experimental halls are located between most of the pre-accelerators, since many experiments at CERN require beams at various lower energies.

An accelerator's energy and luminosity are the most important figures in experimental accelerator physics [55]. Notably, the LHC was designed to reach unprecedented high values for both its centre of mass energy and its luminosity. Usually divided into two types, instantaneous and integrated, luminosity is a measure of the number of collisions that occur at an interaction point of a particle collider. These two types of luminosities are useful to characterise the performance of the accelerator.

Instantaneous luminosity refers to the number of collisions per unit time, per cross sectional area, $\sigma$, and is therefore used to determine the intensity of the beam. Given a specific cross section for a process of interest, the rate

of interactions produced per second can be described by:

$$\frac{dN}{dt} = L\sigma. \tag{3.1}$$

The instantaneous luminosity for beam-beam collisions can be expressed in terms of beam parameters, assuming a Gaussian beam profile, as follows [56]:

$$L = \frac{N_b^2 n_p^2 f}{4\pi\sigma_x\sigma_y} S \tag{3.2}$$

where $N_b$ is the number of bunches per beam, $n_p$ the number of protons contained per bunch, $f$ is the frequency of revolution and $\sigma_x$ and $\sigma_y$ specify the beam widths in the transverse plane. $S$ is a geometric reduction factor which takes into account the non-zero crossing angle of the beams at the interaction point. The aim of the operation of a particle collider is to optimise the integrated luminosity, defined as the maximum luminosity. The total integrated luminosity may be obtained from the instantaneous luminosity from the following equation [56]:

$$L_{int} = \int_0^T L(t')dt' \tag{3.3}$$

where the integral is taken over the total amount of sensitive time, excluding possible periods of dead time. From these equations, one can see that the study of rare processes requires high overall luminosities.

The design luminosity of the LHC is of the order $10^{34}\,\mathrm{cm}^{-2}\mathrm{s}^{-1}$ which would provide 40 million $pp$ bunch crossings per second [54]. In 2015, the LHC reached a centre of mass energy of $13\,\mathrm{TeV}$ with proton bunches separated by $25\,\mathrm{ns}$ in time. Furthermore, the LHC machine not only reached a peak instantaneous luminosity of $L = 5 \times 10^{33}\,\mathrm{cm}^{-2}\mathrm{s}^{-1}$, but also delivered a total integrated luminosity of $4.2\,\mathrm{fb}^{-1}$. During 2016, a peak instantaneous luminosity of $L = 13.8 \times 10^{33}\,\mathrm{cm}^{-2}\mathrm{s}^{-1}$ was reached with a total integrated luminosity of $38.5\,\mathrm{fb}^{-1}$ [58].

## 3.2 The ATLAS Detector

The ATLAS detector is a multi-purpose detector designed to detect final state particles and their kinematics with incredibly high precision. It is the largest particle detector for collision experiments in the world and measures $45\,\mathrm{m}$ in length, $25\,\mathrm{m}$ in diameter and weighs approximately 7000 tonnes. Additionally, it consists of multiple components or sub-detectors that are specialised for the detection of different types of particles, as well as other specific roles in the detection process. The main components of the ATLAS detector are the inner tracking detectors, the calorimeter systems, the muon spectrometer and the trigger system. An overview of the ATLAS detector can be seen in Figure 3.3, which has been sliced such that each of the main components is visible. This section will first describe the ATLAS coordinate system, which is crucial for particle identification, followed by a brief

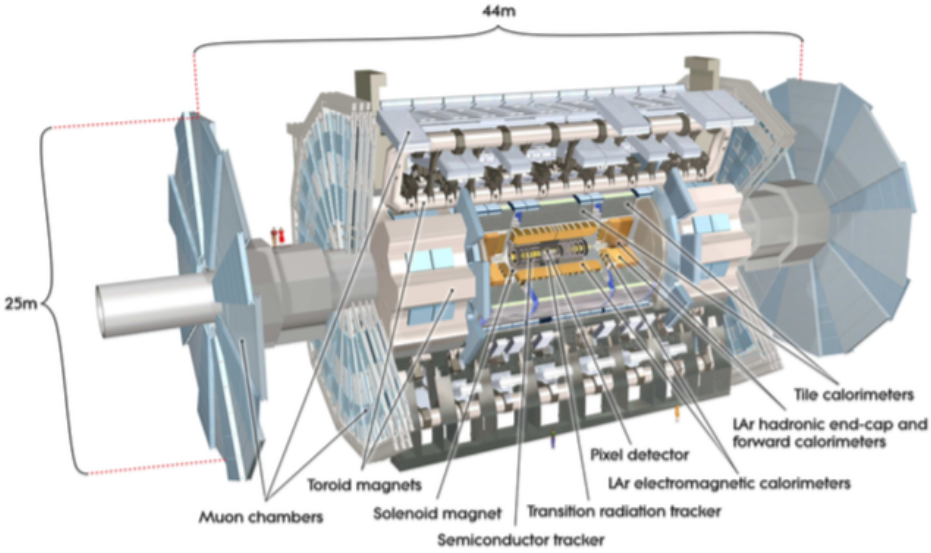


FIGURE 3.3: The ATLAS detector. [47].

summary of the main sub-detectors. The following sections are brief summaries based on the comprehensive descriptions of the ATLAS detector and its components found in [47].

### 3.2.1 The ATLAS Coordinate System

A right-handed coordinate system with the nominal interaction point taken as the origin is used within the ATLAS detector. The $x-$axis points from the interaction point towards the centre of the LHC ring, the $y-$axis points directly upwards and the $z-$axis points along the beam tunnel. Additionally, the side of the detector along the positive $z-$axis is referred to as the A-side, while the side along the negative $z-$axis is referred to as the C-side. The $x-y$ plane defines the transverse plane. Cylindrical coordinates are used in this plane, where the azimuthal angle, $\phi$, is measured relative to the positive $y-$axis around the $z$-axis. The polar angle, $\theta$, is defined in the $x-z$ plane and is measured from the positive $z-$axis with respect to the beam pipe. An illustration of the coordinate system can be seen in Figure 3.4.

It is often more convenient to use the rapidity between particles as a coordinate rather than a coordinate along the $z-$axis, since the momenta of the colliding beams for an event in the $z$-axis are hard to determine. Therefore, it is useful to define variables that are Lorentz invariant to boosts along the $z-$axis. Rapidity, defined in Equation 3.4, is a more useful variable to describe kinematics in hadron colliders, since differences in rapidity are Lorentz invariant.

$$y = 1/2 \ln[(E + p_x)/(E - p_z)] \tag{3.4}$$

In the case of the massless limit, in which the particle's mass is small compared to the particle's momentum, this equation can be approximated and simply becomes:

$$\eta = -\ln \tan \theta/2 \tag{3.5}$$

where $\eta$ denotes the pseudorapidity, which is the detector coordinate used along the $z$-axis. The angular separation between two objects can then be defined in the $\eta - \phi$ space as,

$$\Delta R = \sqrt{(\Delta\eta)^2 + (\Delta\phi)^2} \tag{3.6}$$

Defining the coordinate system in the above-mentioned manner makes it easier to determine the exact location of particles inside the ATLAS detector, as well as being useful for particle reconstruction.

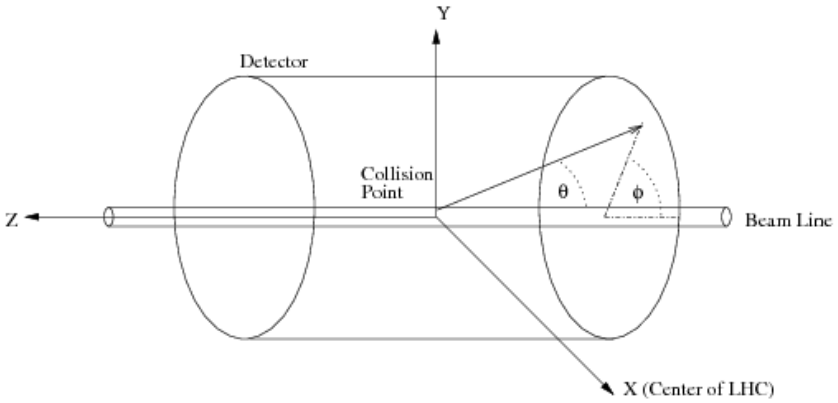


FIGURE 3.4: The ATLAS coordinate system [59].

### 3.2.2 Inner Detector

The Inner Detector (ID) measures tracks and momenta of charged particles within $|\eta| < 2.5$. This detector enables the reconstruction of tracks that have transverse momenta of $p_T > 500\,\mathrm{MeV}$ with high efficiency and resolution. An axial magnetic field of $2\,\mathrm{T}$ completely immerses the ID in a cylindrical envelope of $7\,\mathrm{m}$ in length, $2.3\,\mathrm{m}$ in diameter. The ID consists of three independent, but complementary components: the pixel detector, the Semi-Conductor Tracker (SCT) and the Transition Radiation Tracker (TRT).

Both the pixel detector and the SCT make use of semi-conductor technology to measure incident charged particles and photons. The pixel detector requires high granularity sensors due to its close proximity to the interaction point, as well as the design goal of reconstructing primary vertices. Arranged in three layers in the barrel region and three disks in the end cap region, the pixel detector has a total of 1744 sensors with each sensor containing 47232 pixels. Therefore, the total number of readout channels from the pixel detector is over 82 million! Moreover, the newly installed innermost layer of pixel detectors was operational for the first time during the 2015 data taking period [60]. The pixel layer has a transverse resolution of $10\,\mu\mathrm{m}$ and a longitudinal resolution $115\,\mu\mathrm{m}$. Located outside the pixel detector, the SCT makes use of silicon strips to cover a larger area. One SCT module has two sets of silicon micro-strip sensors. The SCT consists of a total of 4040 modules are arranged as four cylindrical layers in the barrel

region and nine disks in the end cap region. The SCT provides a longitudinal resolution of $580\,\mu\mathrm{m}$ and a transverse resolution of $17\,\mu\mathrm{m}$. Signals generated in the front-end electronics of the pixel detector and SCT are kept in a memory buffer for approximately $3.2\,\mu\mathrm{s}$.

The outermost layer of the ID is the TRT, which comprises straw tube detectors. These detectors measure the drift time of ionised charges caused by charged particles as they traverse through the straw. Each straw has a cathode tube with an anode wire in the centre, filled with a gas mixture of 70% Xe, 27% $CO_2$ and 3% $O_2$. Since transition radiation yields higher signal than minimum charged particles and the amount of transition radiation produced is inversely proportional to particles mass, transition radiator material fills the gaps between the straw tubes. As a result, these unique properties of transition radiation enable the TRT to distinguish electrons from other charged particles. The TRT only provides an transverse resolution to an accuracy of $130\,\mu\mathrm{m}$ and does not provide any information in the longitudinal direction.

### 3.2.3 Calorimeters

A calorimeter system provides identification and energy measurements for electrons, photons, hadronic jets and missing transverse energy within a range of $|\eta| < 4.9$. The two main calorimeters in the ATLAS calorimeter system are the electromagnetic and hadronic calorimeters. Both calorimeters make use of a sampling methodology based design, in which the detectors consist of absorber and active materials. Absorber materials are usually of high density and aid in particle shower development, while the active materials collect and measure the deposited energy. The electromagnetic calorimeter measures the energies of particles that interact electromagnetically. It makes use of liquid argon as an active material, interleaved with lead plates which serve as the absorber material. An overall accordion-shaped geometry chosen for the absorbers and active materials of the barrel and end cap electromagnetic calorimeters, ensures full coverage of $\phi$. Additionally, this accordion-shaped geometry also enables fast extraction of signal, while simultaneously providing information about the longitudinal evolution of the electromagnetic shower. The measured energy resolution of the EM calorimeter is $\frac{\sigma(E)}{E} = 10\%/\sqrt{E} \oplus 0.2\%$ and a spatial resolution of $50\,\mathrm{mrad}\sqrt{\mathrm{E}}$ in the $\eta$ plane [61].

The hadronic calorimeter measures the energies of particles that interact via the strong interaction. It consists of various calorimeters located in different regions of the detector: the tile calorimeter, the extended barrel calorimeter, the liquid argon hadronic calorimeter and the liquid argon hadronic forward calorimeter. Located in the barrel, the tile calorimeter covers a range of $|\eta| < 1$, while the extended barrel calorimeter covers a range of $0.8 < |\eta| < 1.7$. Both of the calorimeters located in the barrel region are instrumented with scintillator tiles and steel for the active material and absorber material, respectively. On the other hand, the liquid argon hadronic is located in the end cap region where it covers a range of $1.5 < |\eta| < 3.2$ and uses copper as an absorber material. Finally, extending the range up to $|\eta| < 4.9$, the forward calorimeter uses copper and tungsten as absorber

materials. Furthermore, the active material for both the end cap and forward calorimeters is liquid argon. The measured energy resolution for the tile calorimeter was determined to be $50\%/\sqrt{E} \oplus 3\%$ [62], while the measured energy resolution for the hadronic end cap calorimeter was found to be $21\%/\sqrt{E}$ for electrons and $70\%/\sqrt{E} \oplus 6\%$ for pions [63]. These measurements for the forward calorimeter was determined to be $29\%/\sqrt{E} \oplus 3.5\%$ for electrons and $70\%/\sqrt{E} \oplus 3\%$ [64].

The forward calorimeter determines missing transverse energy, but also records information for measurements of strongly interacting particles in the forward regions of the detector. A prominent example of these types of interactions is VBS processes.

### 3.2.4 Muon Spectrometer

Located in the outermost layer, the Muon Spectrometer (MS) defines the overall dimensions of the ATLAS detector. The MS consists of different detector modules located in the barrel and end cap regions of the detector, providing tracking capabilities for a near-continuous range of $|\eta|$. Markedly, the Monitored Drift Tube chambers and the Cathode Strip Chambers are responsible for precision measurements, coupled with Resistive Plate Chambers and Thin Gap Chambers serving as dedicated trackers. A magnetic field between $0.5 - 1\,\mathrm{T}$, provided by toroid magnets located in the barrel and end cap regions, completely surrounds the MS. Figure 3.5 shows a layout of the various components of the muon system. The ATLAS detector was designed to contain all other stable particles in the calorimeters. Therefore, only muons, due to their lifetime and higher mass, will reach the MS. Neutrinos will also traverse through the ATLAS detector with a negligible probability of interaction, however since these particles are neutral they are unlikely to interact with the MS system.

Monitored Drift Tube (MDT) provide precision measurements of muon tracks to a minimum threshold of $p_T > 3\,\mathrm{GeV}$. Three stations of MDT's are arranged in concentric cylinders in the barrel region and cover a range of $|\eta| < 1$. Similarly, another four stations are arranged as disks in the end cap regions with a range of $1 < |\eta| < 2.7$. MDT's are based on a similar concept as the TRT by making use of cathode tubes with an anode wire in the centre that is filled with a gas mixture (93% Ar and 7% $CO_2$). Muons traversing through the tube cause ionisations, which are consequently collected by the anode wire. Hence, the distance of the muon track from the central wire can then be determined by the drift time. The average resolution of a MDT chamber in the bending direction is approximately $25\,\mu\mathrm{m}$. In addition to the MDT's, Cathode Strip Chambers (CSC) also perform precision measurements and are arranged in two disks for each of the innermost end cap disks. The Cathode Strip Chambers (CSC) are located $7\,\mathrm{m}$ from the interaction point. Due to the proximity to the interaction point, CSC's require a faster time resolution and higher rate capability which enable these detectors to manage higher fluxes of particles. CSC's are multi-wire proportional gas detectors with a cathode strip readout. The chambers are filled with a gas mixture (80% Ar and 20% $CO_2$) and contain a mesh of parallel tungsten wires. These wires serve as the anodes, held at a potential of $1900\,\mathrm{V}$, and

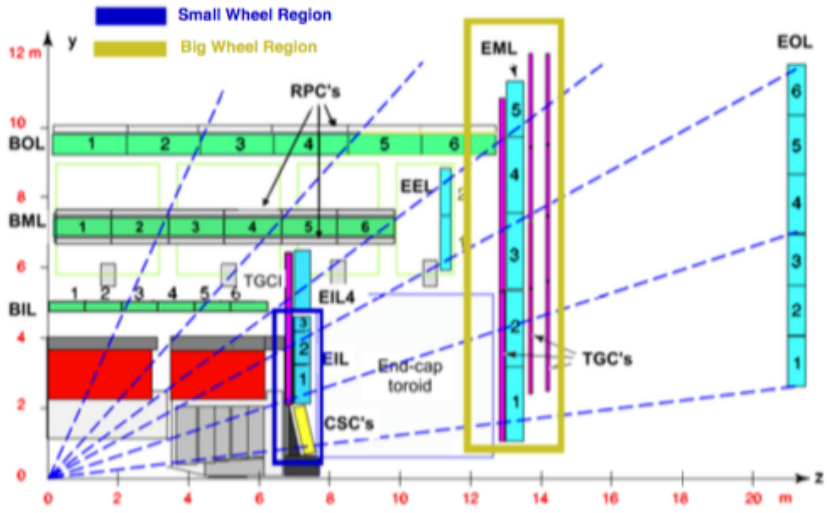


FIGURE 3.5: Layout of the a quarter muon system in the $y - z$ plane. The blue blocks indicate the MDT's located in the end cap region, while the green blocks indicate the MDT's located in the barrel region. Also marked on the plot are the CSC's, TGC's, RPC's and the Small and Big Wheel regions of the detector [65].

are surrounded by two parallel strips of cathodes. The disk is composed of small and large chambers with different readout pitches in the transverse and longitudinal directions resolutions. Therefore, the total overall resolution is $40\,\mu\mathrm{m}$ in the bending direction and $5\,\mathrm{mm}$ in the transverse direction.

The MS has two types of dedicated trackers at its disposal: Resistive Plate Chambers (RPC) located in the barrel region and Thin Gap Chambers (TGC) located in the end cap region. For the RPC and TGC, information is delivered to within $|\eta| < 1$ and $1 < |\eta| < 2.4$, respectively. As their name suggests, RPC's consist of two resistive plates with a gap of $2\,\mathrm{mm}$. The gap between the plates, which is filled with a gas mixture, is held at an uniform electric field. RPC's can reconstruct tracks up to $35\,\mathrm{GeV}$ with a spatial resolution of $10\,\mathrm{mm}$ in both the transverse direction and the bending direction. On the other hand, TGC's are also multi-wire proportional chambers and similar to CSC's. Their wires, however, are held at a much higher voltage of $2900\,\mathrm{V}$. In addition, the size of wire groups utilised to measure positions are varied between 6 and 31 wires in order to maintain good momentum resolution at higher $|\eta|$. The TGC chambers provide a trigger efficiency for a minimum ionising particle of 99% within a time window of $25\,\mathrm{ns}$.

### 3.2.5 Trigger system

At the design luminosity of the LHC, the period of proton bunch crossings will be $25\,\mathrm{ns}$ that will result in a collision rate of $40\,\mathrm{MHz}$. This is a tremendously large amount of data that can't be stored on a daily basis on disk. It should also be noted that not all collision events are interesting to physics analysis. Therefore, only events containing interesting physics processes should be kept. To quickly and efficiently decide whether an event is worth

recording, a trigger system consisting of a three level structure has been put in place.

The first level of the trigger system, L1, is completely hardware based. Only a fraction of the total detector information is used by the on-detector electronics, at a reduced granularity, to be able to make decisions in $2.5\,\mu$s. The L1 trigger searches specifically for signatures of muons, electrons, photons and jets with high transverse momentum. Furthermore, the L1 trigger also scans for $\tau$ leptons decaying into hadrons. Events with large missing or total transverse energy are also identified. At L1 trigger stage, the total nominal data-taking is reduced only to $75\,\mathrm{kHz}$.

The next level of the trigger system, L2, is software based and has the full event information at its disposal to investigate the regions of interest (RoI's), tagged by the L1 trigger. By only evaluating the RoI's, a fast processing time of $40\,\mathrm{ms}$ can be achieved at the L2 stage. After the L2 stage of the trigger system, the total amount of data has been reduced to $3.8\,\mathrm{kHz}$. The final stage of the trigger system is known as the Event Filter, which makes use of the offline reconstruction algorithms that will be discussed in the following section. The Event Filter also makes use of calibration and alignment measurements, as well as the current magnetic field map to increase the accuracy of reconstructed events. Consequently, the offline analysis is performed at an average of $4\,\mathrm{s}$ for each event and reduces the amount of data to $200\,\mathrm{Hz}$. After this final stage of the trigger system, the accepted events are sent to storage facilities before being made available for physics analysis.

Since the L1 trigger makes decisions with less information than the full offline event reconstruction, a trigger selection at the L1 stage at a specific energy may not be optimal. The probability of a physics object to be accepted at the L1 trigger level as a function of its energy is called the trigger efficiency, however trigger efficiencies for L2 and the Event Filter are also used. The trigger performance of the trigger system is demonstrated in [47].

## 3.3 Simulated Monte Carlo samples

To properly investigate possible new physics processes beyond the SM it is crucial to compare data measured by the ATLAS detector subsystems to theoretical predictions. This can be achieved by created simulated data samples based on the Monte Carlo (MC) procedure, hence the name of MC samples for simulated data [66]. These MC samples can also be used to reflect the response and performance of the current detector, by comparing well-understood predictions of SM processes with the estimations produced from full detector simulations.

Several MC generators are used to simulate data samples. Each of these generators have different properties, since different sets of parameters are used as inputs as well as making use of different generation methods. For

this reason, some generators are more suited to generate certain SM processes than other generators, while in some cases the use of different generators may even complement one another. The exact differences between generators and implementation of MC methods are beyond the scope of this thesis, the reader is referred to [67], [68] and [69] for detailed discussions. Commonly used multi-purpose MC generators are Sherpa [42], Pythia 6 [70] or 8 [71] [72], Herwigg++ [73], Madgraph [74] [75] and Whizard [76] [77]. Furthermore, MC generators that provide NLO calculations for specific processes are VBFNLO [78] and Powhegbox [79].

## 3.4 Particle reconstruction and identification

Many different kinds of particles can be produced in a $pp$ collision, however these particles cannot be observed directly. Only through different interactions with various components of the ATLAS detector can the type of particle and its kinematic properties be inferred. Some particles have short lifetimes and decay before they can reach any sensor components of the detector. Outgoing quarks and gluons become fragmented and hadronise, producing a conglomeration of particles with longer lifetimes. This means that only a finite range of stable particles can interact with various detector components. Final state particles leave very distinctive signatures, which allows reconstruction algorithms to read out the information from the detector components and build object candidates. Figure 3.6 shows the various ways that final state particles can interact with the ATLAS detector.

Electrons and photons interact in the electromagnetic calorimeter as electromagnetic showers, with the electron leaving a track in the inner detector. Protons will leave tracks in the inner detector and will then deposit a cluster of energy in the hadronic calorimeter. Neutrons deposit energy in the hadronic calorimeter as well, however they do not leave tracks in the inner detector. Since protons and neutrons are particles that are composite of quarks, these particles are usually identified as hadronic jets that are formed from the hadronisation of quarks and gluons. Muons will traverse the entire detector, leaving tracks in the inner detector, small energy deposits in the electromagnetic calorimeter and finally interact with the muon chambers. Neutrinos will also traverse the entire detector, however unlike muons, they will not interact with any of the detector components and will not leave any tracks. Neutrinos can therefore only be identified by examining the imbalance of transverse energy and momentum in events. The reconstruction algorithms used by ATLAS to identify the various abovementioned particles will be discussed in the following sections.

### 3.4.1 Tracks and vertices

Tracks are reconstructed by making use of hits in the inner detector and fitted with several variables, measured at the point of closest approach to the beamline. These variables are the track's radius of curvature, which can in turn be used to determine the charge-transverse momentum ratio ($q/p_T$), the polar and azimuthal angles and also the transverse and longitudinal impact parameters. The transverse and longitudinal impact parameters ($d_0$

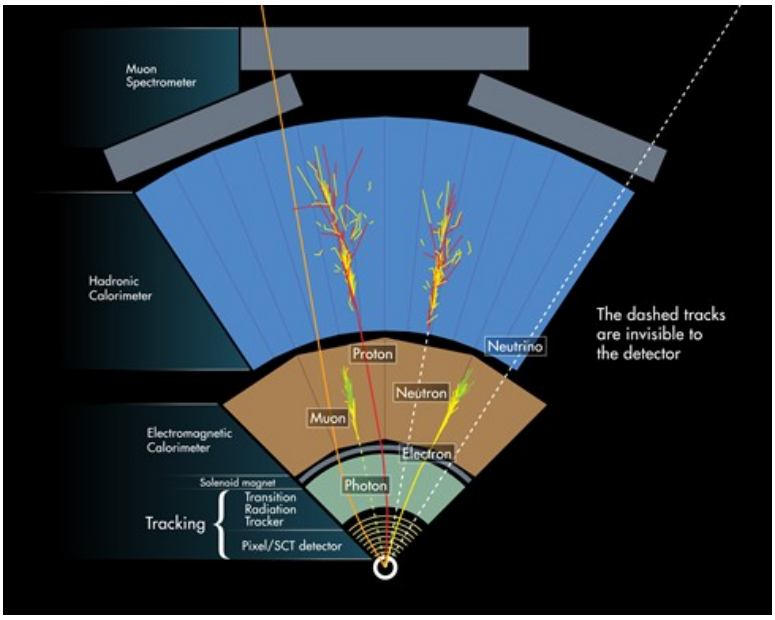


FIGURE 3.6: Different stable particles interacting with the ATLAS detector [80].

and $z_0$) are defined as the distance in the transverse plane or longitudinal axis between the track and the interaction point [81].

Vertices are reconstructed from tracks that fulfil a set of requirements which determine whether the tracks originated from the interaction point [82]. Since the detector sub-systems are sensitive to multiple $pp$ collisions that may occur within a single bunch crossing, multiple vertices are reconstructed. In this case, the vertex with the greatest sum of its associated track transverse momentum is defined as the primary vertex. The primary vertex is used to compute any reconstructed quantity related to the primary reconstruction vertex. For this analysis, only events are considered where the primary vertex has at least three associated tracks.

### 3.4.2 Jets

Due to QCD confinement, quarks and gluons hadronise before they can interact with the detector, which appear as clusters of collimated particles known as jets. The topological clusters (topoclusters) of energy deposits inside the hadronic calorimeter can be combined in order to reconstruct jets. An energy cell, with a signal that is at least four times greater than the expected electronic noise, is used as a starting seed to build these topoclusters. Furthermore. all neighbouring cells surrounding the seed are also collected and added to the cluster. Finally, any adjacent cells with signals greater than twice the expected noise value are then collected, as well as their neighbouring cells. This process is performed iteratively until all signals have been collected and added to the cluster. The position of the topocluster can then be defined by making use of an energy-weighted average of cell positions [83].

A specific algorithm, known as the anti-$k_t$ algorithm [84], is used to define a general method of combining clusters to form a single candidate jet. This algorithm compares distances between an object pair, $d_{ij}$, and the distance between an object and the beam, $d_{iB}$. These two distances are defined in the following manner:

$$d_{ij} = min(p_{T,i}^{-2}, p_{T,j}^{-2}) \frac{\Delta R_{ij}^2}{R^2} \tag{3.7}$$

$$d_{iB} = p_{T,i}^{-2} \tag{3.8}$$

where $p_{T,i}$ is the transverse momentum of object $i$, $\Delta R_{ij}$ is the spatial distance between the two objects in the $\eta - \phi$ plane and $R$ is a distance parameter that is used to restrict the size of jets. The distance parameter is usually fixed at a value ranging from 0.4 to 1.2. For each object, the distances $d_{ij}$ and $d_{iB}$ are calculated. If the minimum distance is $d_{iB}$, then the object is considered a complete jet and removed from the list of input particles. Otherwise, the two objects, $i$ and $j$, are combined by adding their four-momenta. This process continues iteratively until all clusters have been combined.

To give an approximation of the reconstructed objects in the idealised case where the calorimeter is perfectly efficient, this algorithm can also be used to create truth jets. The inputs for truth jets are stable particles from the MC truth record, rather than energy deposits from the calorimeter. All particles with lifetimes longer than $10\,\mathrm{ps}$, with the exception of muons and neutrinos, are included in the clustering of truth jets.

Once the algorithm has combined all clusters, the resulting reconstructed jet must be calibrated to take into account the different detector responses between electromagnetic and hadronic showers that are not corrected by the detectors. Consequently, jets are recalibrated to the full hadronic scale, known as the jet energy scale (JES), which is based on MC simulations of QCD di-jet events [85] [86].

Jets originating from the hadronisation of $b$ quarks have unique features, due to the relatively long lifetimes of hadrons containing a $b$ quark. ATLAS has developed several algorithms for the $b$-tagging of jets, which make use of different methods to singularly search for evidence of a B hadron decay. The IP3D algorithm relies on information concerning the impact parameters of the tracks associated with jet objects, while SV1 and JetFitter reconstruct secondary vertices inside the jet [87]. In addition, the MV1 algorithm uses multivariate techniques to combine the variables from the above-mentioned algorithms to greatly enhance $b$-tagging performance [88].

### 3.4.3 Electrons

Electron candidates are reconstructed by combining a track in the inner detector that points to an energy deposit in the electromagnetic calorimeter [89]. A "sliding-window" algorithm [90] is employed to search for energy clusters in the electromagnetic calorimeter, which could be used as seeds for object reconstruction. The size of the window is $\Delta\phi \times \Delta\eta = 0.025 \times 0.025$ and

the energy clusters must have a transverse energy of at least $2.5\,\mathrm{GeV}$. Standard ATLAS track reconstruction algorithms are employed to reconstruct tracks in the inner detector modules [91]. Additionally, the track reconstruction algorithm is complemented by a dedicated pattern recognition algorithm to take into account the potential energy loss due to brehmsstrahlung. Electron candidates are identified by matching the reconstructed tracks to the seed clusters in the electromagnetic calorimeter. In the case where multiple tracks are matched to a cluster, the track is chosen with at least one hit in the Pixel detector. If multiple tracks also have hits in the pixel detector, then the track with the smallest $\Delta R$ is selected.

Once the candidate clusters have been identified, blocks of cells of varying sizes are used to rebuild the clusters. The varying sizes of the cells depend on the location of the pre-cluster in the calorimeter, coupled with the type of particle candidate in the process of being reconstructed. For electrons and converted photons, a block of cells of size $3 \times 7$ is used in the barrel, while a block of cells of size $5 \times 5$ is used in the end cap. Showers from electrons are wider in the barrel region than for photons, since electrons are more likely to interact with upstream material and can also emit photons from brehmsstrahlung. Due to the magnetic field, the electron's trajectory is also curved in the $\phi$ direction. For this reason, the $\phi$ size of the cluster is increased to contain most of the energy deposited in the calorimeter. Similarly, the $\phi$ size of the cluster is also increased for converted photons, since they can produce electron-positron pairs that spread out in the $\phi$ direction also due to the magnetic field.

In contrast, the effect of the magnetic field is smaller in the end cap region, leading to a smaller block of cells of identical size for all particles types. The $\eta$ size of the cluster is much larger than in the barrel, due to the smaller physical cell size. The total energy of the cluster is obtained by calculating the sum of the measured energy in the cluster and estimating the amount of energy lost before reaching the calorimeter. An in-situ calibration is performed by making use of $Z \rightarrow ee$ and $J/\psi \rightarrow ee$ data events [92], before the final electron energy have finally been calculated. The four-momenta of the cluster may then be calculated by using the energy that has been constructed from the cluster and the $\eta$ and $\phi$ obtained from the associated track.

For the identification of electron candidates, ATLAS uses multivariate selection strategies together with a cut-based strategy. Three categories of electrons has been defined for both of these approaches: loose, medium and tight. Each of these categories have a different signal efficiency and background suppression associated with them. The classification of these categories is defined based on information about the transverse and longitudinal shape of the electromagnetic shower, energy leakage into the hadronic calorimeter, the quality of the inner detector track measurement, the track-to-cluster matching accuracy and the number of high threshold hits in the TRT. More information regarding these identification definitions is given in [89] [93].

### 3.4.4 Muons

Muons traversing through the ATLAS detector will create hits in the tracking detectors, but will deposit only small amounts of energy in the calorimeters due to their minimum ionising behaviour. Therefore, the reconstruction of muons relies mainly on the MS and the ID [94] [95]. Depending on the type of information available from various detector components four types of muons can be reconstructed: stand-alone, combined, segment-tagged and calorimeter tagged.

Stand-alone muon candidates are usually reconstructed at a range of $2.5 < |\eta| < 2.7$. Since this range is beyond the coverage of the ID, these muons can only be reconstructed based on the information from the MS. Two layers of MS chambers are usually necessary in order to construct a track. Furthermore, the track is then extrapolated back to the closest point to the beam line to determine the direction of flight and impact parameters, while simultaneously taking the estimated energy loss in the calorimeter system into account. Even though the acceptance level has been extended beyond the coverage of the ID, reduced momentum and impact parameter resolution are associated with this method. Combined muon candidates are reconstructed independently in both the ID as well as the MS, which are subsequently combined. The combination of muon tracks in both detectors provides the best momentum resolution as well as excellent background rejection. Most ATLAS analyses make use of this type of reconstructed muons. Segment-tagged muon candidates are usually reconstructed in the ID and extrapolated to the MS, where it is matched with a single track segment. These muons traverse only one layer of a MS chamber, due to either small transverse momentum or a poorly equipped area in the MS. Calorimeter tagged muon candidates are formed when an ID track is not associated with any track segments in the MS, but points to an energy deposit in the calorimeter. The energy deposit must also be consistent with a minimum-ionising particle. This type of reconstructed muon suffers from high background contamination.

For the reconstruction of stand-alone, combined and segment-tagged muons two complementary algorithms exist –both producing very similar results [96]. One approach, known as STACO, performs a statistical combination of the individual fits from track parameters by using their covariance matrices. The other approach, MUID, carries out a global refit of the track by using hit information from both the tracking detectors. A third algorithm that would aim to combine the best features of the previously mentioned approaches is currently being developed for future use.

For the identification of muons, ATLAS defines a set of criteria to define the purity of a muon candidates. The criteria is based on the type of reconstructed muon, its position in $\eta$ among other requirements. Three muon quality working points may be used: tight, medium and loose. Similar to the electron case, each of these working points have a different signal efficiency, background suppression and rejection of fake muons associated with them.

### 3.4.5 Missing transverse energy

Non-interacting particles, where neutrinos are the most prominent example, traverse through the ATLAS detector without leaving any tracks or energy deposits in any of the various detector components. Hence, the presence of these particles can only be inferred from the imbalance of transverse momenta in events. The vector sum of the transverse momentum should be exactly zero in the case where all particles have been detected in an event, due to the conservation of momentum in the transverse plane. Correspondingly, the inverse of the vector sum of all transverse momentum is known as the missing transverse momentum. ATLAS makes use of the calorimeter systems to measure the missing transverse energy, which can be defined as:

$$\vec{E}_T^{miss} = -\sum_i \vec{E}_{T,i} \tag{3.9}$$

where the sum runs over all particles produced and detected in an event. An object based approach is used in order to reconstruct the missing transverse energy. This approach allows for the use of different energy calibration schemes for different types of particles, which leads to optimised resolution. The total missing transverse energy is given by:

$$\vec{E}_T^{miss} = \vec{E}_T^{miss,e} + \vec{E}_T^{miss,\gamma} + \vec{E}_T^{miss,\mu} + \vec{E}_T^{miss,\tau} + \vec{E}_T^{miss,jets} + \vec{E}_T^{miss,Soft\ term}. \tag{3.10}$$

In this equation, the first five terms represent the contributions from reconstructed electrons, photons, hadronically decaying $\tau$-leptons, muons and jets. Moreover, jets with $p_T > 20\,\mathrm{GeV}$, calorimeter topoclusters and tracks that are not associated with any high-$p_T$ objects are also included in the calculation, which form the soft term in the equation. The muon contribution for the $E_T^{miss}$ calculation must be corrected to account for energy deposits that are created by muons in the calorimeter system. This can be done by correcting the term for the estimated energy loss of the muon in the calorimeter, which would already be included in the soft term contribution. The balance in the transverse momentum is ruined by pileup events, which cause the $E_T^{miss}$ resolution to be reduced. Pileup events refer to the case where either multiple events occur in the same bunch crossing or where the sub-detectors are sensitive to tracks in the time window between the main interactions. The reconstruction of the missing transverse energy, as well as the calibration of each of the terms is explained in [97] [98].

Calorimeter response is sensitive to several effects such as dead or noisy read-out channels, poorly estimated inactive material, escaping particles or mis-measurement of their energy. These effects can produce events with fake large $E_T^{miss}$ or degrade its resolution. As a result, the reconstructed missing transverse energy incorrectly reflects the actual missing transverse energy originating from a proton-proton collision. By making use of a track based measurement of $p_T^{miss}$ as a complementary measurement to the calorimeter $E_T^{miss}$, these background processes can be reduced significantly. However, this method can only be used for charged particles, since neutral particles do not leave any tracks in the Inner Detector. The imbalance of transverse momentum, $p_T^{miss}$, of a collision event is calculated by making use of tracks originating from the primary vertex and reconstructed in the

Inner Detector. The reconstructed primary vertex must have at least three constituent tracks, while at least one track of the event must pass a set of "high quality track requirements". The $x$ and $y$ components of and event's $p_T^{miss}$ are calculated in the following manner:

$$p_{x,y}^{miss} = -\sum_{tracks} p_{x,y} \tag{3.11}$$

which assumes that all tracks satisfy the high quality track requirements. The reader is referred to [99], for a more detailed discussion on this topic.

### 3.4.6 Overlap removal

In addition to basic object selection, it is possible for two or more objects to overlap in $\eta - \phi$ space. In this case, only one of the objects is considered whereas the other object is rejected. Since the EM calorimeter is utilised to reconstruct both electron candidates and jet candidates, an electron is always also reconstructed as a jet. In the case where a jet lies within a cone of radius $R = 0.3$ to an electron, the jet is removed. In addition, any jet candidate that lies within the above-mentioned radius of a muon is also removed. Lastly, any electron that lies within a cone of radius $R = 0.1$ of a muon is removed. This is necessary to account for highly energetic muons radiating photons that may possibly pair produce into an electron-positron pair.

# Chapter 4

# Upgrade of the LHC and ATLAS detector

Over the coming decade the LHC instantaneous luminosity is expected to increase to $2 - 5 \times 10^{34}\,\mathrm{cm}^{-2}\mathrm{s}^{-1}$ with respect to the design luminosity [100], ultimately leading up to the High-Luminosity LHC (HL-LHC) physics program. Besides operating at an increased centre of mass energy of $\sqrt{s} = 14\,\mathrm{TeV}$, the HL-LHC will also produce a total integrated luminosity of $L = 3000\,\mathrm{fb}^{-1}$ corresponding to an average of $\mu = 200$ inelastic $pp$ collisions per bunch crossing [10]. The main motivation for the HL-LHC is to extend and improve the physics program of the current LHC. Depending on the results of the LHC, the physics agenda for the HL-LHC, outlined in [101], [102] and [10], could focus on rare Higgs boson decays, precision studies of many Higgs couplings and the study of VBS [103], among many other interesting possible studies. Due to statistical errors dominating the uncertainty of the Run I $W^{\pm}W^{\pm}jj$-EW measurement at $\sqrt{s} = 8\,\mathrm{TeV}$ [6] [7], the study of this process will be continued at future runs of the LHC at higher energies to refine this measurement.

To cope with the intense radiation and the increased pileup environment the ATLAS sub-detectors will require several significant upgrades or replacements. Particularly, upgrading the ATLAS sub-detectors, namely the inner tracking system, the calorimeters and the muon system, to include additional instrumentation and extend the pseudorapidity coverage in the forward regions out to $|\eta| \leq 4.0$ will lead to the improved reconstruction of physics objects. However, all extensions of the sub-detectors rely on the foundational charged particle reconstruction capabilities of the inner tracking system over an extended pseudorapidity range [104]. For this reason, the main focus will be the extension of the Inner Detector tracker to detect charged particles within $2.5 < |\eta| < 4.0$.

The following sections will outline the luminosity upgrades of the LHC, as well as the scheduled upgrades of the ATLAS sub-detectors toward the HL-LHC. The reader is referred to [11] for further discussions, since the following sections provide a summary of this work. Additionally, the extension of the ID tracking system will be discussed, since this specific feature will be of great importance in the study of VBS at the HL-LHC. Lastly, the final section of this chapter will describe the expected performance of the upgraded ATLAS detector during the HL-LHC run, which will be implemented to study the sensitivity of the SM $W^{\pm}W^{\pm}jj$-EW measurement at $\sqrt{s} = 14\,\mathrm{TeV}$ with a realistically projected upgraded ATLAS detector.

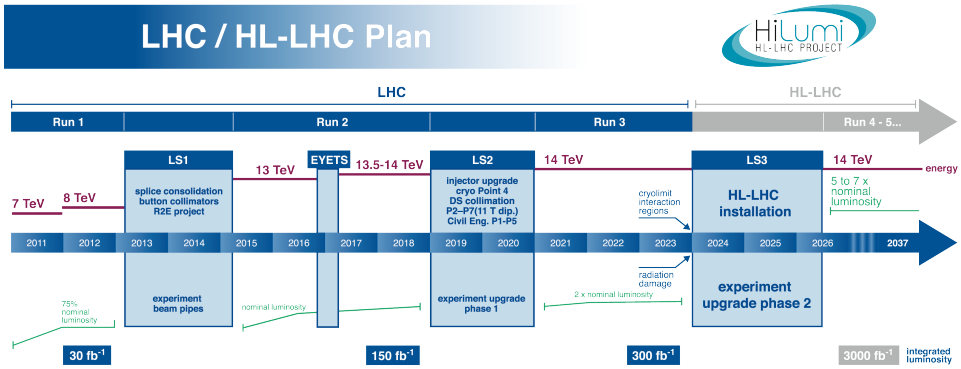


FIGURE 4.1: Upgrade schedule for the LHC towards the HL-LHC [105].

## 4.1 Scheduled LHC upgrades

A series of luminosity upgrades have been scheduled to prepare for the eventual upgrade of the LHC to the HL-LHC. The main goal is to increase the total integrated luminosity from approximately $300\,\mathrm{fb}^{-1}$, collected by the end of the LHC run in 2022, to $3000\,\mathrm{fb}^{-1}$ by the end of 2035. Accordingly, three long technical shutdowns have been foreseen for the LHC, during which various modifications and upgrades will be made toward the HL-LHC. These three technical shutdowns are known as 'phases', some of which have already been completed: Phase-0 (started in 2013 and continued during 2014), Phase-I (scheduled for 18 months from 2018 to 2019) and Phase-II (scheduled for 30 months between 2023 and 2023). Figure 4.1 shows a schematic of the scheduled technical shutdowns for the LHC.

Currently, Run II is underway which immediately followed the first long technical shutdown and will last for three years. The consolidation in the superconducting circuits of the LHC during the technical shutdown enabled the peak design luminosity and centre of mass energy to be reached during Run II. Next, the Phase-I upgrade will take place during the long shutdown between 2018 to 2019, which will aim to upgrade the injectors, the collimation system as well as the upgrade of the pre-accelerator chain. Specifically, the current Linac2 will be replaced with a more powerful proton linear accelerator, Linac4. In addition, the output energy of the Proton Synchrotron Booster will be increased. The goal of these upgrades will be to reach a centre of mass energy of $14\,\mathrm{TeV}$ and to increase the instantaneous luminosity by a factor of three. After the Phase I upgrade, experiments will be able to collect up to $300\,\mathrm{fb}^{-1}$ of proton-proton collision data. Finally, the Phase-II upgrade will be scheduled from 2023 to 2024, which will enable the installation of new focusing magnets and crab cavities. After these final scheduled upgrades, an instantaneous luminosity of $5 \times 10^{34}\,\mathrm{cm}^{-2}\mathrm{s}^{-1}$ should be accomplished.

## 4.2 ATLAS upgrades toward the HL-LHC

Due to the harsher radiation and high pileup environment associated with HL-LHC, several of the ATLAS sub-systems will require modifications. The ATLAS upgrade program has been scheduled in three phases, which corresponds to the three long technical shutdowns of the LHC. The main requirement of the sub-system upgrades is to maintain, or improve upon, the same level of detector performance achieved at the current LHC [11]. The harsher radiation conditions will affect sub-detectors that are located at a close proximity to the beamline or in the very forward regions, due to the high particle fluxes in these regions. Therefore, due to the expected increase of radiation damage, the Inner Detector, the forward calorimeter and the forward muon wheels will require several upgrades or even complete replacement. Possible foreseen modifications include radiation hard tracking detectors with higher granularity, improved bandwidth and more robust front-end (FE) electronics. Moreover, the higher event rates and event sizes will pose a great challenge for the Trigger and data acquisition systems, which will require new trigger algorithms.

All planned upgrades to the various sub-systems of the ATLAS detector are discussed in detail the Scoping Document [10]. The following section will briefly discuss the upgrades of the Calorimeter and trigger systems, as well as the extension of the ID. The upgrade of the Muon Small Wheels is thoroughly investigated in this thesis and will be described in great detail in Chapter 5.

### 4.2.1 Calorimeter and trigger upgrades

The high radiation and pileup conditions will impact the Calorimetry systems significantly. In order to maintain adequate performance the cold electronics inside the Liquid Argon Hadronic calorimeter will be completely replaced. In addition, the on and off-detector electronics for both the Liquid Argon Hadronic and Tile calorimeters will be implemented with a new readout architecture. Furthermore, digital information for all calorimeter cells for every bunch crossing will be transmitted directly to the off-detector system, greatly reducing system occupancies of front-end electronics in the high radiation environment. Lastly, transmission data bandwidth will be increased for the entire calorimeter system, up to a value of $200\,\mathrm{Tbps}$.

The back-end system will be utilised to feed the Level-0 and Level-1 trigger systems with pre-processed digital information. This system will also include a pipeline memory with programmable depth, ensuring the the system will be capable of coping with the latencies and trigger rates outlined in the new trigger schema [102]. The planned upgrade of the ALAS trigger system will include the addition of a Track Trigger at Level-1 and Level-2, leading to the application of full granularity of the calorimeter at Level-1 as well as the improvement of the muon trigger coverage.

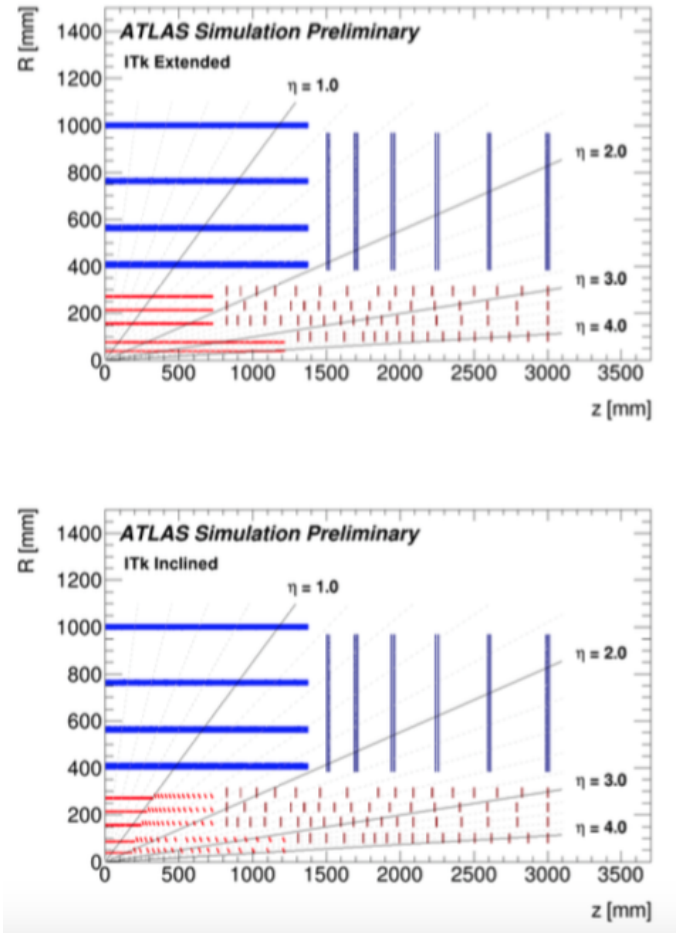


FIGURE 4.2: Schematic of the "extended" (top) and "inclined" (bottom) layouts, under consideration for the ITk, showing the active areas of silicon detectors arranged in cylinders and disks [106].

### 4.2.2 Extension of the Inner Detector

The number of pileup events associated with the HL-LHC will result in detector occupancies beyond the design parameters of the TRT. In addition, by 2022 the Pixel and SCT subsystems will seriously degrade in performance due to radiation damage to the sensors and front-end electronics [106]. Therefore, the ATLAS Collaboration made the decision to replace the entire Inner Detector with new, all-silicon Inner Trackers (ITk) consisting of Pixel and Strip detectors. Basic components as well as the baseline design of the ITk detector are described in the Letter of Intent [102]. The ITk must satisfy the following design criteria: higher granularity and an increased radiation hardness of readout electronics. The upgraded Inner Detector is being designed to provide not only 13 clusters per charged particle in the central barrel region, but also uniform coverage in the forward regions [106]. These designs would enable the ITk to precisely measure the transverse momenta and directions of isolated, charged particles -in particular muons and electrons.

Currently, two candidate layouts for the ITk is under consideration: the

"extended" and the "inclined" layout, depending on the design of the Pixel tracker [106]. Schematics of the two candidate layouts are shown in Figure 4.2. The main difference between these two layouts is the structural design of the Pixel barrel. To determine the optimal tracer architecture, the current stage of the ITk design phase is to study the performance of the two candidate layouts. For both designs, the Pixel system has been updated to cover a wider range in pseudorapidity up to $|\eta| \leq 4.0$. The strongest motivation for a tracker with an extended pseudorapidity coverage of $|\eta| \leq 4.0$ is the ability to reject forward pileup jets by associating the signal jets to the hard scattering vertex by making use of tracks. This can be achieved since the tracks due to pileup jets generally originate from pileup vertices, as opposed to the hard scatter primary vertex. Since VBS processes are characterised by the presence of high-$p_T$ forward jets, excellent discrimination between pileup jets and forward jets resulting from hard scattering events would be particularly beneficial for the study of VBS scattering processes at the HL-LHC. To investigate the prospects of a $W^{\pm}W^{\pm}jj$-EW measurement at the HL-LHC the expected performance of the upgraded ATLAS detector must be implemented in order to obtain a realistic verdict on the matter. The performance assumptions will be described in the following section.

### 4.2.3 Simulating the upgraded ATLAS detector

The expected performance of the upgraded detector has been studied in detail by making use of a full ATLAS detector simulation based on GEANT4 [107], as well as the properties of the detector sub-systems [108] [109]. Consequently, parametrised estimates of the of the performance and efficiencies of the ATLAS sub-detectors at the HL-LHC have been established and are provided for ATLAS analyses investigating physics processes at the HL-LHC. These upgrade performance functions are applied to truth-level quantities in order to modify the kinematics and take into account detector-level effects. First versions of the performance functions (TruthToRecoFunctions) were used in studies during the European Strategy for Particle Physics 2012 [110], as well as the European Committee for Future Accelerators 2013 [101] [111]. A new set of performance functions, smearing functions and efficiency functions were used in 2015 for physics studies outlined in the Scoping Document [10]. The current upgrade performance functions include detector momentum and energy resolutions (for smearing functions), object reconstruction efficiencies and trigger efficiencies for various different physics objects. In addition, a dedicated pileup overlay library is provided to add pileup jets to a hard scatter truth-event.

# Chapter 5

# Upgrade of the Muon Spectrometer

With the LHC scheduled to operate at a higher luminosity during Run III, the ATLAS Muon System's main upgrade project will involve the upgrade of the forward muon triggers. In order for ATLAS to maintain the Run I and Run II triggering capability of moderate momentum leptons under these higher background conditions, the first end cap stations of the MS, known as the Muon Small Wheels (SW), have been scheduled to be replaced [100]. The new replacement detectors will provide improved precision tracking at a high particle rate [11] and cover a large pseudorapidity range of $1.3 < |\eta| < 2.7$ [65]. In addition, the new Muon Small Wheels will be integrated into the Level-1 trigger [112].

In the following sections the ATLAS New Small Wheel Project will be described as well as the detector layout and technology, with a focus on the small-strip Thin Gas Chamber (sTGC) technology. The reader is referred to [65] and [100] for in-depth discussions on these topics, which were consulted for the summaries in the following sections. Since the assembly procedure to build a fully integrated wedge has not yet been finalised, a possible proposal of the sTGC assembly procedure that has been developed through discussions with many experts will be outlined. Particularly, a few of the more complicated steps in the process, requiring great care, will be highlighted. During sTGC wedge construction numerous resources will be necessary including teams of specialists trained to perform various tasks, specialised equipment and storage space for wedges in different stages of development. Besides optimising resources to quickly and effectively build sTGC wedges, various installation and testing methods must be finalised. Lastly, the final section of this chapter briefly discusses the estimated storage space requirements that will be necessary for crates of quadruplets, as well as completed sTQC wedges.

The New Small Wheel (NSW) will play a vital role in collecting signal for the $W^{\pm}W^{\pm}jj$-EW measurement during future runs of the LHC through to the HL-LHC physics Program. Specifically, the NSW coupled with a forward muon-tagger [10] will aid in significantly reducing additional leptons originating from other SM background processes. Same sign W boson scattering will be discussed in more detail in Chapter 6. Furthermore, the prospects of a $W^{\pm}W^{\pm}jj$-EW measurement during the HL-LHC run with the current proposed pseudorapidity range, as well as a scenario with an extended pseudorapidity up to $|\eta| \leq 4.0$ will be investigated in Chapter 7.

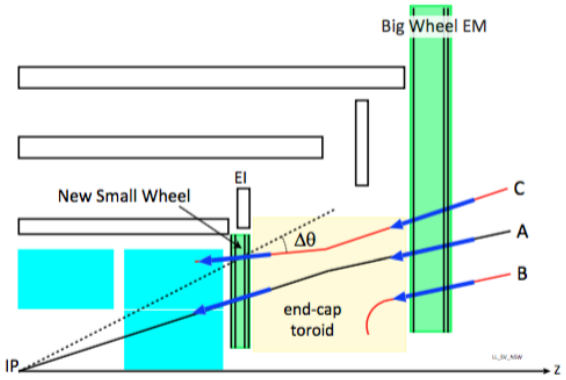


FIGURE 5.1: Illustration of the ATLAS muon trigger. The Big Wheel accepts all three of the shown tracks shown, however the two fake tracks (B and C) can be rejected at the NSW stage [65].

## 5.1 The New Small Wheel Project

For the ATLAS Muon trigger, the triggering rate is proportional to the instantaneous luminosity. Therefore, due to the higher background conditions associated with the expected increase of instantaneous luminosity during Run III, the Level-1 muon trigger will be eight to nine times higher in the barrel region. Currently, high fake rates dominate the forward muon triggers due to the low energy particles, mostly protons, created in the materials between the Big and Small Wheels. These low energy particles may consequently produce fake triggers by hitting the end cap chambers at similar angles as real high transverse muons. Therefore, with the increased levels of cavern background noise the performance of the muon tracking and spatial resolution will degrade significantly.

To address these issues, the NSW will comprise a set of precision tracking detectors that will be capable of identifying the origins of the triggered muons. Additionally, it will be capable of performing bunch crossing identification at a rate of up to $15\,\mathrm{kHz/cm^2}$ and a spatial resolution of fewer than $100\,\mu\mathrm{m}$ per detector plane. These requirements will be sufficient to provide an adequate angular resolution in order to distinguish whether triggered muons originated from the interaction point or elsewhere in the MS. Figure 5.1 illustrates the improved triggering capabilities of the Muon system with the addition of the NSW. Generally, the ATLAS Big Wheel accepts all three tracks in the illustration, however with the new enhancement of the NSW only tracks that have been confirmed by both the Big Wheel and the Small Wheel will be accepted. In Figure 5.1 only track 'A' will be accepted, while the fake tracks can be rejected. Track 'B' will be rejected because there is no matching track coming from the interaction point that also matches the Big Wheel candidate. Similarly track 'C' will be rejected since it does not point directly to the interaction point [65].

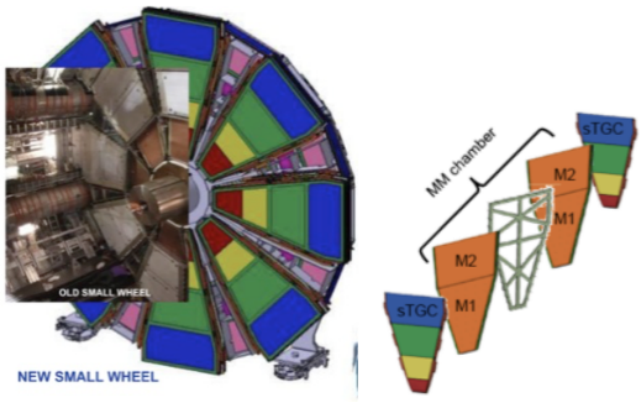


FIGURE 5.2: Left: The sixteen sectors of the NSW partially overlaid with the SW. Right: Sandwich arrangement of sTGC and MM detectors with the support structure [100].

### 5.1.1 Detector layout

The design of the NSW will follow the structure of the current Small Wheel (Figure 5.2) and will implement two complementary technologies; sTGCs and Micromegas (MM). There will be two NSWs, located on the A-side and C-side of the NSW geometry which corresponds to the $+x$ and $-x$ sides in the ATLAS coordinate system. The NSW will consist of sixteen detector planes arranged in two multilayers. These multilayers are divided into eight large sectors, while the gaps between these sectors will be filled with eight small sectors that will allow for some overlap between the different sectors. Each sector comprises four sTGC and four MM detector planes. In addition, these detector planes implement a sandwich arrangement of two sTGCs and two MM chambers and will be mounted directly on the spacer frame to support the whole sector. Figure 5.2 shows an illustration of the sandwich arrangement. Particularly, this arrangement of detectors will maximise the distance between the main triggering planes, which will consequently lead to the improved angular resolution of the online track segment. The eight-fold symmetry design of the NSW will ensure a robust, fully functional detector over the entire course of its lifetime. A specific amount of eight detector planes will be sufficient to ensure track reconstruction with high precision and efficiency under a high background environment. Additionally, the large amount of detector planes ensure appropriate detector performance even in the case where some planes fail to function as expected.

The two detector technologies implemented by the NSW will each perform a different task as their primary function. Specifically, sTGC technology will function as the primary trigger due to their single bunch crossing capabilities, whereas MM chambers have excellent spatial resolution and will serve as the primary precision trackers for the NSW. However, these detectors will also complement one another by contributing to the primary function of the converse detector. For instance, in the forward regions of the MS the MM chambers will also serve as triggers in order to provide redundancy and improved coverage in the forward regions. Likewise, the

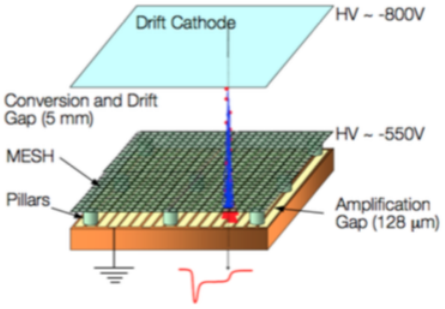


FIGURE 5.3: Basic structure of MM technology [100].

sTGC chambers will aid in the precision track measurements of the offline track segments. The following sections will briefly discuss the main concepts of the MM and sTGC technologies, also described in [100] [113].

### 5.1.2 Micromegas technology

Micromegas technology (an abbreviation for "micro mesh gaseous structure") enabled the construction of thin, wireless gaseous particle detectors [114]. The basic structure of a MM detector can be seen in Figure 5.3. MM detectors comprise a planar drift cathode, a gas gap of typically a few millimetres in thickness serving as a drift region and a thin, metallic wire mesh that is usually located at $100 - 150\,\mu\mathrm{m}$ from the readout electronics. This final area is known as an amplification region. The electric field inside the drift region is held constant at a few hundred $\mathrm{V/cm}$, while the electric field inside the amplification region is held at much higher values, typically between $40 - 50\,\mathrm{kV/cm}$.

MM chambers utilise a similar method that is employed by other gaseous particle detectors to detect charged particles traversing through the chamber. Charged particles ionise the gas mixture as they traverse through the drift region of the chamber, consequently creating electrons due to do ionisation process. These electrons drift toward the wire mesh until the amplification region is reached, where the electrons are accelerated due to the greater electric field gradient within the amplification region. Accordingly, an electron avalanche is produced inside the amplification region directly above the readout strip. Generally, the drift velocity of electrons in the drift region of the detector is usually slow and may take several tens of nanoseconds to reach the amplification region, whereas the amplification process only takes a fraction of a nanosecond. As a result, the readout strip detects a fast pulse of electrons. Ions produced in the avalanche process traverse back toward the amplification wire mesh, in the opposite direction of electrons. Since these ions are produced in the final stages of the avalanche process, most of these ions are located close to the readout strips. Even though the drift velocity of ions comparatively slow, it nevertheless only takes $100\,\mathrm{ns}$ for these ions to reach the amplification wire mesh. In comparison to other gaseous multiwire proportional chambers, this evacuation of positive ions is still relatively fast which indicates that the MM technology is well-suited to function in high particle flux environments.

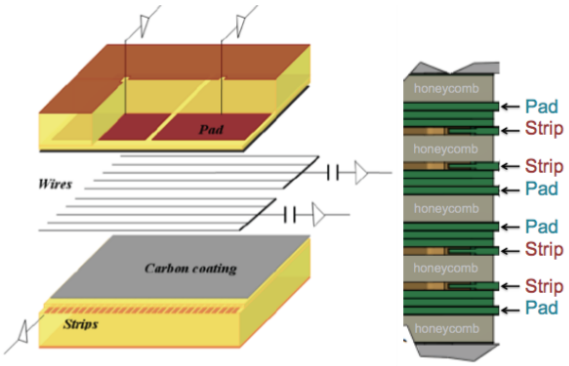


FIGURE 5.4: Left: Basic structure of a sTGC layer. Right: The sTGC quadruplet structure [113].

### 5.1.3 sTGC technology

TGC technology [115] was first used for the OPAL Pole-Tip calorimeter [116], as well as the ATLAS end cap muon trigger. Similar to their predecessors, sTGC detectors are also gaseous multiwire proportional chambers. Figure 5.4 shows the basic structure of a sTGC layer which consists of a grid of $50\,\mu\mathrm{m}$ gold plated tungsten wire held at a potential of $2.9\,\mathrm{kV}$, coupled with a pitch of $1.8\,\mathrm{mm}$ that are sandwiched between two cathode planes. Each cathode plane is at a distance of $1.4\,\mathrm{mm}$ away from the wire plane and are made of a graphite-epoxy mixture, with a typical surface resistivity of $100 - 200\,\mathrm{k}\Omega/\square$. Located behind the cathode planes, perpendicular to the wire plane are precision copper strips. Likewise, located behind the other side of the cathode planes are copper pads covering large rectangular surfaces on a $1.6\,\mathrm{mm}$ thick printed circuit board (PCB), with the ground shielding on the opposite side. Both pads and strips serve as readout electrodes.

The new precision strips have a pitch of $3.2\,\mathrm{mm}$ which is much smaller than the original TGC technology of $1\,\mathrm{cm}$ [117] (hence the new name "small-strip"). A smaller pitch for the new precision strips will ensure an improved angular resolution for online reconstructed segments. The cathode pads have a larger pitch of $80\,\mathrm{mm}$, which utilised to identify the muon tracks approximately pointing toward the interaction point by making use of a 3-out-of-4 coincidence. Additionally, these cathode pads are also used to identify the regions of interest that will be read out by the pads and strips for online event selection. Grouping the wires together aids in obtaining the azimuthal coordinate of the muon tracks. A sTGC chamber is filled with a gas mixture of 55% $CO_2$ and 45% n-pentane. Each sTGC wedge consists of three chambers or "quadruplets" –so called because each sTGC wedge, in turn, comprises four gas-gaps, which makes each chamber a stack of four detectors. The quadruplet structure of a sTGC chamber is illustrated in Figure 5.4.

The following sections will discuss the construction of sTGC chambers, followed by the detailed descriptions of various necessary steps to assemble quadruplets into a fully integrated sTGC wedge.

## 5.2 sTGC wedge construction

To construct a complete sTGC wedge, three types of sTGC quadruplets are required. In total, there are six types of sTGC quadruplets: three for the large sectors and three for the small sectors. These sectors are further divided into ”pivot" and ”confirm” layers, which refer to the roles the chambers play in the muon trigger. If there is a hit in a ”pivot” layer, the trigger searches for hits in the corresponding ”confirm” layer to make a decision regarding the muon track. Quadruplets are numbered from 1 to 3 indicating the smallest to the largest quadruplets, respectively. Additionally, the smallest quadruplets are located closest to the beam pipe, while conversely the largest quadruplets are located farthest from the beam pipe. The naming convention for quadruplets therefore indicates the size of the quadruplet, its location relative to the beam pipe, whether it will be used for a large or small sector and whether it forms part of a pivot or confirm wedge. All of the quadruplets are trapezoidal in shape and have dimensions between $1\,\mathrm{m}^2$ and $2\,\mathrm{m}^2$. Production sites located at institutions from across the world, namely Canada, Chile, China, Israel and Russia [100], will produce different types sTGC quadruplets as well as additional spare quadruplets. An illustration of the large and small sTGC sectors, together with the corresponding production sites of the quadruplets can be seen in Figure 5.5.

The main challenge to overcome with the construction of sTGC chambers and assembly of quadruplets is achieving a high precision alignment of readout strips across all detector layers. The necessary alignment between layers is $40\,\mu\mathrm{m}$ and can be obtained by machining the readout strips together with brass inserts, which allows the layers to be externally referenced with respect to precision pins that have been positioned on a flat table. Individual sTGC layers are glued together, while an externally machined frame maintain some separation between the layers. A $100\,\mu\mathrm{m}$ thinner honeycomb is placed over the surface of the detector as a spacer, which will allow the glue to serve as a filler in order to take into account any small unevenness of the PCBs. The glueing process assumes that various sTGC layers can be manipulated and placed in correct positions with respect to each other with high accuracy. For this purpose, external brass inserts attached to an external precision jig will be employed for the precise manipulation of sTGC layers. This precision jig will be placed on a large, perfectly horizontal marble table [65].

In the following sections several proposed procedures, which have been developed through discussions with many ATLAS-sTGC experts, for the assembly of a sTGC wedge will be outlined. The procedure for sTGC assembly has not been finalised yet, however the current version of the procedure is explained in the sTGC Assembly and Testing Manual [118]. This manual is an unofficial document which is constantly being updated with more refined methods and ideas. The successful assembly of a sTGC wedge will require various resources, including groups of specialists to perform various tasks, specialised equipment and in most cases a lot of space.

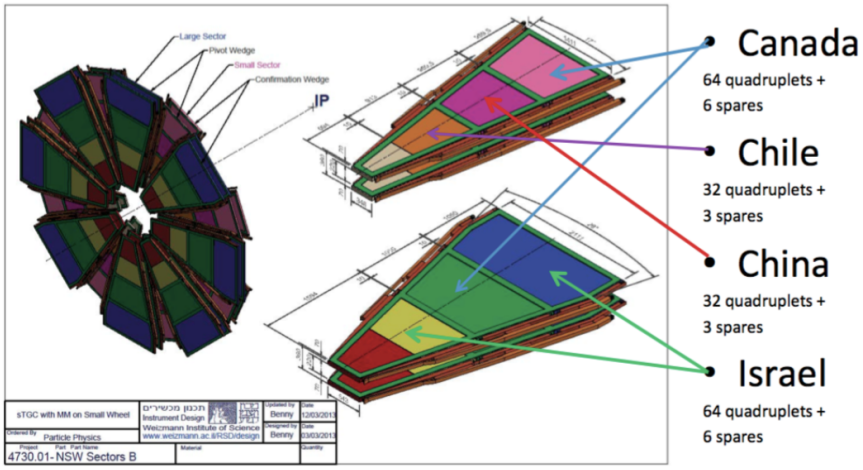


FIGURE 5.5: Left: Locations of pivot and confirm layers in the NSW. Right: Large and small sTGC wedges with the corresponding production sites [100].

### 5.2.1 Assembly procedure

#### Transport of quadruplets to CERN

Groups of four to five quadruplets, mounted in pallets, will be transported to CERN in air-conditioned containers equipped with temperature sensors to record the minimum and maximum temperatures inside the pallets. Each pallet will be equipped with shock absorbing devices, shock sensors and a barcode. A database will contain a list of the quadruplets associated with the pallet's barcode.

#### Checks upon arrival at CERN

Upon arrival at Building 180 at CERN, the containers will be unloaded and each pallet will be registered in the database. For this purpose, a hand-held device, which is capable of connecting to the network at a later time, will be necessary for database logging. Simultaneously, the shock sensors will be inspected and possible damage to the containers will be identified. Detectors will be examined for any gas leaks that may have developed during transit as well as any possible broken wires. Gas leaks will be tested by making use of a $CO_2$ line coming from a testing hut, while broken wires will be checked by applying $1.5\,\mathrm{kV}$ with a portable High Voltage (HV) source.

Once all these checks have been completed, the pallets will be transported to the Gamma Irradiation Facility (GIF++). The detectors should be flushed in the preparation area with $CO_2$ for 48 hours before they may be moved to the radiation area. If the readout electronics are available, then the detectors will be connected to the readout electronics as well as the HV, however the HV will not be switched on yet at this stage. The procedure that will be followed for the irradiation test is partly explained in [119]. Generally, the detectors will be flushed with a gas mixture of n-pentane and $CO_2$ for 48 hours. At the discretion of the facility, the source may or may not be turned on during this first flushing. When the source has been turned off, a HV of

$2.9\,\mathrm{kV}$ will be applied to all the detectors while the ground current of each detector will be measured and entered into the database. Finally, the source will the be turned on again to provide $20\,\mathrm{kHz}$ of detected photons in each plane. Since the chambers located in the back of the pallet will be shielded by the chambers in the front, irradiating each detector plane properly might be hard to achieve. None of the chambers should trip during the 1-2 hour irradiation period, otherwise any chamber that trip will be rejected. After the source has been switched off, the HV current of each detector will once again be measured and recorded in the database. The measured current should not exceed the initial ground current by $0.5\,\mu\mathrm{A}$. Once the process has been completed, the detectors should be retrieved and exchanged for a new pallet of detectors when GIF++ is next opened, usually once a week.

**Frame assembly**

Fibreglass frames will support each sTGC wedge, illustrated in Figure 5.6. Although these frames are not precision elements, the quadruplets must be precisely positioned when they are being glued to the frames. The position of the frames' "ears" will be the part that requires the most precision, since these ears will be used to attach the wedge kinematic mounts enabling the wedges to hang on the fully integrated NSW sector. These frames will be made from machine profiles and will arrive at CERN in pieces, which will be glued together. Frame pieces must be sorted in the case where they have not been pre-sorted, after which the frames will then be stored on shelves outside the clean room or, for the smaller pieces, on shelves inside the clean room. The required 128 large, 128 small frames and the spare frames should be built prior to the main wedge assembly schedule. It will not be necessary to perform the frame assembly process in the clean room, however the surfaces of the frames should still be cleaned before the glueing process may begin. The pieces should be assembled on top of a template to ensure that each piece has been positioned correctly. After the glue has been applied, the frames will be clamped or weighted and left to cure overnight. The frames may rest on any clean, flat area while the glue cures, however folding tables set up in the clean room might be preferable. Once the glue has dried, the frames may be stored on horizontal shelves.

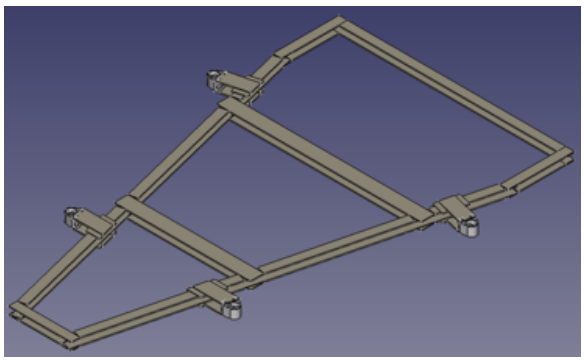

FIGURE 5.6: External frame that will support each wedge [118].

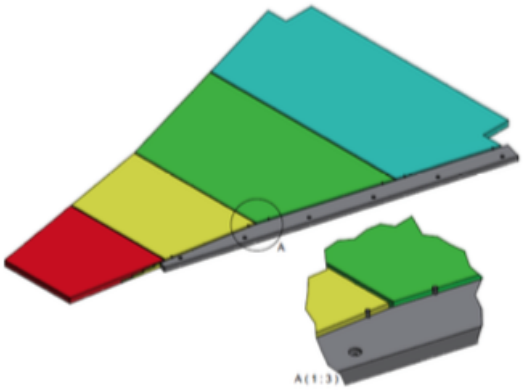

FIGURE 5.7: Schematic of the inserts used to align modules against precision pins [65].

**Integration of quadruplets into wedges**

This procedure requires a flat (within $50\,\mu\mathrm{m}$), granite table of $4.2 \times 2.4\,\mathrm{m}^2$, as well as six removable $10\,\mathrm{mm}$ diameter precision position pins used to match the inserts shown in Figure 5.7. The granite table will be equipped with a Mylar jig containing channels for compressed air, in order to release the quadruplets. Springs will pull the detectors against the precision pins to align detectors on the jig relative to the precision pins. It is assumed that it will be unnecessary to apply a vacuum underneath the detectors, since they are sufficiently flat and heavy to create their own vacuum and adhere to the table. Once the inserts have been checked to ensure that the alignment pins are in electrical contact with the inserts, the glue may be applied on the outside fibreglass frame and lowered onto the three quadruplets. Weights will then be placed on top of the frames and the system will be left overnight which would be a sufficient amount of time for the glue to cure.

After the glue has cured, the wedge must be lifted and turned by $180°$. This delicate operation will make use of a rotating frame, shown in Figure 5.8, with additional support bars in order to prevent deformation of the wedge. Tests performed with this lifting frame has demonstrated that this technique is capable of absorbing significant unevenness and non-parallelism between quadruplets. First, the alignment pins will be removed, while three vacuum chucks with flat, parallel faces and approximately $10\,\mathrm{cm}$ in thickness will be placed on the quadruplets. The surfaces of the chucks, equipped with silicon-rubber vacuum channels, will rest directly on the quadruplets and must be the correct size to cover most of the surfaces of the quadruplets inside the frames. Four tensioning rods will be used to attach the three chucks to the steel lifting frame. Additionally, wheels are located on one long side of the frame, corresponding to the frame's Bessel points, while the frame can be attached to the crane at the Bessel points located on the opposing side. Next, the crane will lift the frame slightly off the table and safety clamps will be attached to hold the quadruplets securely to the vacuum chucks. The crane will then continue to lift the assembly, very carefully, while simultaneously the wheels must be pushed forward toward the centre of the table. The wedge will then be allowed to stand vertically.

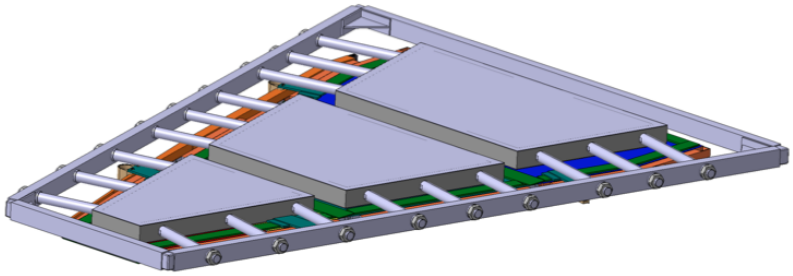

FIGURE 5.8: Schematic of the lifting tool [118].

At this point, modifications to the Mylar jig must be made for the channels to correspond to the smaller vacuum chucks, rather than the entire area of the quadruplets. Once the modifications to the Mylar jig has been completed, the crane will gently lower the wedge, while the wheels will continue to roll across the table. When the chucks are just slightly above the table, the safety clamps will then be removed and the positions of the chucks will be aligned to correspond to the Mylar jig. Finally, the crane will then lower the wedge onto the table to rest on the chucks that will be resting on top of the table. To avoid torque on the frame, both sides of the chucks must be perfectly flat and parallel. Precision pins will be screwed back into position and compressed air will float the wedge back into the correct position. Furthermore, the ears of the frame will be screwed and pegged to spherical mount holders, which will be slipped over the precision pegs. The ears will be glued to the frame in these positions, ensuring the precise positions of the ears with respect to the quadruplets.

After the wedge has been rotated, an alignment platform jig will be placed against the precision alignment features of each quadruplet, which will be used to install alignment and B-field sensor platforms. Photogrammetry targets, used to ascertain the relative positions of quadruplets within the wedge, will be installed by making use of the same alignment platform jig. The glue will be left to cure overnight and the following day the alignment team will return to perform photogrammetry measurements.

Once the alignment team completed the photogrammetry measurements, the previously mentioned procedure will be followed to glue the second fibreglass frame onto the quadruplets. Similarly, this frame's ears will also be attached to the spherical mount holders and glued to the frame, which will ensure that the frame cures in the correct position. Since the downward pressure of the weights might deform the unsupported areas of the quadruplets, it might be necessary to place a soft, springy support underneath the relevant areas. The assembly will once again be left overnight to cure.

After the glue has cured, the wedge must be lifted off the table while the

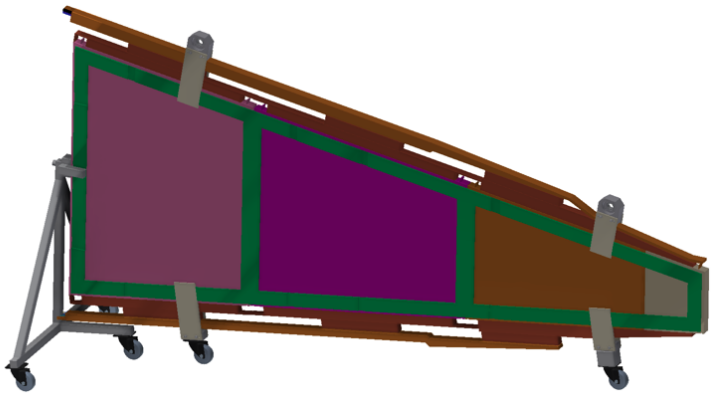

FIGURE 5.9: Tripod cart used to wheel the wedge to different locations [118].

vacuum chucks and lifting tool are released. The wedge may then be lowered to the ground in order to rest on its wheels. This step is an incredibly delicate operation and will require space, people and great care to successfully perform this complicated manoeuvre. First, the spherical mount holders will be removed and replaced with temporary mount holders, since these holders will be used to attach wheels and lifting shackles. Next, the lifting tool will be reattached to the vacuum chucks with the four tensioning rods, in order to follow the previous procedure and rotate the assembly into a vertical position. The crane will first lift the wedge off the table, then carefully lower the wedge until the wheels of the lifting frame touch the floor. However, blocks must be placed underneath the wedge's wheels to provide additional support, since these wheels will not be on the ground yet. The wedge's hoist shackles will then be attached to two hooks hanging from a support, taking care to ensure a minimal amount of slack in the lines. With the assembly hanging securely from the support the frame will be released from the wedge. Just in the same way, the safety clamps will first be removed followed by the release of the vacuum chucks, where particular care must be taken to hold the wedge steady. To allow the wedge's wheels to bear the full weight of the wedge, hooks will be attached to the lifting shackles and the wedge wheels. At this point, the crane will remove the lifting frame and vacuum chucks. Finally, crane hooks will be attached to the lifting shackles and the crane will first lift the wedge off the blocks in order to then lower the wedge to the ground, where it will stand on its own wheels. A tripod "cart", shown in Figure 5.9, will be necessary to support the wedge.

The wedge can then be prepared for connections to gas distribution and HV lines. For this purpose, u-shaped connections must be made at the intersections of the different quadruplets, specifically between the four layers of gas lines. A special rotating device, Figure 5.10, will be used for the installation of on-detector electronics as well as the in situ assembly of Faraday cages over the adaptor boards. In order to mount the wedge onto this rotating frame, support points must be attached to each end together with aluminium profiles on each side. The crane will lift the support point very

slightly to raise the wedge onto the "weight lifting" stands, which allow the wedge to rotate about its central axis.

The assembly of the Faraday cages could proof to be a complex operation, since the cage for the large wedge consists of 50 individual pieces to be assembled at different stages. Furthermore, a final protection shield for the Faraday cages will only be mounted after the completion of long-term tests, due to the inaccessibility of electronics once the cages have been completely closed. Lastly, the slots for the front-end boards (FEBs) should be closed with duct tape to prevent humidity during the long-term test period and to ensure realistic currents.

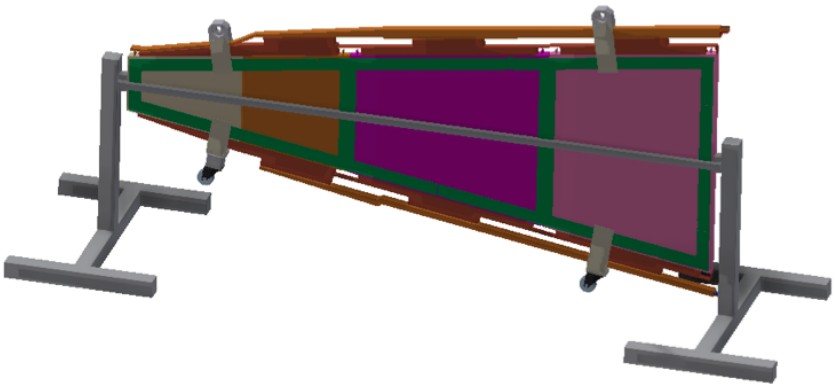

FIGURE 5.10: Device used for rotation of the wedge to install remaining services without deformations [118].

**Long-term HV testing**

To move the wedge to the test room for long-term testing, the wheels will be reattached and the wedge will be removed from the rotating frame with the crane. The tripod "cart" will be attached again to support the wedge while it is being wheeled into the test room. Once the wedge has been wheeled to the correct position inside the test room, the tripod may be removed and the wedge should either be secured to a fixed tripod, in the case where it is the first wedge, or to a neighbouring wedge. Gas and HV lines will then be connected and the wedge will be flushed first with $CO_2$ for 48 hours, before receiving normal operating gas. After 24 hours the HV may be turned on in order to begin recording the currents in the database. Wedges will be operated for approximately three months under high voltage with normal operating gas and the current will be logged periodically during this time. There should be no more than one HV trip, otherwise the relevant wedge should be investigated. After three months of testing, the operating gas will be switch off and the wedge will once again be flushed with $CO_2$ for 48 hours. The HV and gas lines will be disconnected and protective paper tape will cover the gas inlets and outlets to prevent dust from entering. The wedge will then be attached to its tripod cart and wheeled out of the test room to a safe storage area, until the installation of the final on-detector electronics.

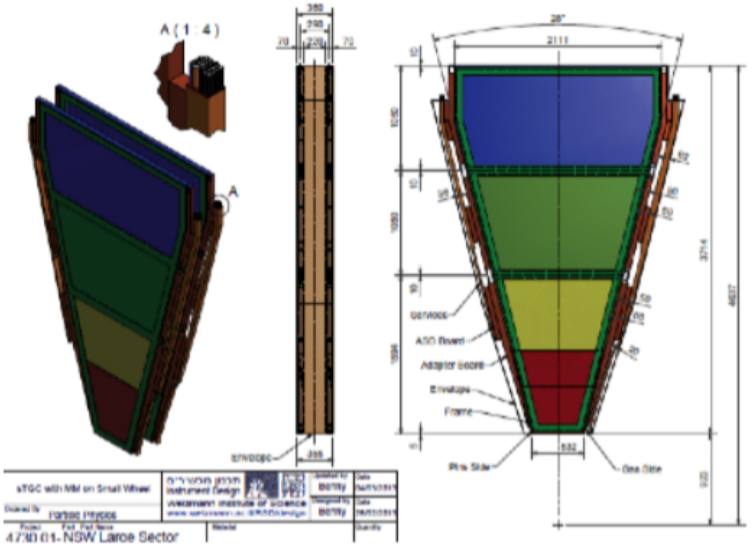


FIGURE 5.11: A fully integrated device with all its services installed [65].

**Completion of a sector wedge**

The on-detector electronics, when available, will be installed together with various other remaining services including cooling and alignment sensors. Consequently, the wedges will be placed in the rotating frames and, since this operation should not take place inside the clean room, a small crane or a lifting-jack will be necessary to raise the wedges onto the frames. Due to this delicate operation, manipulations of wedges should be minimised by optimising installation and testing procedures. Therefore, the remaining services will be installed in an enclosed area inside Building 180, where multiple installation stations will be set up. Ideally, these multiple installation stations will keep the wedge stationary while various specialised teams rotate through the sequence of installation activities. In addition, the installation of services for wedges from large sections will require scaffolding to reach the upper sides of the wedges.

Besides connecting the FEBs to the adaptor boards, thermal foam will also be stuck on all the FEBs that output significant heat. Furthermore, copper cooling pipes must be fitted and welded to the protection boxes that will eventually slide over the FEBs. This delicate operation will require a large amount of space, since the pipe will run the full length of the wedge and back, while bent into a complicated shape before it can be welded to the protection shield boxes completing the Faraday cages. A very talented pipe fitter and welder would have to perform this task. Once this procedure has been completed successfully, the protection boxes will be eased into position over the FEBs. At this point, the Faraday cages may be sealed properly, while readout and HV cables will be connected and routed through the services channels on both sides of the wedge. The final step is for the alignment team to mount alignment fibres, temperature sensors and B-field sensors on the surface of a fully integrated wedge. However, care must be taken to avoid violating the grounding strategy of the electronics. A fully

integrated wedge, seen in Figure 5.11, after the installation of the final services may then be stored in a large, sheltered area in Building 180 until required.

### 5.2.2 Storage requirements

Storage space will be necessary for crates of quadruplets as they arrive from production sites located all over the world. Due to different shipping durations, some types of quadruplets may arrive at CERN much sooner than other quadruplets. However, all three types of quadruplets are necessary to construct a sTGC wedge, which will result in considerable pile-up of quadruplet crates. Current shipping schedules and approximated arrival dates may be used to calculate an estimate of the amount of necessary storage space for quadruplet crates. Quadruplets produced in Canada, Chile and China will be transported to CERN by ship, whereas quadruplets produced in Israel and Russia would be shipped overland. It has been assumed that road shipments would be smaller, but more frequent. Current estimated shipping and arrival dates are subject to change and have not been finalised yet. The sizes of the crates for different quadruplets were approximated by using the measurements of the QS3 crate, designed in Canada, and scaling them with respect to the design specifications for each of the different types of quadruplets, described in [65]. The footprint of the QS3 crate is approximately $2\,\mathrm{m}^2$ and will to transport up to five quadruplets, as shown in Figure 5.12.

A diagram was then created that illustrates the various crates of different quadruplets that would be in storage for a given month. Correspondingly, this diagram does not include crates that have been moved to the clean room, hence it is evident that more space becomes gradually available as crates are moved out of storage and into the clean room. Additionally, completed wedges will also require storage space after they had been in the test room for approximately three months. The amount of space necessary for completed wedges was calculated by assuming that the wedges have been appropriately sheltered with large concrete blocks to prevent any damage. Figure 5.13 shows an example of the potential pile-up of quadruplet crates that may occur. Although shipments of QS3P and QS1P have already arrived at CERN from Chile, Canada and Israel, these crates must be placed in storage until the QS2P crates have arrived at CERN. In addition, upon arrival the QS2P crates must first be transported to GIF++, which would further delay the construction process. The entire storage evolution diagram may be viewed in Appendix A.

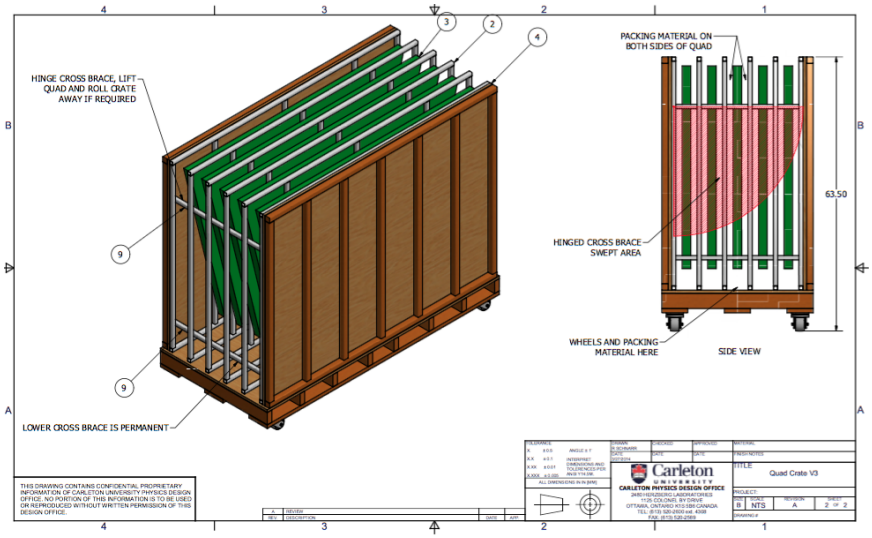


FIGURE 5.12: A QS3 crate, designed in Canada to transport up to five quadruplets [120].

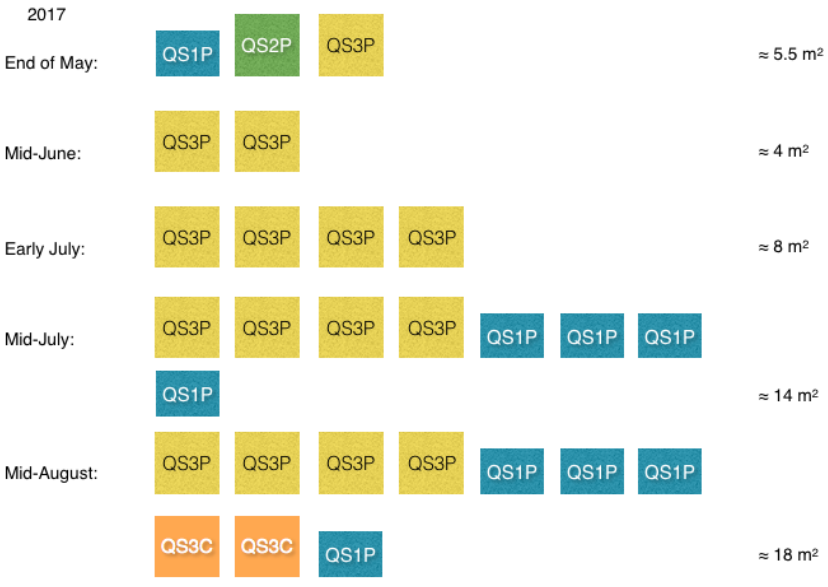


FIGURE 5.13: Potential pile-up of quadruplet crates. Shipments of the QS1P and QS3P quadruplet types have already arrived at CERN, however construction can only begin once the shipment of QS2P has arrived. The total approximated amount of necessary storage space is shown in the rightmost column.

# Chapter 6

# Same sign $W^{\pm}W^{\pm}$ production

An incredibly rare process, same sign W boson scattering occurs at hadron colliders like the LHC, as an interaction of W bosons radiated off incoming proton beams. These W bosons subsequently decay, however only events are where the W bosons decay to electrons and muons, i.e $W^{\pm} \rightarrow l^{\pm}\nu$, $l = e, \mu$, are selected. This process therefore has a very distinctive experimental signature of a lepton pair with the same electric charge and two high energy forward jets. Two analysis regions for the study of $W^{\pm}W^{\pm}jj$ production can be defined: an inclusive analysis region and a VBS analysis region [6]. The inclusive analysis region includes a combination of both strong and weak production mechanisms, used to measure the fiducial cross section of $W^{\pm}W^{\pm}$ production. In the VBS analysis region, events from strong $W^{\pm}W^{\pm}jj$ production are considered as background in order to study the purely electroweak $W^{\pm}W^{\pm}jj$ production process. The SM fiducial cross section predictions at leading order for the inclusive analysis region and VBS analysis region are $1.52 \pm 0.11$ fb and $0.95 \pm 0.06$ fb, respectively [6] [7].

Both ATLAS and CMS reported first evidence of the $W^{\pm}W^{\pm}jj$ scattering process, by making use of $pp$ collision data at $\sqrt{s} = 8\,\mathrm{TeV}$ collected by the ATLAS and CMS detectors in 2014. ATLAS measured cross sections for both the inclusive analysis and VBS analysis regions [6] [7]. The cross section for strong and electroweak $W^{\pm}W^{\pm}jj$ production in the inclusive analysis region was measured to be $\sigma^{fid} = 2.1 \pm 0.5\,\mathrm{fb}$, while the cross section for electroweak $W^{\pm}W^{\pm}jj$ production, which includes interference of strong production, was measured to be $\sigma = 1.3 \pm 0.4\,\mathrm{fb}$ for the VBS analysis region. Furthermore, the observed combined significance over the background-only hypothesis was 4.5 and 3.6 standard deviations in the inclusive region and the VBS region, respectively. CMS measured the cross section for electroweak $W^{\pm}W^{\pm}jj$ production to be $\sigma = 4.0^{+2.4}_{-2.0}\,\mathrm{fb}$ at an observed significance level of 2 standard deviations [8].

Recently, CMS observed electroweak production of same sign W boson scattering in $pp$ collisions at $13\,\mathrm{TeV}$. The observed significance is 5.5 standard deviations, where the SM predicts a significance of 5.7. In addition, the measured fiducial cross section was found to be $\sigma^{fid} = 3.83 \pm 0.66\,\mathrm{fb}$ [9]. Figures 6.1 and 6.2 present results from the $8\,\mathrm{TeV}$ ATLAS analysis and the recent CMS observation, respectively, showing an excess of data events over the predicted background processes. The $W^{\pm}W^{\pm}jj$-EW cross section is one of the smallest cross sections measured by the ATLAS detector and the first to reach the fb line [121].

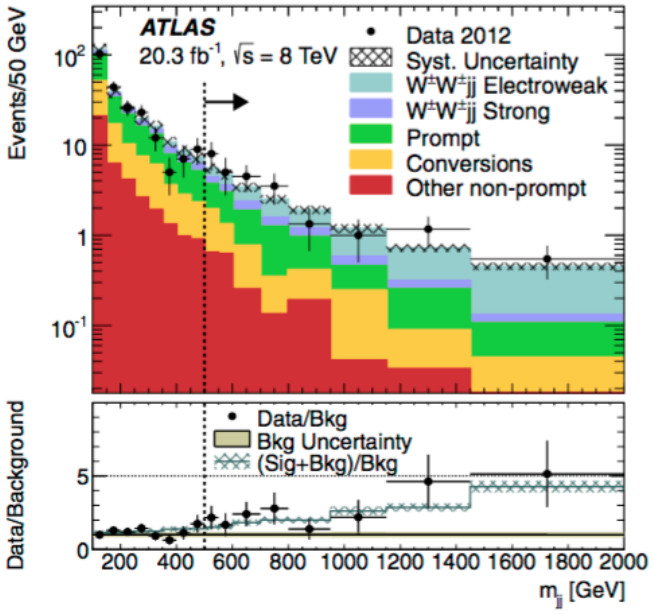


FIGURE 6.1: The di-jet invariant mass distribution for the predicted background and signal events obtained by ATLAS. The hashed bars represent the systematic uncertainties in the total prediction, while the lower plot shows the ratio of the total prediction to background only and the uncertainty [7].

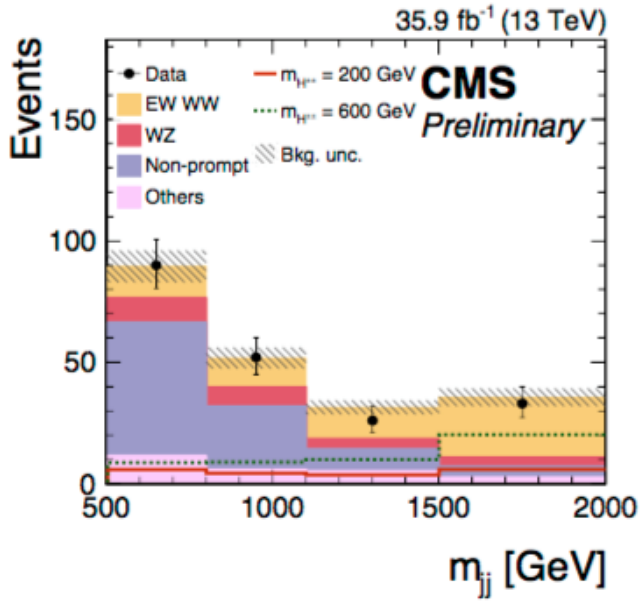


FIGURE 6.2: The di-jet invariant mass distribution for predicted background and signal events obtained by CMS. The hashed bars represent the systematic and statistical uncertainties [9].

Further studies of this rare process with data at a centre of mass energy of $\sqrt{s} = 13\,\mathrm{TeV}$ will increase our understanding of VBS scattering processes as well as electroweak processes. By making use of data from $pp$ collisions at a higher centre of mass energy than the previous study an excess of data events over the expected background processes at a significance level of 5 standard deviations could be observed, which would provide corroborative evidence for same sign W boson scattering. The ATLAS $W^{\pm}W^{\pm}jj$-EW analysis at $13\,\mathrm{TeV}$ is still underway at the time of the writing of this thesis.

This chapter introduces the experimental signature and topology of $W^{\pm}W^{\pm}$ scattering, as well as the various SM processes that could mimic the $W^{\pm}W^{\pm}$ signature. In addition, sections in this chapter discuss the object and event selections, signal and background estimations using MC simulations or data-driven methods and the systematic uncertainties associated with these methods. Furthermore, various di-lepton control regions used to test the modelling of background estimations will be summarised, with a focus on the $b$-tagged control region. Current studies of this control region are ongoing.

## 6.1 Experimental signature

The final state of the $W^{\pm}W^{\pm}$ scattering process under investigation consists of two leptons of the same electric charge, two neutrinos and two forward jets. For this reason, the $W^{\pm}W^{\pm}jj$ process has an unique experimental signature characterised by the presence of two, high energy forward jets in opposite hemispheres with large invariant mass, as well as the presence of a same electric charge lepton pair. When combined, these two signatures can reduce most SM background processes. Similarly, events arising from VBS processes exhibit a set of very distinct kinematic properties, which can be used to define selection criteria for the signal regions. Due to the emission of a vector boson from each incoming quark line, the resulting quarks tend to be at high absolute values of rapidity with large momenta. The two jets in these processes usually tend to be well-separated in rapidity with large invariant mass. Figure 6.3 illustrates the typical event topology for vector boson scattering processes.

## 6.2 Background processes

Despite the unique experimental signature of $W^{\pm}W^{\pm}jj$ production, some SM processes or detector effects can still mimic the signature of $ll' + E_T^{miss} +$ 2 jets and must be excluded or reduced as background processes. These background processes can be categorised into three main groups according to the origin of the leptons, which will be discussed in the following sections, also described in detail in [6] [7] [43] which were the main sources of reference.

### 6.2.1 Prompt processes

Processes in which the final states produce two jets, two leptons of the same electric charge and missing transverse energy are called prompt processes.

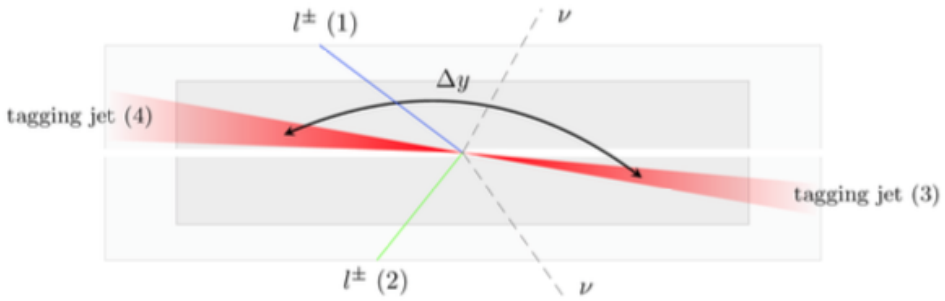


FIGURE 6.3: Event topology for $W^{\pm}W^{\pm}jj$: two forward tagging jets (labelled as 3 and 4) encompass the two leptons of same electric charge (1 and 2), which are the visible decay products of the scattered W bosons [121].

The dominant prompt lepton background is due to the $WZ/\gamma* \rightarrow l^{\pm}l^{\mp}l^{\pm}\nu$ process, which could pass signal selection criteria when one lepton is mis-reconstructed or not identified while the remaining leptons have the same charge. Approximately 90% of the total prompt background is due to the WZ process [7]. Another process included in the prompt background is $ZZ \rightarrow l^{+}l^{-}l'^{+}l'^{-}$. These cases may pass signal selection cuts, when one or more of the final leptons are mis-reconstructed leading to two leptons of the same electric charge. Double parton scattering processes also contribute toward the prompt background. For these processes, the experimental signature of the $WZ/\gamma$ produce may be produced from collisions between two incoming pairs of partons, such as $W^{\pm}$ + jets interacting with Z + jets, as an example. Prompt background processes are estimated by making use of MC samples.

### 6.2.2 Backgrounds from photon conversion

This category of background processes include not only backgrounds due to photon conversions, but also SM processes producing two opposite sign leptons that are mis-reconstructed as same sign events due to charge mis-identification (misID). The dominant mechanism contributing to the charge mis-ID background is known as the "trident" process, while the main process that contribute toward backgrounds due to photon conversions is production of the $W^{\pm}\gamma jj$ process.

A representative Feynman diagram of the trident process is shown in Figure 6.4. In this process, a prompt electron radiates an energetic photon due to hard brehmsstralung which subsequently converts into an electron-positron pair. On the other hand, charge mis-ID for combined muons have been found to be negligible and is therefore not considered in the analysis. Other processes that also contribute toward the charge mis-ID background are $W^{\pm}\gamma \rightarrow l^{\pm}\nu\gamma$, $Z \rightarrow e^{+}e^{-}$ and fully leptonic $t\bar{t} \rightarrow l\nu l\nu b\bar{b}$ decays.

The production of the $W^{\pm}\gamma jj$ process can mimic the same sign selection criteria when a photon is reconstructed as an electron. This can occur when the photon converts in the detector into an electron-positron pair and one of the

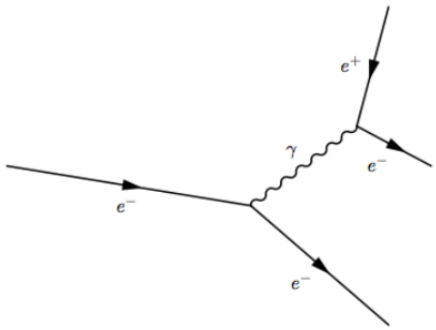


FIGURE 6.4: Representative Feynman diagram of the "trident" process: if most of the energy from the original $e^-$ is carried over to the $e^+$, then is is very likely that the $e^+$ will be reconstructed [81].

two leptons is not reconstructed. The $W^{\pm}\gamma$ process can be separated into strong and an electroweak processes. Both these processes are estimated from MC samples, while the charge mis-ID backgrounds are estimated by making use of a data-driven technique.

### 6.2.3 Non-prompt processes

Processes producing one prompt lepton from a W boson decay and one lepton originating from hadronic decays, or jets mis-reconstructed as leptons are known as the non-prompt background. The non-prompt category is dominated by backgrounds due to jet faked leptons, which can occur from the leptonic decays of hadrons within the jets. These leptons are considered a source of background, since they did not originate from the original hard scattering event. The main contributing sources to this background are W + jets$\rightarrow$ $l^{\pm}\nu+$ jets, $t\bar{t}$ $\rightarrow$ $l^{+}\nu bjj\bar{b}$, single top production and QCD multijet processes. Events due to these processes may be mistaken for the $W^{\pm}W^{\pm}jj$ signal if one of the associated jets are reconstructed as a lepton or if a lepton from a hadronic decay within a jet passes the signal selection criteria. Since jet faked leptons are usually not well-isolated and often emerge as $b$-quark decays, strict isolation requirements of leptons can suppress this background. MC simulations can not accurately model non-prompt processes, therefore this background is estimated by making use of a data-driven fake factor method [6].

## 6.3 Object and event selection

Various analysis selection criteria are applied to minimise the total contributions from background processes, as well as to increase the signal to background ratio. The next section will first describe the selection criteria for physics objects, followed by the definition of the two fiducial regions studied in this analysis at particle level, which have also been summarised in Table 6.5. Selection criteria for the signal region is similar to the criteria used by the $8\,\mathrm{TeV}$ analysis, described in [6] [7].

TABLE 6.1: Nominal muon definition.

| **Description** | **Selection value** |
|---|---|
| Quality | `medium` |
| Kinematic acceptance | $p_T > 25\,\mathrm{GeV}$ |
| Geometric acceptance | $\lvert\eta\rvert < 2.5$ |
| Longitudinal impact parameter | $\lvert z_0 \times \sin\theta\rvert < 0.5\,\mathrm{mm}$ |
| Transverse impact parameter | $\frac{d_0}{\sigma_{d_0}} < 3$ |
| Isolation | `gradient` |

### Triggers

Single electron and muon triggers with low transverse momentum acceptance thresholds are used in this analysis. For each event, at least one nominal electron or muon is required to be matched to a trigger object with a $p_T$ greater than the trigger object's threshold by at least $1\,\mathrm{GeV}$. The trigger efficiency in MC is corrected by scale factors provided by the combined performance groups of the ATLAS Collaboration.

### Lepton isolation

Leptons are required to be isolated in order to reduce the amount of leptons originating from hadronic decays or jet-faked leptons. Several isolation working points are used by ATLAS and either make use of simple fixed cuts or targeted efficiencies at specific transverse momenta. The isolation working point implemented by this analysis is the `gradient` definition, which employs a calorimeter and track isolation efficiency, $\epsilon$, calculated by

$$\epsilon = (0.057 \times p_T + 95.57)\%. \tag{6.1}$$

The isolation is applied as a function of $|\eta|$ and $p_T$ to obtain the targeted efficiency. Furthermore the combined isolation has a targeted efficiency of 95% at $25\,\mathrm{GeV}$ and 99% at $60\,\mathrm{GeV}$.

### Muons

Muons are required to fulfil the quality requirements recommended by the ATLAS Collaboration for medium muons. In addition, kinematic cuts are applied to reduce muons originating from pileup events as well as multijet backgrounds. Markedly, the inner detector track associated to the muon is required to originate from the primary vertex. This requirement can be achieved by requiring that each muon's flight path intersects the beam axis to within $0.5\,\mathrm{mm}$ of the primary vertex. In addition, the distance to the closest approach to the primary vertex in the transverse plane ($d_0$) divided by its resolution must be less than three. Furthermore, muons are required to have a transverse momentum $p_T > 25\,\mathrm{GeV}$ and fall within the geometrical acceptance of $|\eta| < 2.5$. To reduce contributions from muons originating from heavy flavour decays and other multijet process, muons are required to pass an isolation cut. All quality requirements for muons are listed in Table 6.1.

TABLE 6.2: Loose muon definition.

| **Description** | **Selection value** |
|---|---|
| Quality | `medium` |
| Kinematic acceptance | $p_T > 25\,\text{GeV}$ |
| Geometric acceptance | $\lvert\eta\rvert < 2.5$ |
| Longitudinal impact parameter | $\lvert z_0 \times \sin\theta\rvert < 0.5\,\text{mm}$ |
| Transverse impact parameter | $\frac{d_0}{\sigma_{d_0}} < 6$ |
| Isolation | `fail gradient` |

TABLE 6.3: Nominal electron definition.

| **Description** | **Selection value** |
|---|---|
| Kinematic acceptance | $p_T > 25\,\text{GeV}$ |
| Geometric acceptance | $\lvert\eta\rvert < 2.5$, outside crack region $1.37 \leq \lvert\eta\rvert \leq 1.52$ |
| Identification criteria | `Tight` |
| Longitudinal impact parameter | $\lvert z_0 \times \sin\theta\rvert < 0.5\,\text{mm}$ |
| Transverse impact parameter | $\frac{d_0}{\sigma_{d_0}} < 5$ |
| Isolation | `gradient` |

A looser transverse momentum requirement is required for muons is used for the third-lepton veto requirement. The nominal selection criteria remain the same, however veto muons must have $p_T > 10\,\text{GeV}$. Furthermore, the determination of the fake background implements a non-isolated definition for muons. The requirements for loose muons are shown in Table 6.2.

### Electrons

Besides the general reconstruction algorithm utilised for electrons, additional identification criteria are applied to further reject background, as shown in Table 6.3. Electrons are required to have a transverse energy $E_T > 25\,\text{GeV}$, a geometrical acceptance within $\lvert\eta\rvert < 2.47$ as well as $1.37 \leq \lvert\eta\rvert \leq 1.52$ outside the calorimetric crack region. Similar to the muon case, electrons are required to pass the selected isolation requirement.

Just in the same manner as the muons case, veto electrons have a looser transverse momentum requirement $p_T > 10\,\text{GeV}$ and must be identified as a `Medium` electron for the use of the third-lepton veto. Similarly, a non-isolated definition is also employed for the use of the fake background estimation. Selection requirements for loose electrons are listed in Table 6.4.

### Jets

Jets are reconstructed by making use of the anti-$k_T$ algorithm with a resolution parameter of $R = 0.4$ and calibrated with the Jet Energy Scale. Selected jets are required to have $p_T > 30\,\text{GeV}$ with $\lvert\eta\rvert < 4.5$. In addition, jets within $\lvert\eta\rvert < 2.4$ that have $p_T < 50\,\text{GeV}$ are required to have a Jet Vertex Tagger

TABLE 6.4: Loose electron definition.

| **Description** | **Selection value** |
|---|---|
| Kinematic acceptance | $p_T > 25\,\mathrm{GeV}$ |
| Geometric acceptance | $\lvert\eta\rvert < 2.5$, outside crack region $1.37 \leq \lvert\eta\rvert \leq 1.52$ |
| Identification criteria | `Loose` |
| Longitudinal impact parameter | $\lvert z_0 \times \sin\theta\rvert < 0.5\,\mathrm{mm}$ |
| Transverse impact parameter | $\frac{d_0}{\sigma_{d_0}} < 5.$ |
| Isolation | `fail gradient` |

of JVT > 0.64. The JVT is implemented to reject jets with large contributions originating from pileup, by giving a measure of the contribution of tracks from a specific vertex to a jet [122]. Furthermore, $b$-jets are tagged by using a tagger that identifies $b$-jets with an efficiency of 80%. Generally, these $b$-tagging algorithms have several operating points chosen to provide a specific $b$-tagging efficiency on an inclusive $t\bar{t}$ sample. Correction factors are applied to simulated events to account for the differences between data and simulation of the $b$-tagging efficiency for $b$, $c$ and light jets. These correction factors are determined from the final states of $t\bar{t}$ events containing two leptons [123]. All jets passing the above-mentioned criteria and fall within $|\eta| < 2.5$ are considered with the $b$-tagging algorithm, while mis-tag efficiency scale factors are also applied to these jets.

### 6.3.1 Definition of the signal region

Events were selected during stable beam conditions while the relevant detector systems were fully functional. Candidate $W^{\pm}W^{\pm}jj$ events require exactly two prompt leptons of the same electric charge. In addition, $\tau$ leptons or leptons originating from $\tau$ decays are not considered. Three different final states or "channels" are investigated depending on lepton flavour: $e^{\pm}e^{\pm}$, $\mu^{\pm}\mu^{\pm}$ and $e^{\pm}\mu^{\pm}$. Both leptons are required to have a transverse momentum of $p_T > 27\,\mathrm{GeV}$ to within $|\eta| < 2.5$ and an invariant mass $m_{ll} > 20\,\mathrm{GeV}$. Furthermore, the two leptons are required to have an angular separation of $\Delta R_{ll} \equiv \sqrt{(\Delta\phi)^2 + (\Delta\eta)^2} > 0.3$. Due to the non-negligible charge flip rate that occurs for electrons originating from the $Z/\gamma^*$ process, the di-electron invariant mass must not be within $15\,\mathrm{GeV}$ of the Z boson mass. This requirement reduces contributions from the Z + jets background, which arises from electron charge mis-identification. Events containing either additional leptons reconstructed with the loose isolation requirements, loose quality definition for electrons or containing $p_T > 7$ and $6\,\mathrm{GeV}$ for electrons and muons, respectively, are also excluded. This veto ensures the suppression of backgrounds from processes with more than two leptons in the final state, namely WZ/$\gamma^*$ + jets, ZZ + jets or events where a photon radiated by a muon is mis-reconstructed as an electron.

At least two jets satisfying the nominal objects selection criteria are required. Additionally, these two jets are required to have transverse momentum $p_T > 30\,\mathrm{GeV}$, $|\eta| < 4.5$ and separated from leptons by $\Delta R_{lj} > 0.3$. In order to reject non-prompt leptons, mainly originating from $t\bar{t} \to l\nu jjb\bar{b}$, events are vetoed if at least one jet has been identified as a $b$-jet. Tagging

TABLE 6.5: Selection criteria for signal regions.

| **Signal region** | | **Selection criteria** |
|---|---|---|
| Inclusive | Lepton | Two tight leptons of the same electric charge with $p_T > 25\,\text{GeV}$ |
| | Jet | At least two jets with $p_T > 30\,\text{GeV}$ and $\|\eta\| < 4.5$ |
| | $m_{ll}$ | $m_{ll} > 20\,\text{GeV}$ |
| | $E_T^{miss}$ | $E_T^{miss} > 40\,\text{GeV}$ |
| | Z veto | $\|m_{ll} - m_Z\| > 10\,\text{GeV}$ |
| | $b$-jet veto | Identified $b$-jets with $p_T > 30\,\text{GeV}$ and $\|\eta\| < 2.5$ are excluded |
| | $m_{jj}$ | $m_{jj} > 500\,\text{GeV}$ |
| VBS | $\Delta y_{jj}$ | $\|\Delta y_{ij}\| > 2.4$ |

jets are defined as the two selected jets with the highest transverse momentum. These jets are required to have an invariant mass ($m_{jj}$) greater than $500\,\text{GeV}$, which further reduces contributions from $t\bar{t}$ and WZ/$\gamma^*$ + jets processes.

The magnitude of the missing transverse energy, calculated from all the neutrinos in the final state, must be greater than $30\,\text{GeV}$. This $E_T^{miss}$ requirement also reduces backgrounds due to charge mis-identification. To reduce the dependence on QED radiation, contributions from photons within $\Delta R = 0.1$ of the lepton direction has been included in the lepton momenta [6].

The above mentioned event selections define the inclusive analysis region used to calculate the fiducial cross section of $W^{\pm}W^{\pm}jj$ production. To extract the $W^{\pm}W^{\pm}jj$-EW component of the cross section, the two tagging jets are required to be well separated in rapidity $\Delta y_{jj} = |y_{j1} - y_{j2}| > 2.4$. This $W^{\pm}W^{\pm}jj$-EW region is known as the VBS region.

## 6.4 Signal and background estimation

In order to make a meaningful measurement of the $W^{\pm}W^{\pm}jj$ process, estimates of the number of events produced by each of the various SM processes that pass the selection criteria and filter into the signal regions are essential. Depending on the specific type of process, these estimates are calculated by making use of either MC simulations or data-driven techniques. Events for MC samples are generated in a two-step process. First the hard scattering of constituents within the proton are generated, followed by the hadronisation of outgoing quarks and gluons. After the events have been generated, the interactions of the particles with the detector are simulated making use of a full detector simulation [124] framework based on GEANT4. Additional inelastic $pp$ events, modelled by Pythia 6.428, are included in the simulation. The generated events are re-weighted to reproduce the average number of collisions per bunch crossing observed in the data. An additional pileup contribution arises from the sensitivity of sub-detector systems to interactions in the preceding bunch crossings. This effect is also modelled in the simulation.

The generated events are then reconstructed from the simulated detector

signals using the standard ATLAS reconstruction algorithms, also implemented for data. After the reconstruction of events, several correction factors are applied in order to take into account the differences with respect to data. Correction factors including lepton and jet efficiencies, additional $pp$ interaction multiplicities and beam spot location, $b$-tagging efficiency and mis-tag rate for jets are applied to the simulation. In addition, the simulations are tuned to take into account for calorimeter response, as well as the muon momentum scale and resolution.

Signal and background estimations will be described in more detail in the following sections, and is discussed at length in [6]. The method implemented to estimate the predicted $W^{\pm}W^{\pm}$ cross sections for the $13\,\mathrm{TeV}$ analysis has not yet been finalised during the writing of this thesis, however it is likely that a similar method utilised by the $8\,\mathrm{Tev}$ analysis will be decided upon. For this reason, the method used by the $8\,\mathrm{TeV}$ analysis will be described below. Various sources of systematic uncertainties associated with the background estimations will be discussed in Section 6.5.

### 6.4.1 Signal estimation

The electroweak and strong production processes of $W^{\pm}W^{\pm}jj$ are simulated separately by making use of the Sherpa event generator, normalised to next to leading order cross sections that have been calculated in the two fiducial regions [6]. The cross sections for these two regions, the "fiducial cross section", are calculated using Powhegbox with CT10 parton distribution functions (PDFs) [125] interfaced with Pythia 8 for parton showering, hadronisation and underlying event modelling. The acceptance, which is defined as the fraction of generated events that pass the fiducial signal region selections, of Sherpa samples is used to convert the fiducial cross sections into cross sections corresponding to the phase space where the events were generated [81]. The samples can then be normalised to the correct luminosity.

The predicted fiducial cross sections for the electroweak $W^{\pm}W^{\pm}jj$ process are $1.00 \pm 0.06\,\mathrm{fb}$ and $0.88 \pm 0.05\,\mathrm{fb}$ in the inclusive and VBS regions, respectively. Predictions of the corresponding cross sections for the strong process are $0.35 \pm 0.05\,\mathrm{fb}$ and $0.098 \pm 0.018\,\mathrm{fb}$. Due to the absence of a NLO calculation for the combined $W^{\pm}W^{\pm}jj$ process, which includes both strong and weak production mechanisms, the effect of the interference between the two processes are calculated at leading order using Sherpa. The effect of the interference is studied by comparing the cross section of the combined process to the sum of the two cross sections for the electroweak and strong $W^{\pm}W^{\pm}jj$ processes.

In the $8\,\mathrm{TeV}$ analysis, it was found that the interference between electroweak and strong production increase the total combined cross section by $(12 \pm 6)\%$ in the inclusive region and $(7 \pm 4)\%$ in the VBS region [7]. The total SM prediction for the signal cross section in the inclusive region is $1.52 \pm 0.11\,\mathrm{fb}$ and $0.95 \pm 0.06\,\mathrm{fb}$ in the VBS region which includes electroweak and interference contributions.

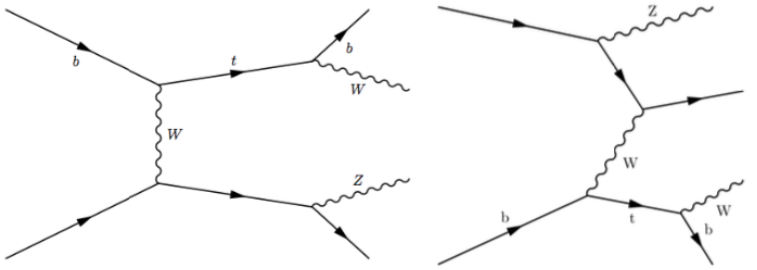


FIGURE 6.5: Representative Feynman diagrams of the tZj process, which produces WZ + jets in the final state due to the top quark decay [81].

### 6.4.2 Prompt background simulation

The prompt lepton backgrounds are estimated from MC simulations. As mentioned before, the $W^{\pm}Zjj$ process accounts for 90% of the total prompt background [81]. These samples are simulated with Sherpa, taking into account both the strong and electroweak production mechanisms, and normalised to the NLO calculation in QCD from VBFNLO in each of the fiducial regions. However, the normalisation of the electroweak contribution of the $W^{\pm}Z$ process has an additional complication. This cross section has a contribution from the associated production of a top quark with a Z boson and an additional parton, leading to the production of a W boson in the subsequent top decay. This contribution is taken into account in Sherpa, whereas the VBFNLO calculation neglects it due to the requirement of a $b$ quark in the initial state. Figure 6.5 shows this class of diagrams that accounts for a third of the total events in the fiducial regions. The contribution from the $tZj$ process is therefore taken into account with the Sherpa prediction.

Prompt leptons from the ZZ + jets process are modelled with Sherpa, while samples for the $t\bar{t}+V$, where $V = W, Z$, processes are simulated with Madgraph and showered with Pythia. Separate samples are generated for different numbers of jets present in each sample. Several $t\bar{t}$ samples are used for various consistency checks as well as prompt subtraction in the data-driven background estimation and was generated by Powheg. In addition, single-top production in the s-channel and Wt channel is also produced by this generator. Sherpa also generates the Z + jets and W + jets samples used in this analysis.

For all diboson samples simulated with Sherpa, the CT10 PDF set is used. In addition, the decay of $\tau$-leptons is treated with Sherpa's parton shower algorithm, while $b$ and $c$-quarks are explicitly treated as massive.

### 6.4.3 Charge mis-ID estimation

The dominant process contributing to the charge mis-identification background is where one prompt electron radiates due to hard brehmsstralung

leading to the photon converting into an electron-positron pair in the detector. This background is estimated by using a data-driven method. The electron charge misidentification rate is measured by making use of a data sample enriched with $Z \to e^+e^-$ events. Conversely, the muon charge misidentification rate has been found to be negligible. The estimated background is determined by applying the electron charge misidentification rate to the selected data, while using all selection criteria. However, the lepton's charges are required to be of opposite electric charge rather than same electric charge. An additional energy correction must also be applied to the reconstructed electron momentum, to take into account the loss of energy due to brehmsstrahlung and the subsequent conversion. This energy correction is derived from simulation.

Included in the background due to photon conversions are the contributions from the $W\gamma$ process, which includes both electroweak and strong production mechanisms. Whether these contributions will be included in the $13\,\mathrm{TeV}$ analysis remains to be decided. For the $8\,\mathrm{TeV}$ analysis, both contributions were estimated by making use of MC simulations: the strong production was simulated using Alpgen [126], while the electroweak production of $W\gamma jj$ was estimated by using Sherpa. For both samples the CTEQ6L1 PDF [127] set were used.

### 6.4.4 Non-prompt simulation and estimation

A fake factor data-driven method is used to estimate the non-prompt background. The fake factor method estimates a fake rate from the ratio of the number of jets satisfying the loose lepton identification criteria in a jet enriched sample. This data sample require two jets in the final state, hence "di-jet" sample, which is selected with one tagging jet passing nominal selection criteria defined in Section 6.3 and one loose or tight lepton that are back-to back in the azimuthal plane such that $\Delta\phi(l, j) > 2.8$. Definitions of tight and loose leptons are found in Tables 6.1, 6.2, 6.3 and 6.4. In addition, the transverse mass of the lepton and the missing transverse momentum is required to be within $M_T(l, E_T^{miss}) < 40\,\mathrm{GeV}$ to reduce contributions from the W + jets process. By requiring the leptons to be back-to-back with the jet, it can be safely assumed that the lepton originated from a hadronic decay or a jet [111].

The fake rate can be calculated, which is defined as the ratio of the number of events in which a tight lepton passes the tight selection criteria, to the number of events in which the lepton passes the orthogonally defined loose lepton selection criteria.

$$f_{lepton} = \frac{N_{Tight}}{N_{Loose}} \tag{6.2}$$

Once the fake factor has been measured as a function of loose lepton $p_T$ and $|\eta|$, the contribution of the fake leptons in the signal region is estimated by applying the fake factors to a "tight + loose" sample. The "tight + loose" sample is defined by the same selection criteria as the signal region, however one of the leptons are required to be a loose non-isolated lepton. Since it is more likely for a fake lepton to fail the isolation or lepton

quality requirements, it is very likely that the loose selected lepton is a mis-reconstructed jet. Therefore, it is important to choose a set of loose lepton criteria such that there are reasonable statistics in the tight + loose region.

The non-prompt estimations are calculated by scaling each event by $f_{lepton}$ according to the kinematic properties of the selected loose lepton as shown below:

$$N_{fake\ bkg} = f_{lepton} \times N_{Tight+Loose}. \tag{6.3}$$

To avoid double-counting, contributions from prompt leptons in the di-jet sample are subtracted from the MC estimations as well as data. Several $t\bar{t}$ samples are used for consistency checks and the prompt subtraction. Powheg v2 is used to simulate these samples, as well as single top production in the s-channel for W$t$ channel.

## 6.5 Systematic uncertainties

Background and signal estimations have several associated sources of systematic uncertainty. Estimations based on MC predictions can be categorised according to two main groups: uncertainties due to the theoretical cross section which are used to normalise the MC and uncertainties on the correction factors that are applied for reconstructed objects in MC to agree more accurately with data. Estimations based on data-driven methods arise from statistical uncertainties and method bias. The following sections describe various sources of systematic uncertainties associated with estimations based on MC and data-driven methods. The reader is referred to [6] for further discussions, which have been summarised below.

### 6.5.1 Uncertainties due to theoretical modelling

Three quarters of the total predicted events in the signal region consist of the $W^{\pm}W^{\pm}jj$ and $W^{\pm}Zjj$ processes. It is therefore necessary to have an adequate understanding of the uncertainties on the cross sections of these processes, in order to accurately compare MC predictions with data. Sources of uncertainty include the uncertainty on the parton distribution function of the proton, the dependence of the calculated cross section on the choice of renormalisation and factorisation scales and the dependence of event kinematics in the showering model. Another source of uncertainty is the difference between cross sections calculated by Powhegbox and VBFNLO. Dominant uncertainties for the electroweak production process are the parton shower and generator uncertainties, while the dominant uncertainties for the strong production process are scale variations.

### 6.5.2 Uncertainties due to object reconstruction

Systematic uncertainties on the estimated MC backgrounds are derived from the correction factors, energy smearing, $E_T^{miss}$ modeling [97] and the $b$-tagging efficiency and mistag rate [87]. Other sources of uncertainties for estimations based on MC are associated with the simulation of the interaction between particles produced in a proton-proton collision. The reconstructed objects have uncertainty on their energy resolution scale, as well

as an associated uncertainty with the efficiency of the selections for particle identification [94] [92]. In addition, there is also uncertainty applied to MC samples to cover the differences in efficiency between the trigger in data and the trigger in MC simulations. Another source is the uncertainty in the integrated luminosity, which affects the overall normalisation of both signal and background processes in MC samples. A list of various additional sources of associated systematic uncertainties is given below:

- Jet energy scale and resolution.
- Jet vertex cut efficiency.
- Jet $b$-tag inefficiency.
- Electron energy scale and resolution.
- Muon momentum scale and resolution.
- Electron identification efficiency.
- Muon identification efficiency.
- Identification efficiency for leptons passing the veto selection.
- Single lepton trigger efficiencies.
- $E_T^{miss}$ scale and resolution.

### 6.5.3 Uncertainties associated with data-driven methods

The total uncertainty associated with the estimation of non-prompt backgrounds depends on the region as well as the channel. The dominant systematic uncertainty is due to prompt lepton contamination in the di-jet sample used to estimate the fake factor. Another source of uncertainty is the difference in flavour composition between jets in the tight + loose region and jets in the di-jet sample. Other sources of uncertainty include variations in the sample used to calculate $f_{lepton}$, the uncertainty from extrapolating the fake factor into the signal region and statistical uncertainties in the number of tight + loose events.

Dominant systematic uncertainties associated with the estimation of backgrounds due to photon conversions include the possible method bias, as well as the statistical uncertainty in the estimated charge mis-identification rate which arises from limited statistics. Other sources of uncertainty include the uncertainty on the energy loss correction and potential double counting of charge mis-ID in processes that can produce both opposite sign lepton pairs and same sign lepton pairs without any charge mis-ID.

## 6.6 Control Regions

The modelling of MC background predictions must be validated in several same electric charge di-lepton control regions. Control regions are regions used to test MC predictions of background processes by specifically

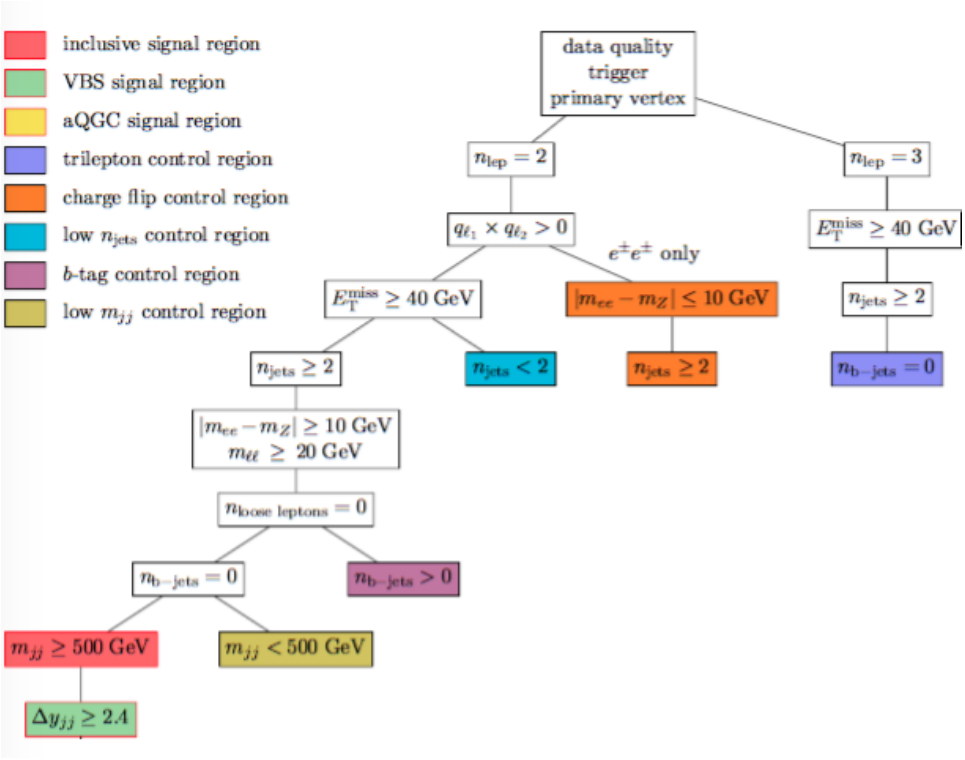


FIGURE 6.6: Selection criteria for signal regions as well as various control regions that were defined by the 8 TeV analysis [128]. The current 13 TeV analysis implements similar selection criteria.

selecting a region where a certain background process of interest is dominant. The sections below briefly describe the definitions of four of the most important control regions, while the selection criteria for each region are graphically presented in Figure 6.6. Additional discussions can be found in [6] [43], which were te main sources of reference.

### 6.6.1 Trilepton CR

Prompt backgrounds are tested in a trilepton control region, specifically tests the description of jet kinematics for WZ and ZZ samples. The control region is defined by requiring an additional lepton together with the two same electric charge leptons, while the third lepton passes the veto-lepton requirements. The final $|\Delta y_{ij}|$ and $m_{jj}$ selection criteria are dropped in order to gain more events.

### 6.6.2 Low $N_{jet}$ CR

The kinematics of leptons from WZ/ZZ samples, where one of the leptons from the Z boson decay are not reconstructed, are tested in a low $N_{jet}$ control region. This control region is defined by requiring less than two jets in an event. Consequently, the selection criteria making use of jet-based quantities, such as $|\Delta y_{ij}|$ and $m_{jj}$, are not required. This control region is also used to test data-driven predictions for fake and charge-misID backgrounds in a region dominated by the W + jets and Drell-Yan processes.

### 6.6.3 Low $m_{jj}$ CR

Final background predictions are tested in the low $m_{jj}$ control region where the background composition is similar to the signal regions. The CR is defined by inverting final di-jet invariant mass to rather be $m_{jj} < 500\,\text{GeV}$ and dropping the final $|\Delta y_{ij}|$ selection.

### 6.6.4 $b$-tagged CR

Non-prompt leptons originating from $t\bar{t} \to l\nu jjb\bar{b}$, $t\bar{t}+W/Z$ and other non-prompt backgrounds are tested in the $b$-tagged control region. The defining process that produces events with at least one fake lepton is semi-leptonic $t\bar{t}$. Therefore, this region is defined by inverting the $b$-veto requirement and selecting events containing at least one jet that has been identified as a $b$-jet. By requiring a $b$-tagged jet in the event selection for this control region, events from non-prompt backgrounds originating from $t\bar{t}$ processes are specifically selected. The $|\Delta y_{ij}|$ and $m_{jj}$ selection criteria are also dropped. This control region is used to test the description of event kinematics for the charge misID background as well as the fake background, where jets are mis-reconstructed as charged leptons. Current studies for the current $\sqrt{s} = 13\,\text{TeV}$ analysis will be discussed in the following section.

## 6.7 Current studies of the $b$-tagged CR

Studies of the $b$-tagged CR for the Run II $W^{\pm}W^{\pm}jj$-EW analysis are still ongoing at the time of the writing of this thesis. Currently, the agreement between data and MC in this region is extremely poor for the nominal background, which requires two tight leptons. The discrepancy is especially evident in the $\mu\mu$ channel where the low statistics are slightly problematic, in addition to the lack of truth events originating from the $t\bar{t}$ process. Another study investigating the truth origins of fake leptons in $t\bar{t}$ processes also observed a low fraction of $t\bar{t}$ events in the $\mu\mu$ channel [129]. The notably low fraction of $t\bar{t}$ events in the $\mu\mu$ channel is demonstrated in the transverse momentum distribution of the leading leptons in Figure 6.7. Figures 6.8 and 6.9 shows the number of jets and $b$-tagged jets in the $b$-tagged CR. From these plots, it can be seen that the modelling of these variables in $\mu\mu$ channel $b$-tagged CR is not very well-understood. It should be noted that a $b$-tagger identifying $b$-jets with a 70% efficiency working point is implemented, since it was shown in a previous study that this value is the optimal working point to suppress the fake lepton background [130]. Generally, backgrounds from $t\bar{t}$ processes are modelled with the data-driven fake factor method, due to the MC modelling's inability to adequately describe this process. The exact reason for the inadequate MC modelling of the non-prompt background is investigated by this thesis.

To investigate this discrepancy between data and MC, the composition of the fake background in the tight + loose sample of the $b$-tagged CR is examined. Besides the agreement between MC and data being slightly better in the tight + loose region, the $\mu\mu$ channel also shows a definite improvement. This is due to the increased contribution from the $t\bar{t}$ process that is now included in the CR. Correspondingly, the region is heavily dominated

by the $t\bar{t}$ process, as it should be. The increased number of events from the $t\bar{t}$ process is shown in Figures 6.10, 6.11 and 6.12. By selecting a tight and a loose muon, the number of jets and $b$-tagged jets also increase, however the total number of events are still low. The selection criteria of the loose leptons therefore play a crucial role in the estimation of the fake lepton backgrounds. Since the only differences between a tight and a loose muon is the isolation and transverse impact parameter requirements, these variables are investigated to find any possible mis-modelling of the MC.

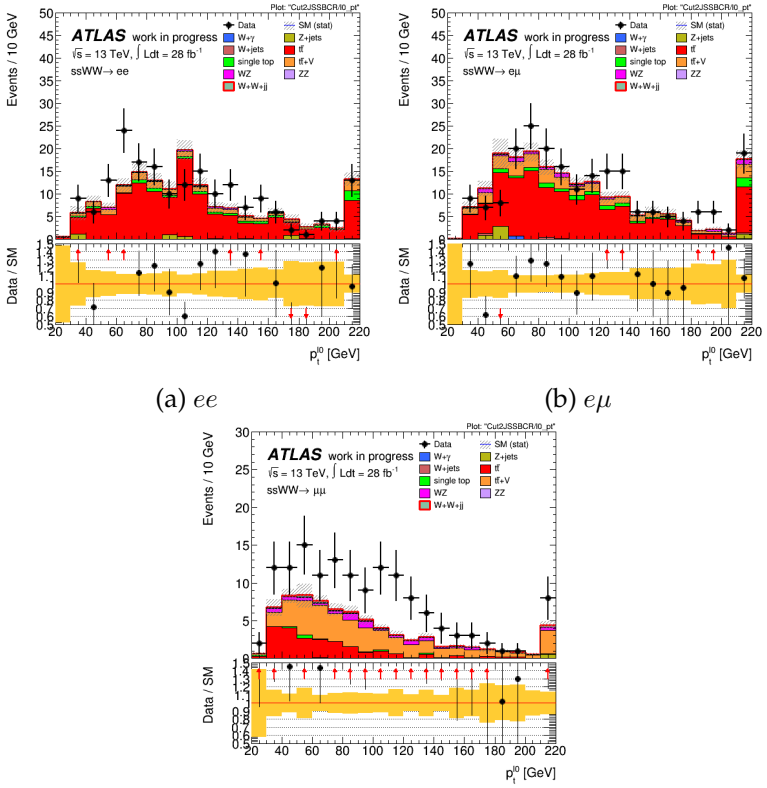


(a) $ee$ (b) $e\mu$

(c) $\mu\mu$

FIGURE 6.7: Transverse momentum distributions of the leading lepton in the $b$-tagged control region in the: (a) $ee$ channel, (b) $e\mu$ channel and (c) $\mu\mu$ channel.

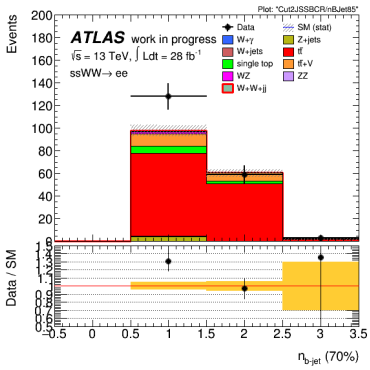


(a) $ee$

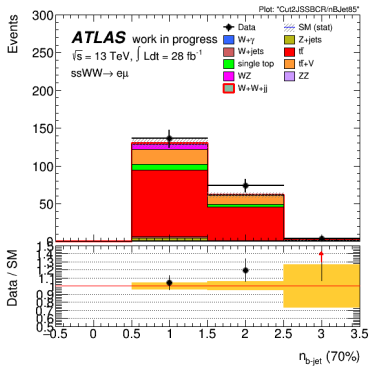


(b) $e\mu$

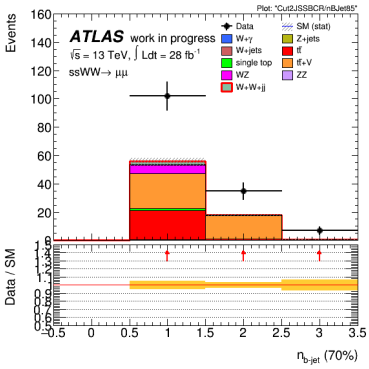


(c) $\mu\mu$

FIGURE 6.8: Number of $b$-tagged jets in the $b$-tagged control region in the: (a) $ee$ channel, (b) $e\mu$ channel and (c) $\mu\mu$ channel.

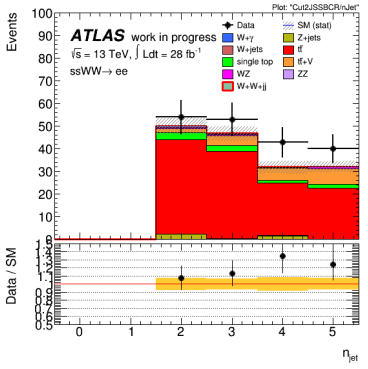


(a) $ee$

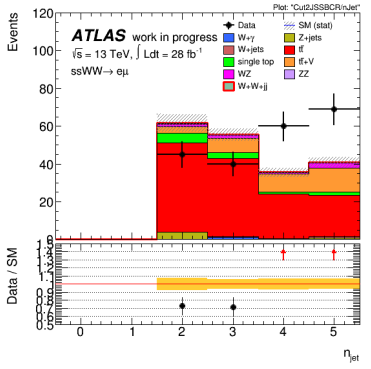


(b) $e\mu$

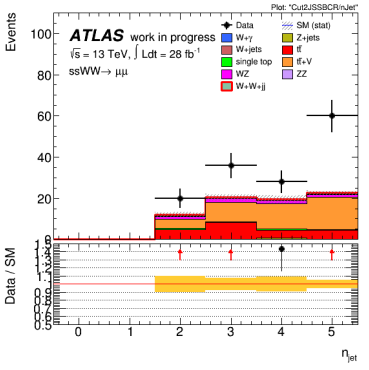


(c) $\mu\mu$

FIGURE 6.9: Number of jets for each channel in the $b$-tagged control region in the: (a) $ee$ channel, (b) $e\mu$ channel and (c) $\mu\mu$ channel.

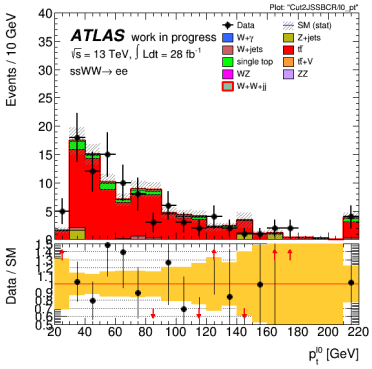


(a) $ee$

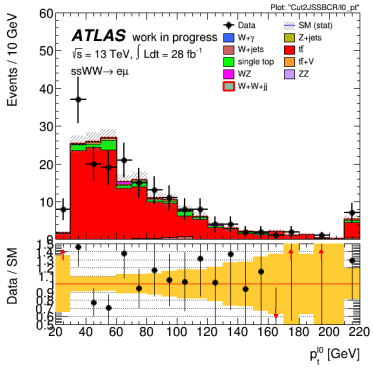


(b) $e\mu$

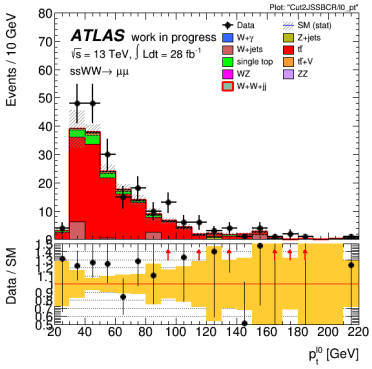


(c) $\mu\mu$

FIGURE 6.10: Transverse momentum distributions of the leading lepton in the tight + loose sample of the $b$-tagged control region in the: (a) $ee$ channel, (b) $e\mu$ channel and (c) $\mu\mu$ channel.

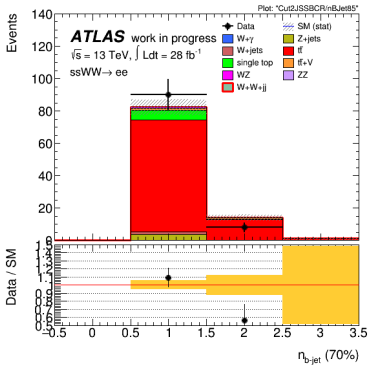


(a) $ee$

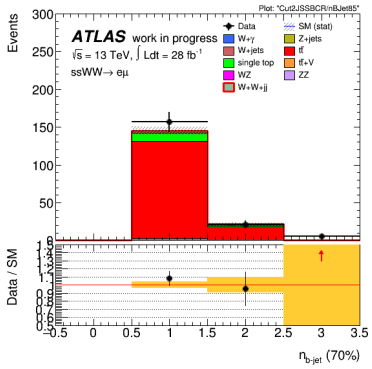


(b) $e\mu$

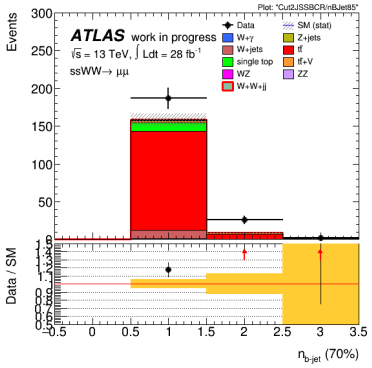


(c) $\mu\mu$

FIGURE 6.11: Number of $b$-tagged jets in the tight + loose sample of the $b$-tagged control region in the: (a) $ee$ channel, (b) $e\mu$ channel and (c) $\mu\mu$ channel.

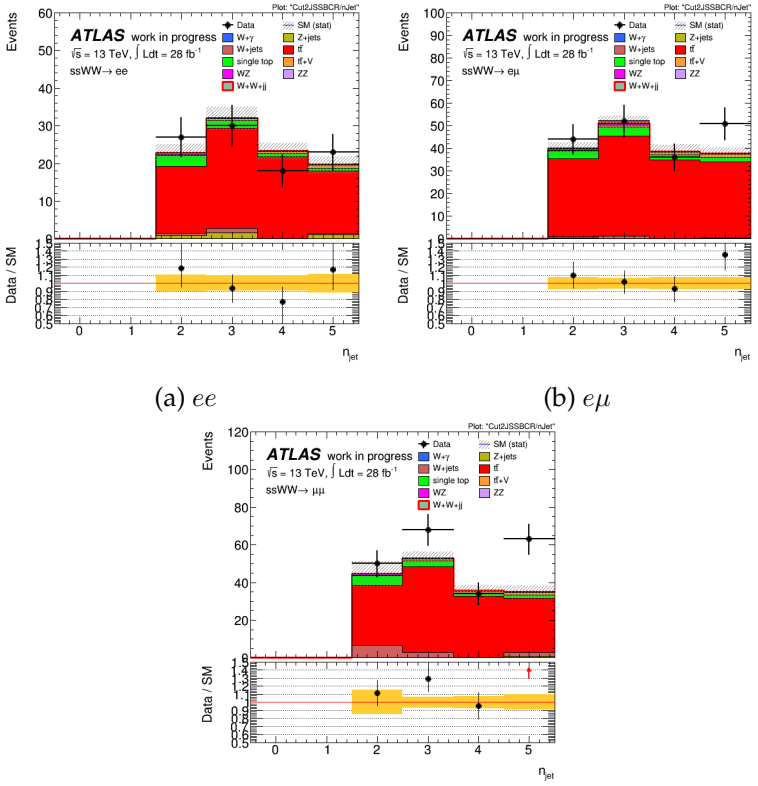


(a) $ee$ (b) $e\mu$

(c) $\mu\mu$

FIGURE 6.12: Number of jets in the tight + loose sample for the $b$-tagged control region in the: (a) $ee$ channel, (b) $e\mu$ channel and (c) $\mu\mu$ channel.

TABLE 6.6: Classification scheme of particle origins

| Integer | Particle origin |
|---|---|
| 5 | Photon conversion |
| 10 | top |
| 12 | W |
| 13 | Z |
| 26 | B meson |
| 33 | B baryon |

To investigate the isolation and transverse impact parameter requirements for the loose leptons a control selection is defined. This selection is referred to as a "mod-tight" lepton. The selection criteria for a mod-tight lepton included the selections for loose electrons or muons, however the isolation requirement is not applied together with the loose muon requirement for the transverse impact parameter. Generally, the data and MC with the tight + loose selection still agrees better than this selection where no isolation is required, shown in Figures 6.13, 6.14 and 6.15. The amount of jets and $b$-tagged jets are still low in the $\mu\mu$ channel in the $b$-tagged control region.

Since a pre-selection cut on the transverse impact parameter is already applied to the MC samples used in this analysis at the production step, different MC samples without the selection cut will have to be studied in order to investigate the loose transverse impact parameter variable. Creating new samples at production level is beyond the scope of this thesis and only the effect of varying the isolation requirement on the mod tight control selection was examined.

Varying the isolation requirement on the control mod tight selection suggests that the gradient isolation requirement vetoes the majority of events originating from the $t\bar{t}$ process in the $\mu\mu$ channel. Upon further investigation it was determined that the majority of sub-leading leptons originating from the $t\bar{t}$ process do not, in fact, pass the gradient isolation requirement. The leading and sub-leading leptons passing and failing the gradient isolation working point can be seen in Figure 6.16.

To further study the leading and sub-leading leptons in the $\mu\mu$ channel, the MC event record was investigated to determine the origins of the leading and sub-leading leptons in the $b$-tagged control region, as well as the tight + loose region. The leading and sub-leading MC origins in the $b$-tagged control region and the tight + loose sample of the $b$-tagged control region is shown in Figures 6.17 and 6.18, respectively. In addition, the integer classification scheme for particle origins have been summarised in Table 6.6. From the plots of the tight + loose region it can be seen that the largest background contribution is due to the $t\bar{t}$ and single top processes, in which the leading leptons originate from W bosons and the sub-leading leptons originate from B mesons. Furthermore, it can be seen in the plots of the

$b$-tagged control region, in which two tight leptons are selected, that this region is no longer dominated by leptons originating from the $t\bar{t}$ and single top processes, but rather the $t\bar{t}+V$ process. Therefore, the isolation requirement for leptons suppresses the large amount of leading and sub-leading leptons originating from W bosons and B mesons from the $t\bar{t}$ process. A similar trend can be seen in all three channels, however the suppression is the most severe in the $\mu\mu$ channel.

With the addition of the isolation requirement for leptons, the the discrepancy between data and MC becomes even worse in the $b$-tagged control region, especially since the MC is underestimated with respect to the data. This observation suggests that even though the isolation requirement suppresses the MC non-prompt backgrounds quite well, this is not the case for the data. Hence the poor agrrement between data and MC in the $b$-tagged control region.

Further investigations of this region are still ongoing. It is crucial to construct a well-understood region with the loose lepton selection criteria, since these loose leptons will determine the purity of the data sample used to determine the non-prompt background.

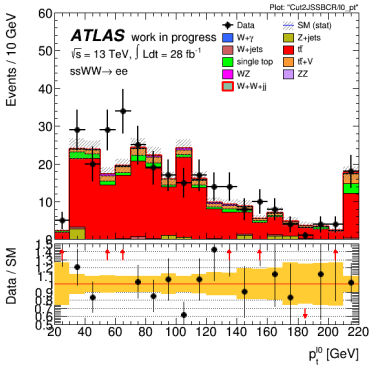


(a) $ee$

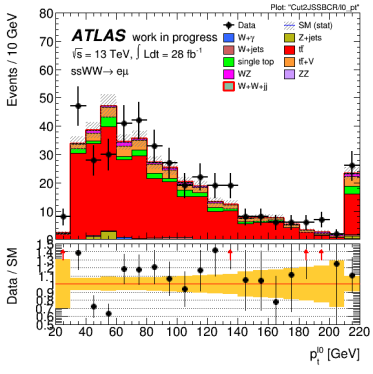


(b) $e\mu$

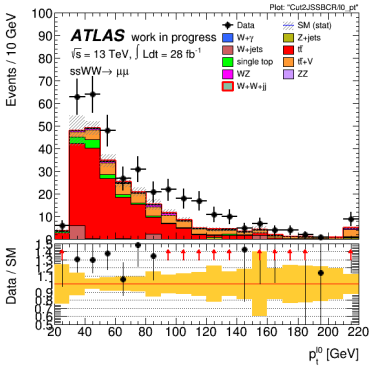


(c) $\mu\mu$

FIGURE 6.13: Transverse momentum distributions of the leading lepton with the mod selection in the $b$-tagged control region in the: (a) $ee$ channel, (b) $e\mu$ channel and (c) $\mu\mu$ channel.

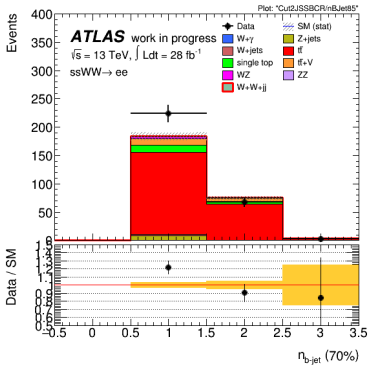


(a) $ee$

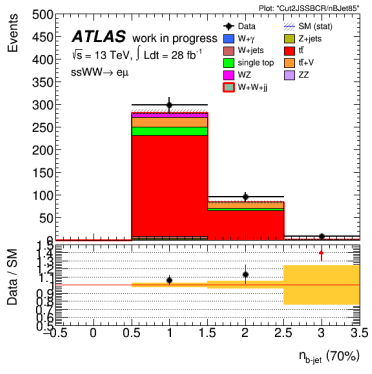


(b) $e\mu$

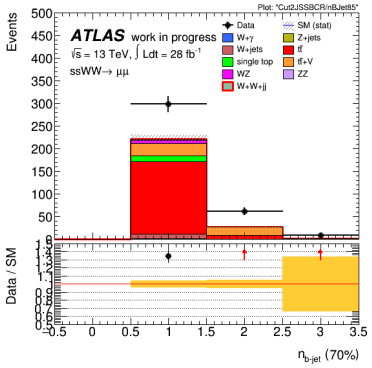


(c) $\mu\mu$

FIGURE 6.14: Number of $b$-tagged jets with the mod selection in the $b$-tagged control region: (a) $ee$ channel, (b) $e\mu$ channel and (c) $\mu\mu$ channel.

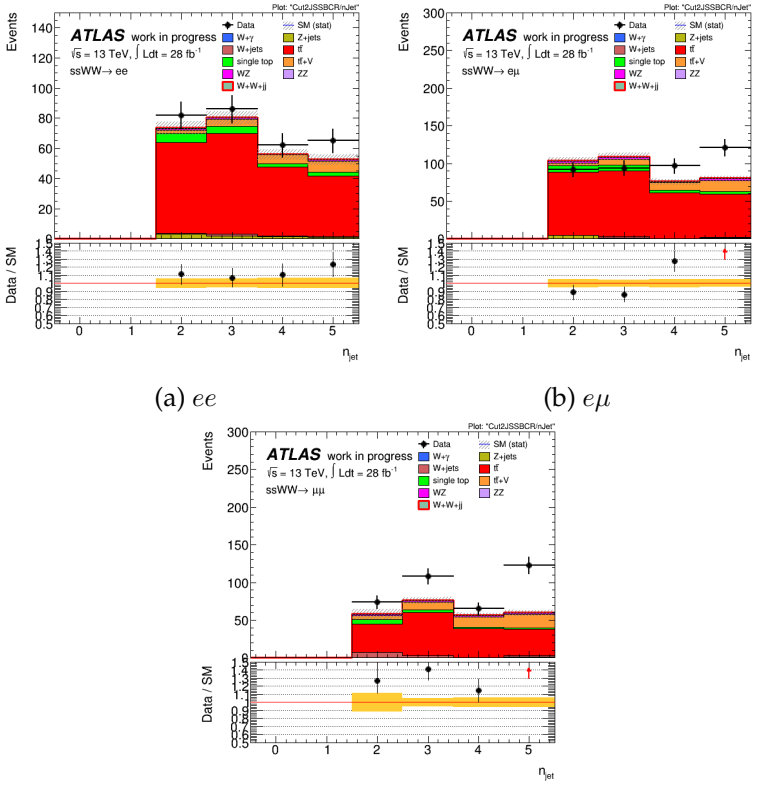


(a) $ee$ (b) $e\mu$

(c) $\mu\mu$

FIGURE 6.15: Number of jets with the mod selection in the $b$-tagged control region in the: (a) $ee$ channel, (b) $e\mu$ channel and (c) $\mu\mu$ channel..

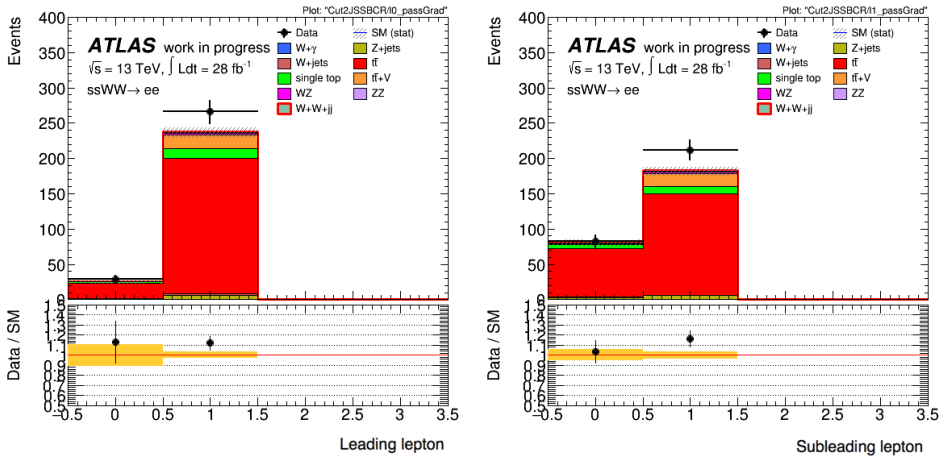


(a) $ee$

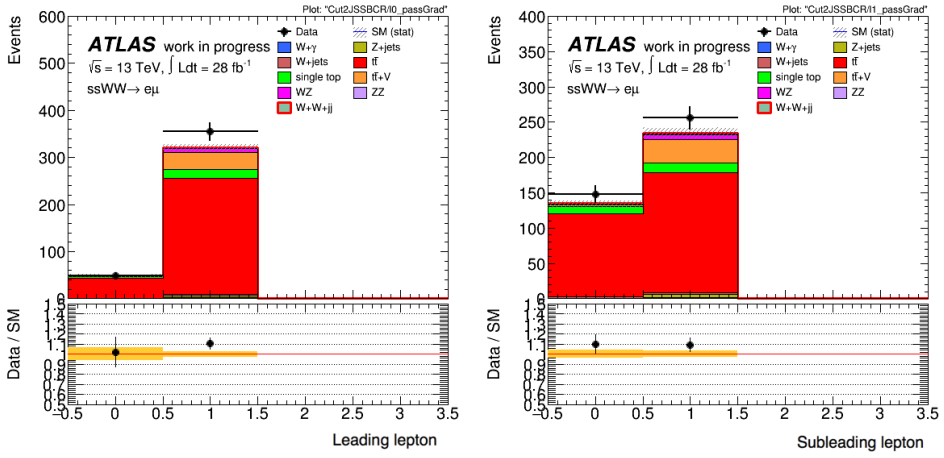


(b) $e\mu$

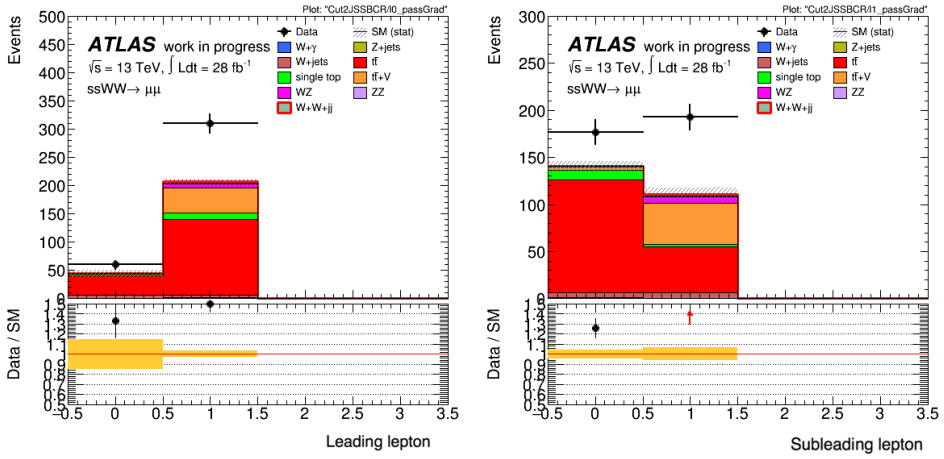


(c) $\mu\mu$

FIGURE 6.16: Leading (left) and sub-leading (right) leptons that pass or fail the gradient isolation requirement: (a) $ee$ channel, (b) $e\mu$ channel and (c) $\mu\mu$ channel.

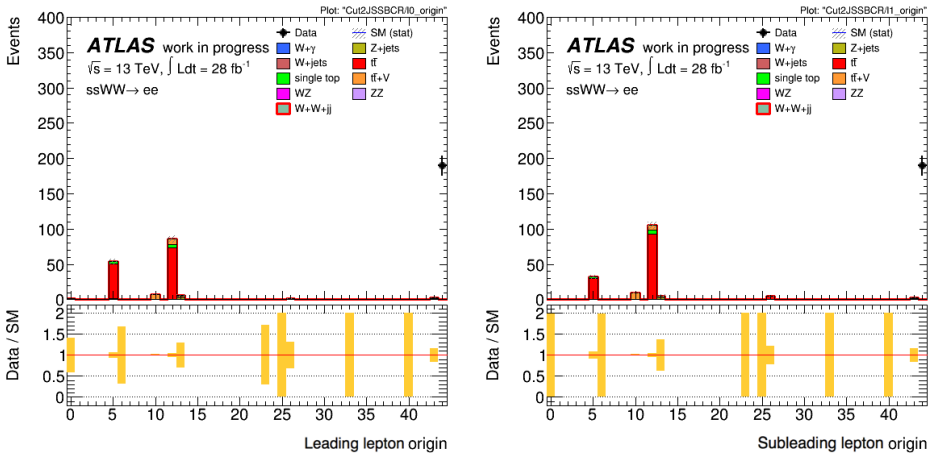


(a) $ee$

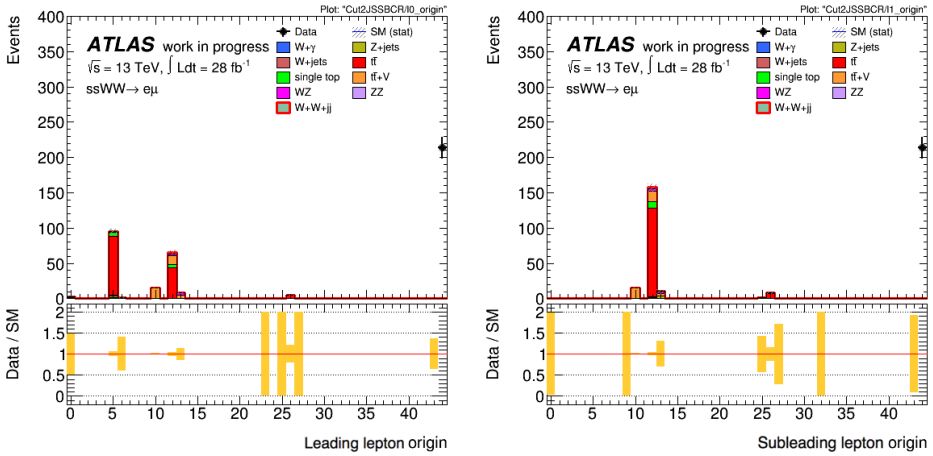


(b) $e\mu$

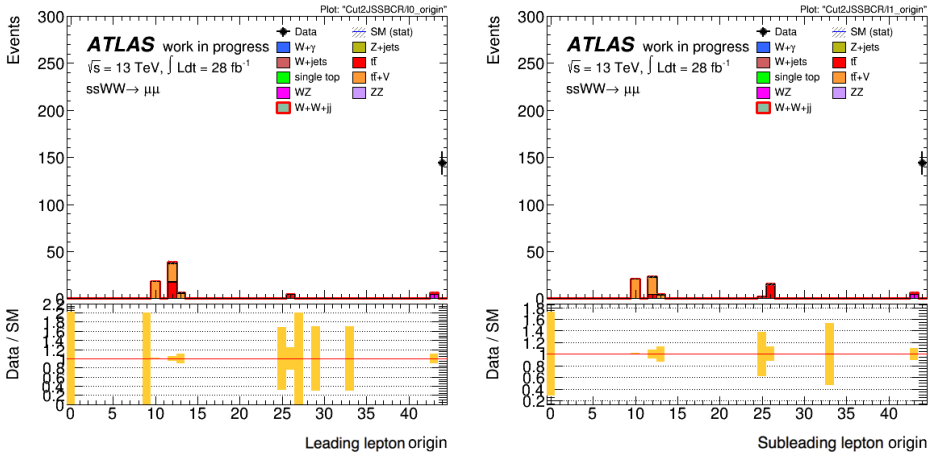


(c) $\mu\mu$

FIGURE 6.17: Leading (left) and sub-leading (right) lepton origins in the $b$-tagged control region in the: (a) $ee$ channel, (b) $e\mu$ channel and (c) $\mu\mu$ channel.

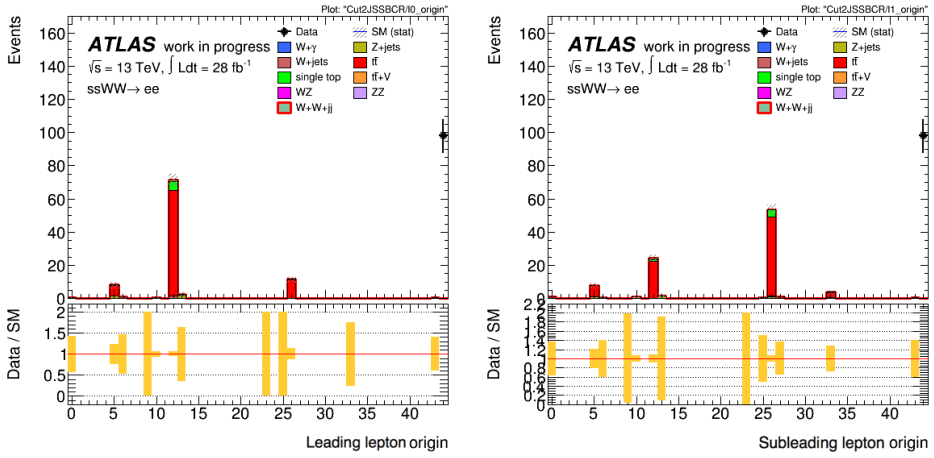


(a) $ee$

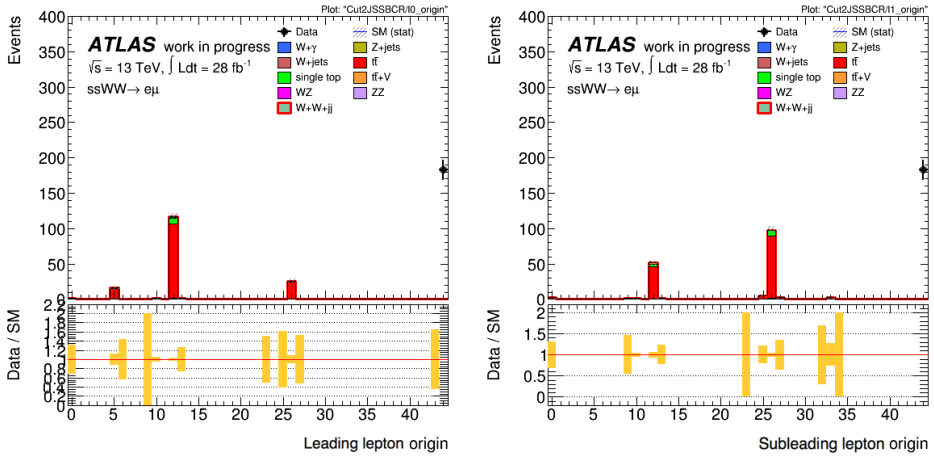


(b) $e\mu$

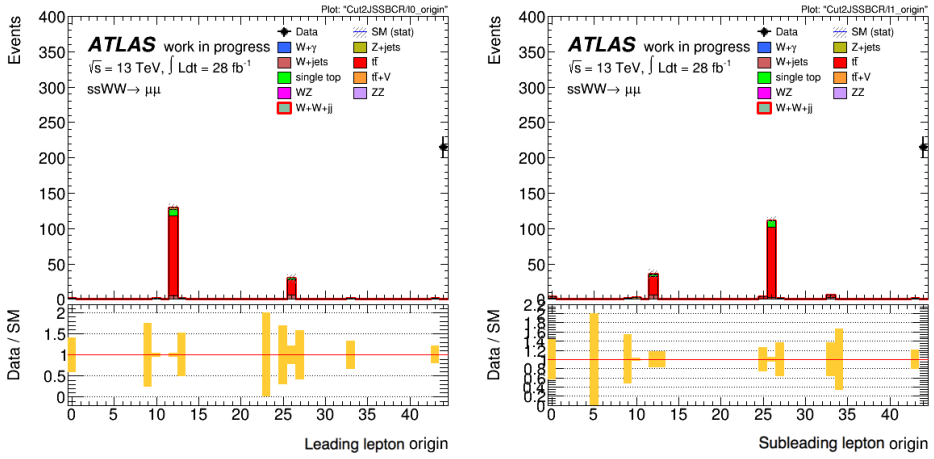


(c) $\mu\mu$

FIGURE 6.18: Leading (left) and sub-leading (right) lepton origins of the tight + loose sample in the $b$-tagged control region in the: (a) $ee$ channel, (b) $e\mu$ channel and (c) $\mu\mu$ channel.

# Chapter 7

# $W^{\pm}W^{\pm}$ scattering at the High Luminosity LHC

Since it is unclear whether the unitarization of WW scattering amplitudes is fully regulated by the SM Higgs boson and behaves according to the SM prediction at high energies, the study of the $W^{\pm}W^{\pm}jj$-EW process is an important task that will be extended to the High Luminosity LHC (HL-LHC) physics program. Successfully extracting a $W^{\pm}W^{\pm}jj$-EW measurement is dependent on the ratio of $W^{\pm}W^{\pm}jj$-EW and $W^{\pm}W^{\pm}jj$-QCD production. In addition, the cross sections for these processes, in turn, depend on the centre of mass energy of $pp$ collisions. The expected ratio in a VBS-like phase with $M_{qq} > 500\,\mathrm{GeV}$ has been shown to increase from $\approx 1.2$ at $\sqrt{s} = 8\,\mathrm{TeV}$ to $\approx 1.5$ for a centre of mass energy of $14\,\mathrm{TeV}$ [111] (Figure 7.1). Therefore, the extraction of the $W^{\pm}W^{\pm}jj$-EW signal will be simplified, due to the fact that the QCD only component of this process will be slightly more diminished.

As mentioned before in previous chapters, the instantaneous luminosity will increase during the operation of the HL-LHC. An increase of instantaneous luminosity will result in an increased pileup interactions per event, which lead to the requirement of new techniques for object reconstruction and particle identification. The increased amount of pileup interactions will pose quite a challenge for the measurement of $W^{\pm}W^{\pm}$ scattering process with respect to the forward tagging jets, since VBS processes are characterised by two, high-$p_T$ forward jets. Pileup jets refer specifically to jets that originated from additional collisions within the same bunch crossing. In order to eliminate pileup jets in the forward regions of the detector, the prospect of extending the tracking detector to a large $|\eta|$ of $4.0$ have been considered.

Finally, well-understood estimates of the contributions from other backgrounds at increased centre of mass energies will also be necessary to determine the potential of extracting the electroweak only contribution of $W^{\pm}W^{\pm}$ scattering at the HL-LHC. The differing dependencies of the cross sections of various background processes may lead to different background contributions at higher energies.

The prospects for a $W^{\pm}W^{\pm}jj$-EW measurement after the LHC and ATLAS detector upgrades, with a main focus on the extended ITk system, will be investigated in this chapter. Previous studies have been carried out by [131], [111] and [132]. This thesis makes use of the methodology employed

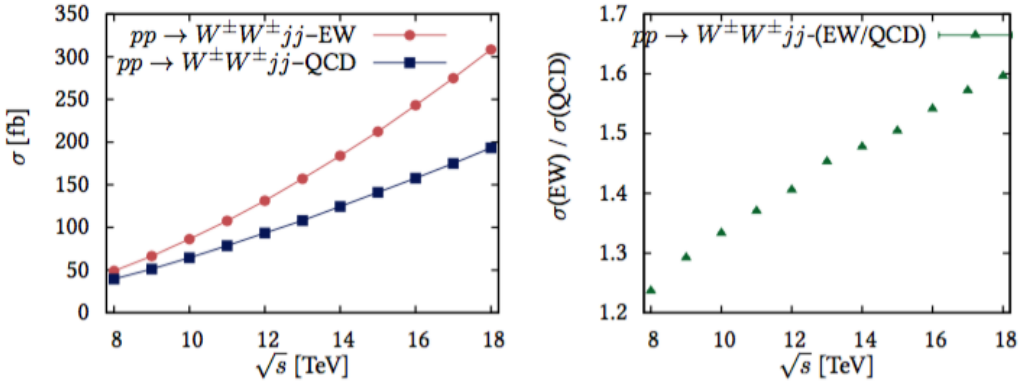


FIGURE 7.1: Cross section for $pp \to W^{\pm}W^{\pm}jj$ with respect to centre of mass energy of $pp$ collisions. An invariant mass cut of $M_{qq} > 500\,\text{GeV}$ has been applied. Left: Purely electroweak production cross sections compared to the difference between inclusive and electroweak cross sections at different $pp$ centre of mass energies. Right: Ratio of the two cross sections shown on the left [111].

by the study described in [132]. Firstly, the MC samples used for signal and backgrounds will be discussed followed by the application of the upgrade performance functions to the truth-level particles. Next, the object and event selection criteria will be summarised. Finally, results will be presented and the effect of an extended Inner Detector tracking system will be discussed. In addition, the effect of a forward muon-tagger will be investigated by raising the acceptance threshold for loose muons. Lastly, an additional background sample was implemented into the analysis, since an approximation estimated most of the other backgrounds.

## 7.1 $W^{\pm}W^{\pm}jj$-EW at $14\,\text{TeV}$

### 7.1.1 Monte Carlo samples

Signal and background processes are modelled with MC generators at a centre of mass energy of $14\,\text{TeV}$ with the number of events scaled to an integrated luminosity of $L = 3000\,\text{fb}^{-1}$. The $W^{\pm}W^{\pm}jj$-EW and $W^{\pm}W^{\pm}jj$-QCD production processes are simulated with Madgraph aMC@NLO interfaced with Pythia 8 for parton showering, hadronisation and the underlying event modelling. The dominant background process, WZ + jets production, is simulated using Sherpa v2.2.0, with NLO accuracy in $\alpha_s$ for up to one associated parton and LO accuracy for two or three partons in the final state. Included in the WZ + jets background estimate is both the strong and electroweak production mechanisms of this process. Additional $pp$ pile up interactions, with an average of 200 interactions per bunch crossing, are generated with Pythia 8 and added event-by-event to simulated samples.

Other background processes that could mimic the final state of $W^{\pm}W^{\pm}jj$ are not simulated. Rather, the contributions from these processes are estimated by making use of the background contributions observed in the

TABLE 7.1: Gaussian widths used to smear energy and momenta of truth particles [109] [108].

| **Object** | **Gaussian width** |
|---|---|
| Muons | $\sigma_{ID} = p_T\sqrt{a_1^2 + (a_2 p_T)^2}$ |
| | $\sigma_{MS} = p_T\sqrt{\frac{b_0}{p_T}^2 + b_1^2 + (b_2 p_T)^2}$ |
| | $\sigma_{CB} = \frac{\sigma_{ID}^2\sigma_{MS}^2}{\sqrt{\sigma_{ID}^2 - \sigma_{MS}^2}}$ |
| Jets | $\frac{\sigma_{pT}}{p_T} = \sqrt{\frac{N^2}{p_T^2} + \frac{S^2}{p_T} + C^2}$ |
| | with $N = a(\lvert\eta\rvert) + b(\lvert\eta\rvert)\mu$ |

$\sqrt{s} = 8\,\text{TeV}$ $W^{\pm}W^{\pm}jj$ analysis [7] [6]. The total background contribution is estimated by summing the final event yields from the $W^{\pm}W^{\pm}jj$-QCD and WZ + jets processes and scaling the result to account for the non-simulated background contributions. Scale factors were derived from the relative background composition observed in the $8\,\text{TeV}$ analysis and calculated for individual channels. The calculated scale factors are 2.17, 1.17 and 1.75 for the $ee$, $\mu\mu$ and $e\mu/\mu e$ channels, respectively, while the scale factor for the combined channels is 1.71 [132].

### 7.1.2 Application of upgrade performance functions

Detector effects are taken into account by making use of performance functions that are parametrised by the response of the upgraded detectors, mentioned in Chapter 4. To modify the kinematics of different physics objects, various efficiencies are applied by making use of random numbers generated from probability density functions provided by the performance functions. Once the reconstruction and trigger efficiencies have been estimated and the momenta have been smeared accordingly, object and event selection cuts are applied which will be discussed in Section 7.1.3.

#### Detector resolution

The performance functions take into account the energy and momentum resolutions of the detector for the kinematics of jets, electrons and muons. This is achieved by generating a random number from a Gaussian distribution with a mean of 1.0 and a width shown in Table 7.1. After the resulting factor has been obtained, it is used to smear the energy and momentum of the relevant particle.

For electrons, the performance functions utilise two dimensional maps which use the electron's transverse momentum and pseudorapidity as inputs to obtain detector and reconstruction efficiencies to smear the energy and transverse momenta of electrons. Results of these studies that has been implemented in the performance functions can be seen in [10]. On the other hand, the energy and transverse momenta of muons are smeared with the factor obtained from a Gaussian with a width that combines the properties of the ID ($\sigma_{ID}$) and the MS ($\sigma_{MS}$). The ID provides two parameters which are

TABLE 7.2: Reconstruction efficiencies for muons.

| **Pseudorapidity bin** | **Reconstruction efficiency** |
|---|---|
| 0.1 | 0.54 |
| $2.5 < \|\eta\| < 2.7$ | 0.97 |
| 4.0 | 0.95 |

given in 15 $|\eta|$ regions, while the MS provides three parameters, given in two $|\eta|$ regions corresponding to the barrel and end cap regions.

Similarly, the energy and transverse momenta of jets are also smeared with the use of a factor obtained from a Gaussian and a width which takes into account $\eta$-dependant noise, stochastic fluctuations and constant uncertainties. Only the noise term is a function of the number of pileup interactions, $\mu$, which is generated from a Poissonian distribution with a mean of $\langle\mu\rangle = 140$ for each event.

**Reconstruction efficiencies**

After the detector performance has been taken into consideration, reconstruction efficiencies are utilised to determine whether an object can be reconstructed by the sub-systems. These reconstruction efficiencies are provided to estimate the fraction of particles that have been reconstructed and identified as the correct type of physics object. Similar to the detector resolution estimation, a random number $n_{reco}$ is generated for each particle from an uniform distribution, [0,1). In the case where $n_{reco} > \epsilon_{reco}$, it is assumed that the particle has not been reconstructed and is removed from the event.

Reconstruction efficiencies for muons and electrons have been studied under different pileup conditions for two working points, tight and loose, referring to criteria with low and high purity [10]. The reconstruction efficiencies corresponding to the tight working point for muons are shown in Table 7.2. For electrons, a similar strategy to obtain the detector resolution efficiencies are employed to obtain the reconstruction efficiencies. Further information on the reconstruction efficiencies for electrons are also found in [10].

The reconstruction efficiencies for jets is estimated by studying the efficiency of the track confirmation algorithm with different values of $\mu$ and extrapolating the performance according to different bins of $p_T$ and $|\eta|$. These values were studied and reported in the Scoping Document [10].

**Trigger efficiencies**

To determine whether the selected leptons have activated the trigger which would result in the event being recorded on disk, trigger efficiency estimates are used for single electrons, muons and jets (Table 7.3). Similar to

the determination of whether a lepton was correctly constructed, a random number $n_{trigger}$ is generated again for each particle candidate from a uniform distribution, [0,1). This time, however, both $n_{reco} < \epsilon_{reco}$ and $n_{trigger} < \epsilon_{trigger}$ must be true in order for the event to pass the trigger requirement. All preselected loose leptons are required to activate the trigger in this analysis.

TABLE 7.3: Trigger efficiencies for single electrons and muons.

| **Object** | **Highest pseudorapidity bin** | **Trigger efficiency** |
|---|---|---|
| Electrons | $\leq 2.5$ | 0.95 |
| | $\leq 4.0$ | 0.90 |
| Muons | $< 1.05$ | 0.69 |
| | $1.05 < \|\eta\| < 2.4$ | 0.96 |
| Jets | $\|\eta\| < 3.2$ | 0.95 |

### 7.1.3 Object and event selection

Muon transverse momentum and electron energy resolution are parametrised as a function of $\eta$. These quantities are used to smear the truth level quantities of each object: transverse momentum for muons and energy for electrons. The missing transverse energy, $E_T^{miss}$, at particle level is defined as the transverse component of the vectorial sum of the final state neutrino momenta. Lepton trigger and identification efficiencies are derived as a function of $\eta$ and $p_T$. The efficiencies are then used to determine the likelihood that a lepton would pass the trigger or identification requirements. Final state particles with a lifetime that is longer than $30\,\mathrm{ps}$ are clustered into jets by making use of the anti-$k_t$ algorithm, with a radius parameter of $R = 0.4$. Final state muons and neutrinos are not included in the truth jet clustering. To avoid the double counting of jets associated with electrons, an additional overlap requirement is applied. This requirement excludes jets within a cone of $\Delta R_{e,j} < 0.2$ from an electron. Momenta of truth jets are smeared as a function of $\eta$ and $p_T$. The smearing functions, however, are not applied to pileup jets, since pileup events are passed through a full ATLAS detector simulation based on GEANT4.

Events are selected based on the experimental signature of the $W^{\pm}W^{\pm}jj$ scattering process. Events preselected by either a single-muon or single-electron trigger require transverse momentum of $25\,\mathrm{GeV}$ for leptons to be selected for the analysis. Additionally, muons and electrons with transverse momenta $p_T > 6$ and $7\,\mathrm{GeV}$ are also preselected and are defined as loose leptons. Several forward tracking scenarios are considered. In the case where no forward tracking is available, the leptons are restricted to $|\eta| \leq 2.7$, while in the case where forward tracking is available a scenario is considered where only electron reconstruction is available to $|\eta| \leq 4.0$. Recall that the nominal $|\eta|$-coverage of the MS is only out to $|\eta| \leq 2.7$. The

TABLE 7.4: Jet track confirmation and lepton pseudorapidity ranges for four scenarios evaluating the effect of an extended tracking system on the $W^{\pm}W^{\pm}jj$ measurement.

| Category | Track confirmation range | Lepton $\eta$ range |
|---|---|---|
| No forward tracking | $\lvert\eta_{jet}\rvert \leq 2.5$ | $\lvert\eta_{e,\mu}\rvert \leq 2.7$ |
| Forward tracking with jets only | $\lvert\eta_{jet}\rvert \leq 3.8$ | $\lvert\eta_{e,\mu}\rvert \leq 2.7$ |
| Forward tracking with jets and electrons | $\lvert\eta_{jet}\rvert \leq 2.5$ | $\lvert\eta_{e}\rvert \leq 4.0$, $\lvert\eta_{\mu}\rvert \leq 2.7$ |
| Forward tracking with jets, electrons and muons | $\lvert\eta_{jet}\rvert \leq 3.8$ | $\lvert\eta_{e,\mu}\rvert \leq 4.0$ |

TABLE 7.5: Selection criteria for $W^{\pm}W^{\pm}jj$-EW events.

| **Description** | **Selection requirement** |
|---|---|
| Lepton selection | Exactly 2 leptons with $p_T > 25\,\mathrm{GeV}$ |
| Dilepton charge and separation | $\Delta R_{l,l} \geq 0.3$, $q_1 \times q_2 > 0$ |
| Dilepton mass | $m_{ll} > 20\,\mathrm{GeV}$ |
| $Z_{ee}$ veto | $\lvert m_{ll} - m_Z\rvert > 10\,\mathrm{GeV}$ |
| $E_T^{miss}$ | $E_T^{miss} > 40\,\mathrm{GeV}$ |
| Jet selection and separation | At least two jets with $\Delta R_{l,j} > 0.3$ |
| Di-jet rapidity separation | $\lvert\Delta y_{ij}\rvert > 2.4$ |
| Third-lepton veto | 0 additional preselected leptons |
| Di-jet mass | $m_{jj} > 500\,\mathrm{GeV}$ |
| Lepton centrality | $> 0$ |

possibility of a forward muon-tagger is also considered, which would allow for both electron and muon reconstruction up to $|\eta| \leq 4.0$. In order to investigate the effect of a forward muon-tagger, the threshold $p_T$ for loose muons is chosen to be either the nominal value, $10\,\mathrm{GeV}$ or $15\,\mathrm{GeV}$.

For this analysis, jets with $p_T > 30\,\mathrm{GeV}$ and $|\eta| < 4.5$ have been considered. A selection requirement is applied to all jets with transverse momenta below $100\,\mathrm{GeV}$ in order to distinguish between jets resulting from a hard scatter interaction and pileup jets, which result from the accompanying soft scatter interactions. This requirement is based on track confirmation, which makes use of the fraction of the $p_T$ of the tracks from the associated hard scattering vertex to the jets. Selection criteria based on this requirement are applied over an $\eta$ region which is related to two different tracking scenarios. In the case where forward tracking is available, the selection criteria are applied for jets up to $|\eta| \leq 3.8$ and for jet up to $|\eta| \leq 2.5$ without any forward tracking. Significant contamination from pileup jets must be reduced by increasing the $p_T$ threshold for jets outside the tracking region from 30 to $70\,\mathrm{GeV}$. This figure was deduced from the $\eta$ and $p_T$ distributions of the fully simulated pileup jets in the events. Jets that pass the track confirmation requirements and $p_T$ threshold are preselected. The two jets with the highest transverse momenta are defined as the leading and sub-leading tag jets in the event.

An extended tracker therefore affects the leading and sub-leading jets and

leptons. The effect of this selection on the $W^{\pm}W^{\pm}jj$ measurement is compared in the four tracking scenarios summarised in Table 7.4. After the selection of jets and leptons, selection criteria based on the $8\,\mathrm{TeV}$ $W^{\pm}W^{\pm}jj$ analysis are applied to each event (Table 7.5). Since the decay products of a VBS event are expected to be found central to the tagging jets, the final state lepton pair should be at a smaller $\eta$ than the two tagging jets [133]. For this reason, an additional selection requirement on the lepton centrality, $\zeta > 0$, has been imposed to enhance the purity of the $W^{\pm}W^{\pm}jj$ electroweak signal. Lepton centrality is a quantity based on the kinematic signature of leptons and jets, given by:

$$\zeta = \min[\min(\eta_{l1}, \eta_{l2}) - \min(\eta_{j1}, \eta_{j2}), \max(\eta_{j1}, \eta_{j2}) - \max(\eta_{l1}, \eta_{l2})] \quad (7.1)$$

where $\eta_{l1}$ and $\eta_{l2}$ are the leading and subleading lepton pseudorapidity and $\eta_{j1}$ and $\eta_{j2}$ are the leading and subleading jet pseudorapidity. This equation is used to determine the position of leptons relative to the tagging jets in $\eta$. If $\zeta > 0$ both leptons are found to be within the tagging jets in $\eta$, however if $\zeta < 0$ one or both of the leptons have a larger $\eta$ than the closest tagging jet.

The following sections present the events yields that were obtained after all selection cuts were applied, the calculated significances for each of the four scenarios and the $\eta$ distributions for the tagging jets and selected leptons. The impact of an extended inner tracking will be discussed with respect to the ability to reject jets originating from pileup as well as the ability to reconstruct leptons in the forward regions. In addition the effect a forward muon-tagger was investigated by increasing the $p_T$ threshold for loose muons. Lastly, an additional diboson background sample was implemented into the analysis and the updates significances with the new total background contribution will be presented.

## 7.2 Results

To assess the sensitivity of the $W^{\pm}W^{\pm}jj$-EW measurement with the future ATLAS detector the significance of the signal, $Z_\sigma$, can be calculated. The signal significance is determined from the number of estimated signal events and background events, denoted as $N_{sig}$ and $N_{bkg}$ respectively, assuming that the number of events follow a Poissonian distribution. An estimated background uncertainty of $\sigma_B$ =15% must also be taken into account. The signal significance can then be calculated with the following equation [10]:

$$Z_\sigma = \sqrt{2[(N_{sig} + N_{bkg}) \log \frac{N_{sig} + N_{bkg}}{B_0} + B_0 - N_{sig} - N_{bkg}] \frac{(N_{bkg} - B_0)^2}{\sigma_B^2}} \quad (7.2)$$

in which $B_0 = \frac{1}{2}(N_{bkg} - \sigma_B^2 + \sqrt{(N_{bkg} - \sigma_B^2)^2 + 4(N_{sig} + N_{bkg})\sigma_B^2})$.

The estimated precision on the signal strength, $\frac{\Delta\mu}{\mu}$, can be calculated in

TABLE 7.6: Final expected event yield for signal and background samples, after all selection cuts have been applied for each of the four tracking scenarios.

| Track confirmation range | Lepton $\|\eta\|$ range | $W^{\pm}W^{\pm}jj$ EW | $W^{\pm}W^{\pm}jj$ QCD | WZ QCD + EW | Total background |
|---|---|---|---|---|---|
| $\|\eta\|_{jet} \leq 2.5$ | $\|\eta\|_{e,\mu} \leq 2.7$ | 4763 | 303 | 2300 | 4451 |
| $\|\eta\|_{jet} \leq 3.8$ | $\|\eta\|_{e,\mu} \leq 2.7$ | 5390 | 324 | 2693 | 5158 |
| $\|\eta\|_{jet} \leq 3.8$ | $\|\eta\|_{e} \leq 4.0$, $\|\eta\|_{\mu} \leq 2.7$ | 5456 | 331 | 2684 | 5155 |
| $\|\eta\|_{jet} \leq 3.8$ | $\|\eta\|_{e,\mu} \leq 4.0$ | 5552 | 340 | 2455 | 4780 |

TABLE 7.7: Significances of the $W^{\pm}W^{\pm}jj$ measurement for individual channels as well as the combined significances for each of the four tracking scenarios.

| Track confirmation range | Lepton $\|\eta\|$ range | $Z_{\sigma}$ $ee$ | $e\mu$ | $\mu e$ | $\mu\mu$ | $Z_{\sigma}$ Combined |
|---|---|---|---|---|---|---|
| $\|\eta\|_{jet} \leq 2.5$ | $\|\eta\|_{e,\mu} \leq 2.7$ | 3.8 | 6.4 | 7.0 | 13 | 17 |
| $\|\eta\|_{jet} \leq 3.8$ | $\|\eta\|_{e,\mu} \leq 2.7$ | 3.7 | 6.2 | 6.9 | 13 | 16 |
| $\|\eta\|_{jet} \leq 3.8$ | $\|\eta\|_{e} \leq 4.0$, $\|\eta\|_{\mu} \leq 2.7$ | 3.8 | 6.3 | 7.1 | 13 | 16 |
| $\|\eta\|_{jet} \leq 3.8$ | $\|\eta\|_{e,\mu} \leq 4.0$ | 3.8 | 6.8 | 7.7 | 16 | 19 |

the following manner [10]:

$$\frac{\Delta\mu}{\mu} = \frac{\sqrt{N_{sig} + N_{bkg} + \Sigma_{i=0}^{bkg}(N_i\sigma_i)^2}}{N_{sig}} \tag{7.3}$$

where each of the background processes, the strong production of $W^{\pm}W^{\pm}jj$, WZ and the other combined backgrounds, are assumed to be correlated with the systematic uncertainty of $\sigma_i = 15\%$. Uncertainties due to MC statistics and theoretical modelling are not taken into account.

The next section presents the estimated significances of the $W^{\pm}W^{\pm}jj$-EW measurement as well as the precision of the measurement for each of the four, above-mentioned tracking scenarios, which had been calculated with the latest upgrade performance functions. Furthermore, the gain in significance as well as the precision obtained with the extended tracking system are presented and compared with respect to the nominal tracking scenario with a coverage up to $|\eta| \leq 2.7$.

### 7.2.1 Effect of an extended Inner Tracker

The final expected event yields for signal and background samples after all selection criteria have been applied are summarised in Table 7.6, where all channels have been combined. The significance and precision are calculated separately for each channel: $ee$, $e\mu$, $\mu e$ and $\mu\mu$ depending on the flavour of the leading or sub-leading lepton and then combined quadratically, shown in Tables 7.7 and 7.8. The total background is approximated by using each

TABLE 7.8: Estimated precisions of the $W^{\pm}W^{\pm}jj$ measurement for individual channels as well as the combined precision for each of the four tracking scenarios.

| Track confirmation range | Lepton $\lvert\eta\rvert$ range | $\frac{\Delta\mu}{\mu}$ $ee$ | $e\mu$ | $\mu e$ | $\mu\mu$ | $\frac{\Delta\mu}{\mu}$ Combined |
|---|---|---|---|---|---|---|
| $\lvert\eta\rvert_{jet} \leq 2.5$ | $\lvert\eta\rvert_{e,\mu} \leq 2.7$ | 18% | 11% | 10.0% | 6.2% | 4.6% |
| $\lvert\eta\rvert_{jet} \leq 3.8$ | $\lvert\eta\rvert_{e,\mu} \leq 2.7$ | 19% | 11% | 10.1% | 6.2% | 4.6% |
| $\lvert\eta\rvert_{jet} \leq 3.8$ | $\lvert\eta\rvert_{e} \leq 4.0$, $\lvert\eta\rvert_{\mu} \leq 2.7$ | 18% | 11% | 9.8% | 6.2% | 4.6% |
| $\lvert\eta\rvert_{jet} \leq 3.8$ | $\lvert\eta\rvert_{e,\mu} \leq 4.0$ | 18% | 10% | 9.0% | 5.1% | 4.0% |

channel's respective scale factor. Event yields by individual channel can be found in Appendix B.

A definite improvement can be seen in the significance of the $W^{\pm}W^{\pm}jj$-EW measurement as forward tracking first becomes available for jets, and then extending the tracking capabilities for electrons and muons up to $|\eta| \leq 4.0$. The extended $\eta$-coverage of the inner tracking system provides the ability to reject pileup jets in the forward region from jets that originated from the hard scatter events. In addition, the forward coverage provides the capacity to reconstruct forward leptons. Both of these two advantages contribute to the overall improvement of the $W^{\pm}W^{\pm}jj$-EW measurement

The $\eta$ distributions for the leading and sub-leading jets after all selection criteria have been applied, are shown in Figure 7.3, for the $W^{\pm}W^{\pm}jj$-EW signal sample together with the other contributing backgrounds. The solid colours in the histograms indicate the contributions of jets originating from hard scatter events, while on the other hand the hashed colours indicate the contributions due to pileup jets. A distinctive step in the signal sample is visible between $|\eta| = 2.5$ and $|\eta| = 3.8$. These ranges correspond to the availability of forward tracking for jets, which indicates the raised acceptance $p_T$ for jets in these regions. The ability to tag and reject forward pileup jets leads to the suppression of backgrounds containing jets.

The increased $\eta$-coverage for electrons and muons provides the ability to reconstruct leptons within a larger range of the detector, which can be seen in Figure 7.4. Additionally, there is an increased acceptance of additional leptons (Figure B.3), which consequently leads to a stronger third-lepton veto for events. For this reason, the third-lepton veto reduces a significant amount of background contributions, especially the dominant WZ process and other backgrounds containing three leptons. The suppression of these backgrounds can be seen in Figure 7.2, where the pseudorapidity distribution for leading and sub-leading leptons are shown before and after the third-lepton veto cut.

The effect of the different tracking scenarios on the signal and background yields, the significance and the precision of the measurement are shown

TABLE 7.9: Variations on the signal and background yields, signal significance, measurement precision obtained with the upgraded detector, with respect to the current detector.

| | Signal variation | Background variation | $Z_\sigma$ variation | $\frac{\Delta\mu}{\mu}$ variation |
|---|---|---|---|---|
| Pileup rejection | +12% | +14% | -1.1% | +1.1% |
| Additional lepton veto | +2.9% | -7.9% | +17% | -14% |
| Combine | +14% | +6.9% | +16% | -13% |

in Table 7.9. The cases with pileup rejection for forward jets and the extended lepton $\eta$ region are considered separately, as well as the case where both are combined. Due to the jet $p_T$ threshold remaining at $30\,\mathrm{GeV}$ over a larger $\eta$ range, rejecting forward pileup jets with the JVT up to $\eta \leq 3.8$ improves the signal yield by 12%. However, increasing the signal also means that the total background yield will increase, which in turn leads to small variations in the signal significance and precision of the measurement. Processes that contain jets originating from the hard scatter vertex include the $W^{\pm}W^{\pm}jj$-EW process, as well as the $W^{\pm}W^{\pm}jj$-QCD and WZ. Although contributions from the $W^{\pm}W^{\pm}jj$-QCD process can be reduced with the rapidity requirement for jets, the strongest suppression for both the QCD and EW contributions of the WZ background comes from a third-lepton veto. This is due to the increased likelihood of reconstructing and detecting the third lepton from the WZ decay. Therefore, the combination of additional rejection of pileup jets as well as the the extended $\eta$ range for leptons is the best scenario.

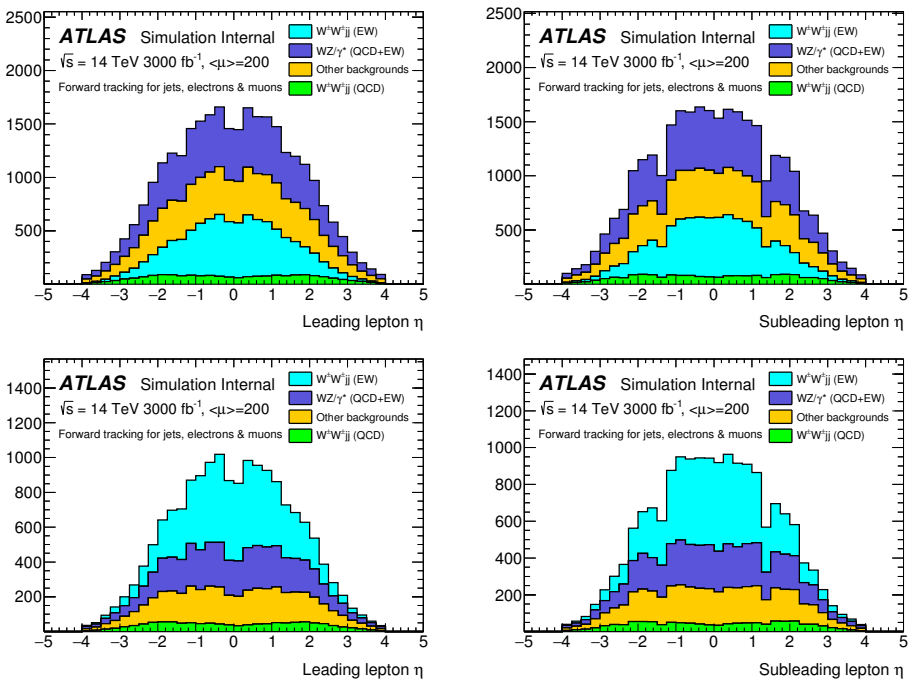


FIGURE 7.2: Pseudorapidity ($\eta$) distributions of the leading and sub-leading leptons before and after the the third-lepton veto for the extended $\eta$ range for leptons.

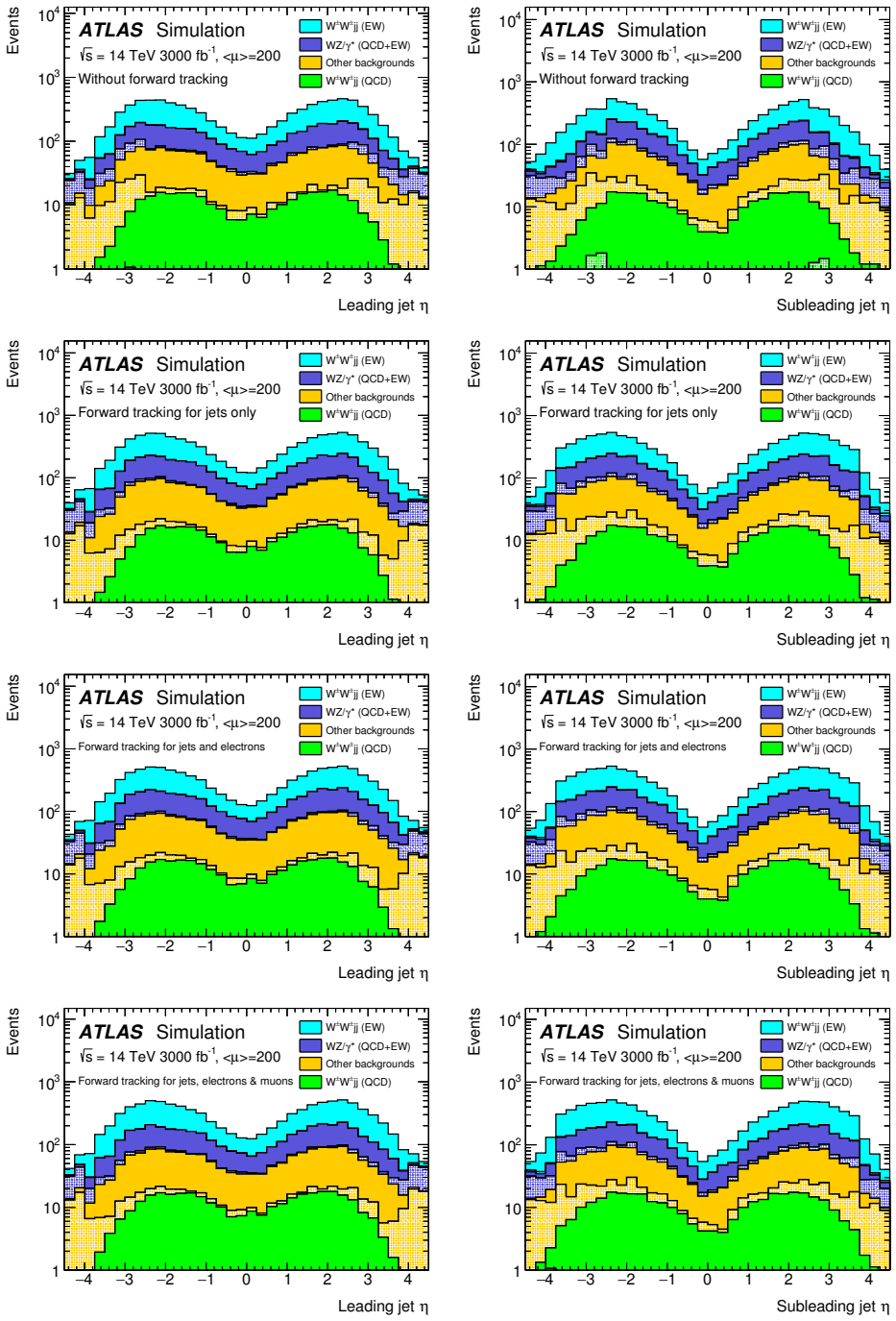


FIGURE 7.3: Pseudorapidity ($\eta$) distributions of the leading (left) and sub-leading (right) jets after all analysis criteria have been applied, for the four track confirmation scenarios. Solid lines indicate jets originating from hard scatter events, while the hashed fills indicate jets originating from pileup events.

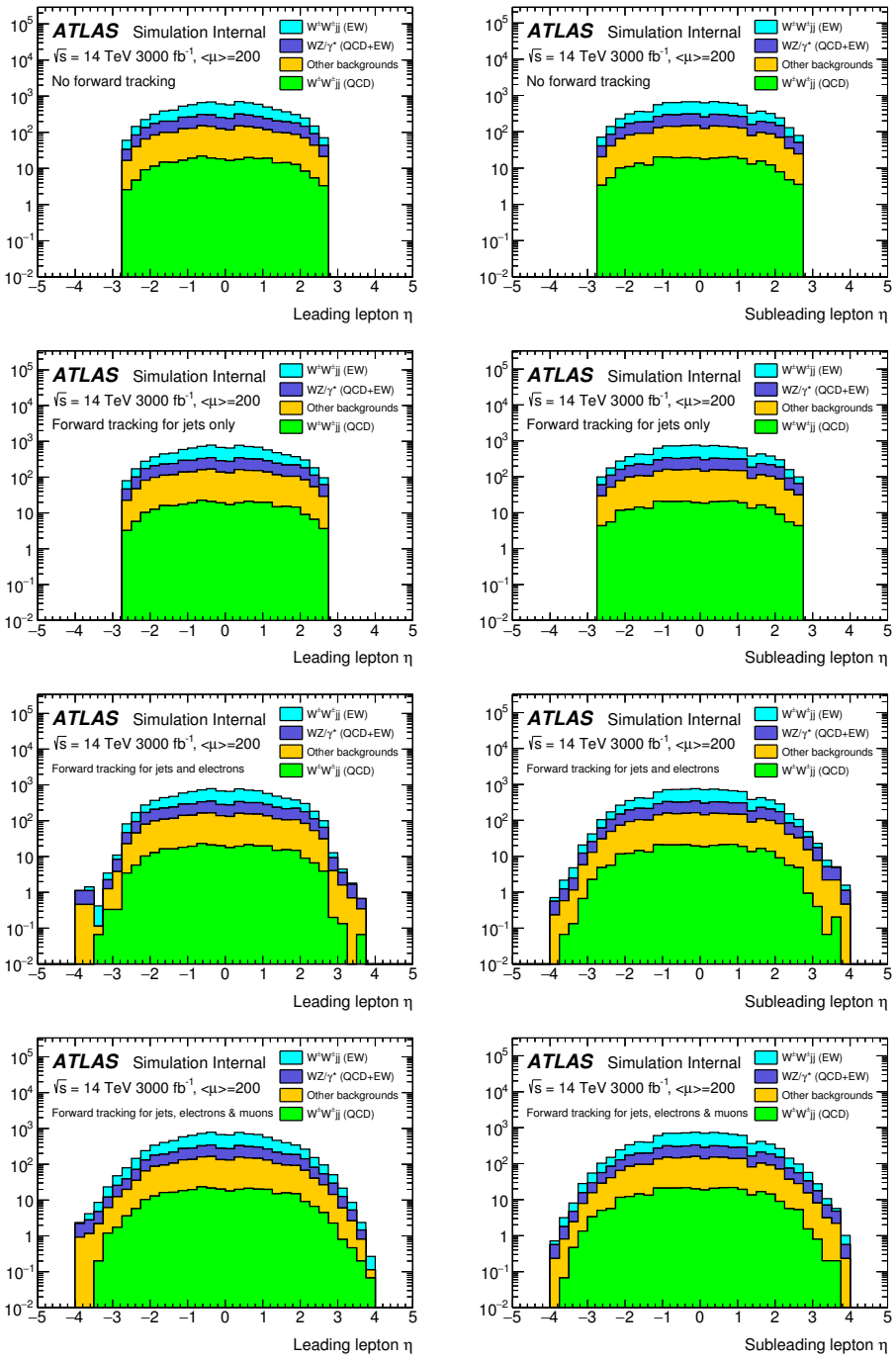


FIGURE 7.4: Pseudorapidity ($\eta$) distributions of the leading (left) and sub-leading (right) leptons after all analysis criteria have been applied, for the four track confirmation scenarios.

TABLE 7.10: Final expected event yield for signal and background samples after all selection cuts have been applied for each of the four tracking scenarios, where the loose muons with $p_T > 10$ have been preselected.

| Track confirmation range | Lepton $\|\eta\|$ range | $W^{\pm}W^{\pm}jj$ EW | $W^{\pm}W^{\pm}jj$ QCD | WZ QCD + EW | Total background |
|---|---|---|---|---|---|
| $\|\eta\|_{jet} \leq 2.5$ | $\|\eta\|_{e,\mu} \leq 2.7$ | 4780 | 305 | 2453 | 4717 |
| $\|\eta\|_{jet} \leq 3.8$ | $\|\eta\|_{e,\mu} \leq 2.7$ | 5409 | 326 | 2868 | 5459 |
| $\|\eta\|_{jet} \leq 3.8$ | $\|\eta\|_{e} \leq 4.0$, $\|\eta\|_{\mu} \leq 2.7$ | 5475 | 333 | 2858 | 5456 |
| $\|\eta\|_{jet} \leq 3.8$ | $\|\eta\|_{e,\mu} \leq 4.0$ | 5578 | 342 | 2663 | 5138 |

TABLE 7.11: Final expected event yield for signal and background samples after all selection cuts have been applied for each of the four tracking scenarios, where the loose muons with $p_T > 15$ have been preselected.

| Track confirmation range | Lepton $\|\eta\|$ range | $W^{\pm}W^{\pm}jj$ EW | $W^{\pm}W^{\pm}jj$ QCD | WZ QCD + EW | Total background |
|---|---|---|---|---|---|
| $\|\eta\|_{jet} \leq 2.5$ | $\|\eta\|_{e,\mu} \leq 2.7$ | 4792 | 305 | 2657 | 5066 |
| $\|\eta\|_{jet} \leq 3.8$ | $\|\eta\|_{e,\mu} \leq 2.7$ | 5423 | 326 | 3095 | 5850 |
| $\|\eta\|_{jet} \leq 3.8$ | $\|\eta\|_{e} \leq 4.0$, $\|\eta\|_{\mu} \leq 2.7$ | 5489 | 334 | 3087 | 5850 |
| $\|\eta\|_{jet} \leq 3.8$ | $\|\eta\|_{e,\mu} \leq 4.0$ | 5595 | 343 | 2933 | 5602 |

### 7.2.2 Effect of varying the loose muon $p_T$ threshold

The effect of a very forward muon-tagger was investigated by varying the acceptance $p_T$ threshold for the loose muons, for each of the four considered tracking scenarios. Three cases are considered namely, $p_T = 6$, 10 and 15 GeV, where $p_T > 6$ GeV is the nominal acceptance for loose muons. Figure 7.5 shows the changes in signal significances with respect to the increased $p_T$ threshold for each of the four tracking scenarios. In addition, the significances for each individual channel for each of the considered tracking scenarios are shown in Figure B.1. These plots indicate that the signal significances decrease rapidly when the $p_T$ threshold is raised, due to the fact that an increased amount of events pass the third-lepton veto. From Tables 7.10 and 7.11, which show the total signal and event yields after all selection cuts have been applied, it can be seen that for several cases the total background contributions are slightly higher than the total event yield for signal. This is especially true for the WZ background processes, which were suppressed in the previous results by the third-lepton veto selection cut.

Although the extended $\eta$-range enables the third-lepton veto cut to suppress the total background contribution for the $p_T > 10$ GeV case, the significance of the measurement is still reduced by 10% with respect to the nominal case of $p_T > 6$ GeV. With respect to the previous results shown in Table 7.6, the total signal yield only improves by a small margin of 0.5%, while the background contribution increases by a much larger amount of 7%.

For the case where the acceptance threshold for loose muons has been raised

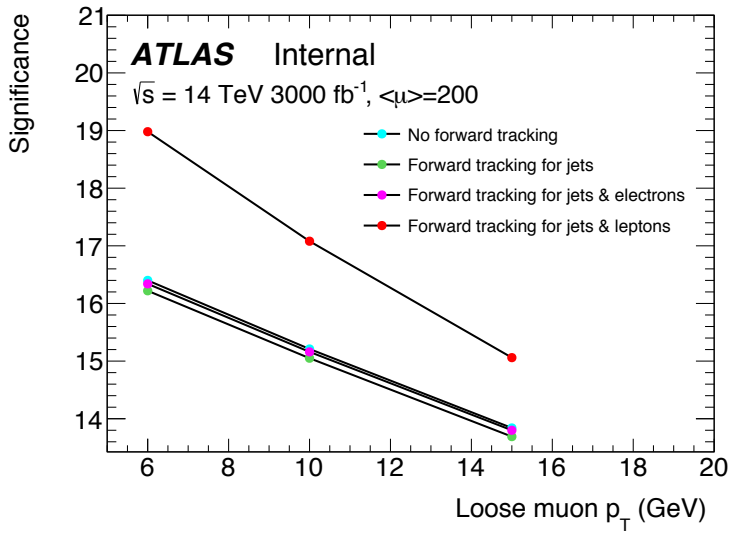


FIGURE 7.5: Effect of varying the loose muon $p_T$ on the combined signal significance for each of the four scenarios.

to $p_T > 15\,\text{GeV}$, the total background contribution dominates over the signal event yield for every all of the considered tracking scenarios. This increase of the total background event yield leads to a severe decrease of the significance of the $W^{\pm}W^{\pm}jj$-EW measurement.

### 7.2.3 Addition of the ZZ background process

Since very few MC samples have been produced at $\sqrt{s} = 14\,\text{TeV}$, the only suitable MC sample that was obtained was a ZZ + jets sample. In the $8\,\text{TeV}$ the total background contribution from the ZZ + jets process was low relative to the non-prompt and charge conversion backgrounds and had a negligible effect in the $8\,\text{TeV}$ analysis. Therefore, this thesis investigated whether the background process from this process would still be negligible at $\sqrt{s} = 14\,\text{TeV}$. This ZZ + jets sample is generated in a similar manner as the WZ + jets samples that was described in Section 7.1.1. The analysis was performed again with this new, additional sample and the final events, significances and precision of the measurements are summarised in Tables 7.12, 7.13 and 7.14.

TABLE 7.12: Final expected event yield for signal and background samples, after all selection cuts have been applied for each of the four tracking scenarios.

| Track confirmation range | Lepton $\lvert\eta\rvert$ range | $W^{\pm}W^{\pm}jj$ EW | $W^{\pm}W^{\pm}jj$ QCD | WZ QCD + EW | ZZ background | Total |
|---|---|---|---|---|---|---|
| $\lvert\eta\rvert_{jet} \leq 2.5$ | $\lvert\eta\rvert_{e,\mu} \leq 2.7$ | 4763 | 303 | 2300 | 77 | 4583 |
| $\lvert\eta\rvert_{jet} \leq 3.8$ | $\lvert\eta\rvert_{e,\mu} \leq 2.7$ | 5390 | 324 | 2693 | 87 | 5308 |
| $\lvert\eta\rvert_{jet} \leq 3.8$ | $\lvert\eta\rvert_{e} \leq 4.0$, $\lvert\eta\rvert_{\mu} \leq 2.7$ | 5456 | 331 | 2684 | 87 | 5304 |
| $\lvert\eta\rvert_{jet} \leq 3.8$ | $\lvert\eta\rvert_{e,\mu} \leq 4.0$ | 5552 | 340 | 2455 | 74 | 4906 |

TABLE 7.13: Significances of the $W^{\pm}W^{\pm}jj$ measurement for individual channels as well as the combined significances for each of the four tracking scenarios with the additional sample.

| Track confirmation range | Lepton $\|\eta\|$ range | $Z_\sigma$ | | | | $Z_\sigma$ |
|---|---|---|---|---|---|---|
| | | $ee$ | $e\mu$ | $\mu e$ | $\mu\mu$ | Combined |
| $\|\eta\|_{jet} \leq 2.5$ | $\|\eta\|_{e,\mu} \leq 2.7$ | 3.7 | 6.2 | 7.0 | 13 | 16 |
| $\|\eta\|_{jet} \leq 3.8$ | $\|\eta\|_{e,\mu} \leq 2.7$ | 3.6 | 6.1 | 6.7 | 13 | 16 |
| $\|\eta\|_{jet} \leq 3.8$ | $\|\eta\|_e \leq 4.0$, $\|\eta\|_\mu \leq 2.7$ | 3.7 | 6.2 | 6.9 | 13 | 16 |
| $\|\eta\|_{jet} \leq 3.8$ | $\|\eta\|_{e,\mu} \leq 4.0$ | 3.7 | 6.6 | 7.5 | 16 | 19 |

TABLE 7.14: Estimated precisions of the $W^{\pm}W^{\pm}jj$ measurement for individual channels as well as the combined precision for each of the four tracking scenarios with the additional sample.

| Track confirmation range | Lepton $\|\eta\|$ range | $\frac{\Delta\mu}{\mu}$ | | | | $\frac{\Delta\mu}{\mu}$ |
|---|---|---|---|---|---|---|
| | | $ee$ | $e\mu$ | $\mu e$ | $\mu\mu$ | Combined |
| $\|\eta\|_{jet} \leq 2.5$ | $\|\eta\|_{e,\mu} \leq 2.7$ | 19% | 11% | 10.0% | 6.2% | 4.6% |
| $\|\eta\|_{jet} \leq 3.8$ | $\|\eta\|_{e,\mu} \leq 2.7$ | 19% | 11% | 10.2% | 6.3% | 4.7% |
| $\|\eta\|_{jet} \leq 3.8$ | $\|\eta\|_e \leq 4.0$, $\|\eta\|_\mu \leq 2.7$ | 19% | 11% | 9.9% | 6.3% | 4.6% |
| $\|\eta\|_{jet} \leq 3.8$ | $\|\eta\|_{e,\mu} \leq 4.0$ | 19% | 10% | 9.1% | 5.1% | 4.0% |

Despite small variations in the significance and precision of the measurement for individual channels, the overall combined values remain unchanged. Only a small number of events from the ZZ sample remain after all selection criteria have been applied. This is again due to the excellent pileup rejection, however a significant amount of events from the ZZ process is suppressed by the di-jet selection criteria. In combination with the third-lepton veto which plays a part in rejecting the additional leptons originating from the ZZ decay, the final contribution from this process is negligible when compared to the contributions from the WZ and $W^{\pm}W^{\pm}jj$-QCD processes.

This result is to be expected, since the ZZ background process had a small contribution to the total background composition in the signal region observed by the $8\,\mathrm{TeV}$ analysis. Figure 7.6 exhibits the di-jet invariant mass distribution after all selection have been applied, since this distribution gives an approximation of the possible signal region at $14\,\mathrm{TeV}$ for the $W^{\pm}W^{\pm}jj$-EW measurement.

## 7.3 VBS studies at future colliders

Other particle colliders currently in multiple stages of development may also study VBS processes in the future. Currently, the ILC is planning the commission of a promising candidate, a linear electron-positron collider which will operate at $\sqrt{s} = 500\,\mathrm{GeV}$ up to $1\,\mathrm{TeV}$ [134]. The advantage of an electron-positron collider at a lower energy is that VBS processes could be measured more precisely with reduced backgrounds originating from

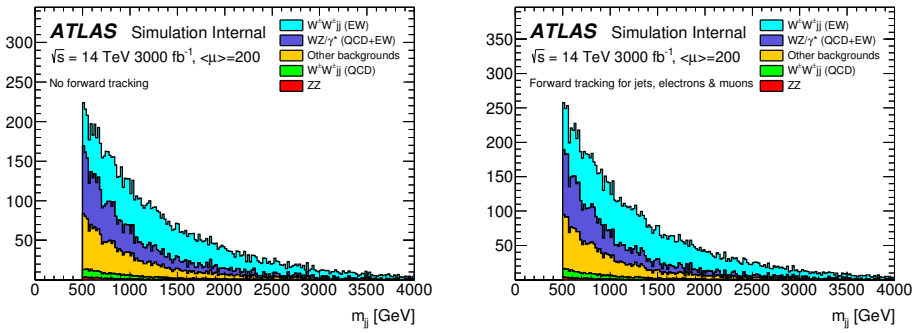


FIGURE 7.6: Di-jet invariant mass ($m_{jj}$) distributions for the case without forward tracking as well as the case where forward tracking is available for jets and leptons, after all analysis criteria have been applied.

hadronic activity. Therefore, it would provide a complementary measurement to that of the LHC. Additionally, a phenomenological study [135] has also investigated the prospects of a VBS measurement with a muon-muon collider at an energy of $\sqrt{s} = 4\,\text{TeV}$, which would provide a measurement in a jet-free environment above the energy range proposed by the ILC. A possible interesting study using this collider would be to investigate the diboson distributions in the $VVjj$ final states. More recently, another study highlighted the promising features of VBS processes in an environment of a future hadron collider operating at an energy of $\sqrt{s} = 100\,\text{TeV}$ [136]. The study of VBS processes at unprecedented energies would provide opportunities to investigate Beyond Standard Model physics in the electroweak sector.

# Chapter 8

# Conclusion

The thesis investigated the $W^{\pm}W^{\pm}jj$-EW measurement in two very different environments of the LHC, as well as the upgrade of the MS which would greatly enhance the $W^{\pm}W^{\pm}jj$-EW measurement during Run III and the HL-LHC. Firstly, this thesis studied the upgrade of the MS with a main focus on the assembly of sTGC chambers for the NSW. Since the assembly procedure for the assembly of these chambers has not yet been finalised, a proposed procedure that was developed as a summer student project at CERN through discussions with many experts was outlined. Particularly, a few of the more complicated steps in the process, requiring great care, was highlighted. A few resources necessary during the assembly of sTGC chambers including teams of specialists trained to perform various tasks, specialised equipment and storage space for wedges in different stages of development was discussed. Finally, the estimated storage space requirements for crates of quadruplets, as well as completed sTQC chambers was summarised.

Secondly, $28\,\mathrm{fb}^{-1}$ of $pp$ collision data at a centre of mass energy of $13\,\mathrm{TeV}$, collected by the current ATLAS detector, was considered. This thesis focussed on studying the $b$-tagged control region of this process, which is used to test the MC and data-driven estimations of the fake lepton background, dominated by events from the $t\bar{t}$ process. The poor MC modelling of the non-prompt processes in the $b$-tagged control region was investigated by defining a "mod tight" selection with no isolation requirements applied to the leading and sub-leading leptons. The effect of the isolation requirement was studied. It was found that a low fraction of events originates from the $t\bar{t}$ process in the $\mu\mu$ channel of this control region. Upon further investigation, it was determined that the majority of sub-leading leptons originating from the $t\bar{t}$ process in the $\mu\mu$ channel fail the imposed isolation requirements. The MC event record was then investigated and it was observed that in the tight + loose sample the largest background contribution is due to the $t\bar{t}$ and single top processes, in which the leading leptons originate from W bosons and the sub-leading leptons originate from B mesons. On the other hand, it was found that the $t\bar{t}+V$ process is the dominant process in the nominal $b$-tagged control region with the selection of two tight leptons. The isolation requirement therefore suppresses leptons originating from the $t\bar{t}$ and single top processes, however the suppression is the most sever in the muon channel.

With the addition of the isolation requirement for leptons, the the discrepancy between data and MC becomes even worse in the $b$-tagged control

region, especially since the MC is underestimated with respect to the data. This observation suggests that even though the isolation requirement suppresses the MC non-prompt backgrounds quite well, this is not the case for the data. Hence the poor agreement between data and MC in the $b$-tagged control region. Further studies of the $b$-tagged control region are still ongoing at the time of the writing of this thesis.

Lastly, $3000\,\mathrm{fb}^{-1}$ of simulated $pp$ collisions data at a centre of mass energy of $14\,\mathrm{TeV}$ with the future, upgraded ATLAS detector was considered. Extending the pseudorapidity coverage of various sub-detectors from 2.7 to within 4.0 will provide increased reconstruction capabilities of candidate physics objects, therefore greatly enhancing the $W^{\pm}W^{\pm}jj$-EW measurement. Particularly, the extension of the Inner Detector tracker in the forward regions with a coverage up to $|\eta| \leq 4.0$, together with a very forward muon-tagger will provide increased acceptance of leptons as well as the ability to tag and reject pileup jets in these regions. With the addition of a very forward muon-tagger to the NSW, the ability to reconstruct and accept muons over a large pseudorapidity region will be provided.

The prospects of a $W^{\pm}W^{\pm}jj$-EW measurement was then investigated with a focus on the extension of the inner tracking system, as well as an additional case where a forward muon-tagger is available. Simulated data at $\sqrt{s} = 14\,\mathrm{TeV}$ and a total integrated luminosity of $L = 3000\,\mathrm{fb}^{-1}$ was used for the estimation of the final event yield for $W^{\pm}W^{\pm}jj$-EW. In addition simulated data was also used for the estimation of two of the main background contributions, namely the $W^{\pm}W^{\pm}jj$-QCD and the WZ + jets processes. Other processes that contribute toward background were estimated with scale factors calculated from the total background event yields of the $8\,\mathrm{TeV}$ $W^{\pm}W^{\pm}jj$-EW analysis.

The forward tracker provides an increased background rejection, due to excellent pileup rejection in the forward regions. In addition, the extended coverage for leptons enables the reconstruction and identification of leptons in the forward region, hence providing a more effective third-lepton veto. The sensitivity of the measurement was assessed by calculating the significance and the precision of the measurement for each of the considered tracking scenarios. These values were then compared to the nominal case where tracking is only available up to $|\eta| \leq 2.7$. The significance of the $W^{\pm}W^{\pm}$ scattering measurement at $\sqrt{s} = 14\,\mathrm{TeV}$ and a total integrated luminosity of $L = 3000\,\mathrm{fb}^{-1}$ was measured to be 16.4 standard deviations. It was determined that the significance improves by 16% by extending the Inner Detector tracker and including forward tracking for jets, electrons and muons up to a pseudorapidity of $|\eta| \leq 4.0$. In addition, the precision of the measurement was estimated to be 5%, however this value can also be improved by 14% with the increased pseudorapidity coverage.

The effect of a forward muon-tagger was further investigated by varying the $p_T$ acceptance threshold for loose muons. It was found that fewer muons were accepted leading to an increased amount of background events passing the third-lepton veto. Consequently, the significance of the measurement decreased rapidly from a significance of 19 for $p_T = 6\,\mathrm{GeV}$ to 15 for

$p_T = 15\,\mathrm{GeV}$ in the case where forward tracking is available for jets and both electrons and muons.

Lastly, an additional ZZ sample was implemented in the analysis, however the di-jet selection requirements sufficiently reduced the final event yield of this sample to have a negligible effect on the significance and precision of the measurement.

In brief, an extended tracker providing increased tracking and reconstruction capabilities for forward jets and leptons has the potential to considerably improve the future $W^{\pm}W^{\pm}jj$-EW measurement at the HL-LHC, which will lead to a greater understanding of electroweak symmetry breaking and possibly even physics beyond the Standard Model.

# Appendix A

# Storage space requirements for sTGC wedges

In this section the entire storage space requirements for crates of sTGC quadruplets, as well as the completed sTGC wedges are given.

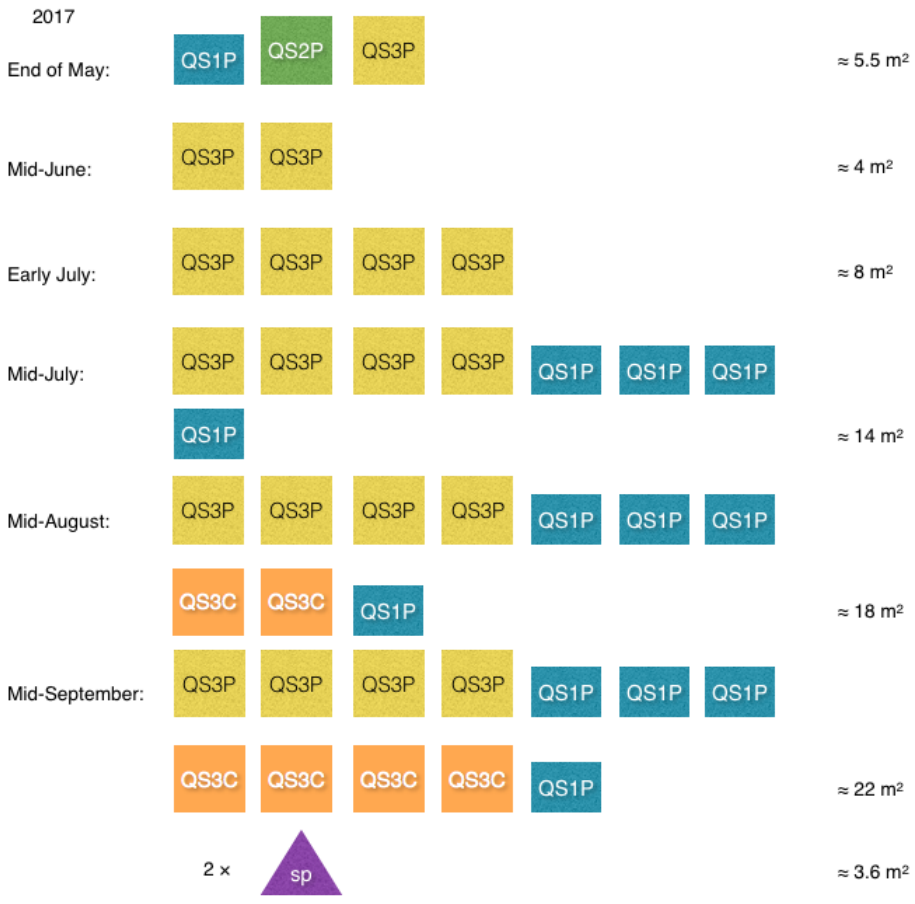


FIGURE A.1: Potential pile-up of quadruplet crates based on estimated arrival dates, while triangular shapes refer to completed sTGC wedges. The total approximated amount of necessary storage space is shown in the right-most column.

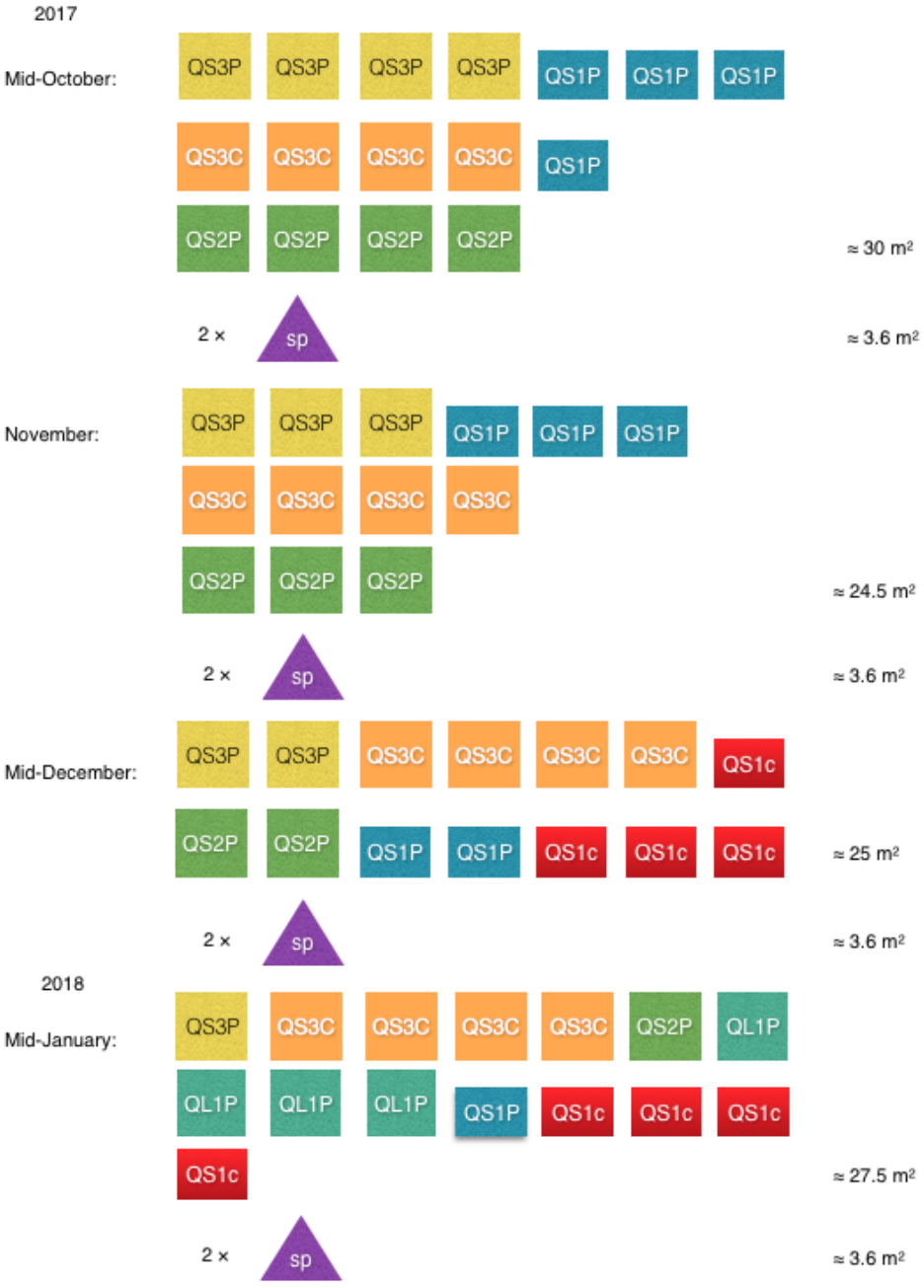


FIGURE A.2: Potential pile-up of quadruplet crates based on estimated arrival dates, while triangular shapes refer to completed sTGC wedges. The total approximated amount of necessary storage space is shown in the right-most column.

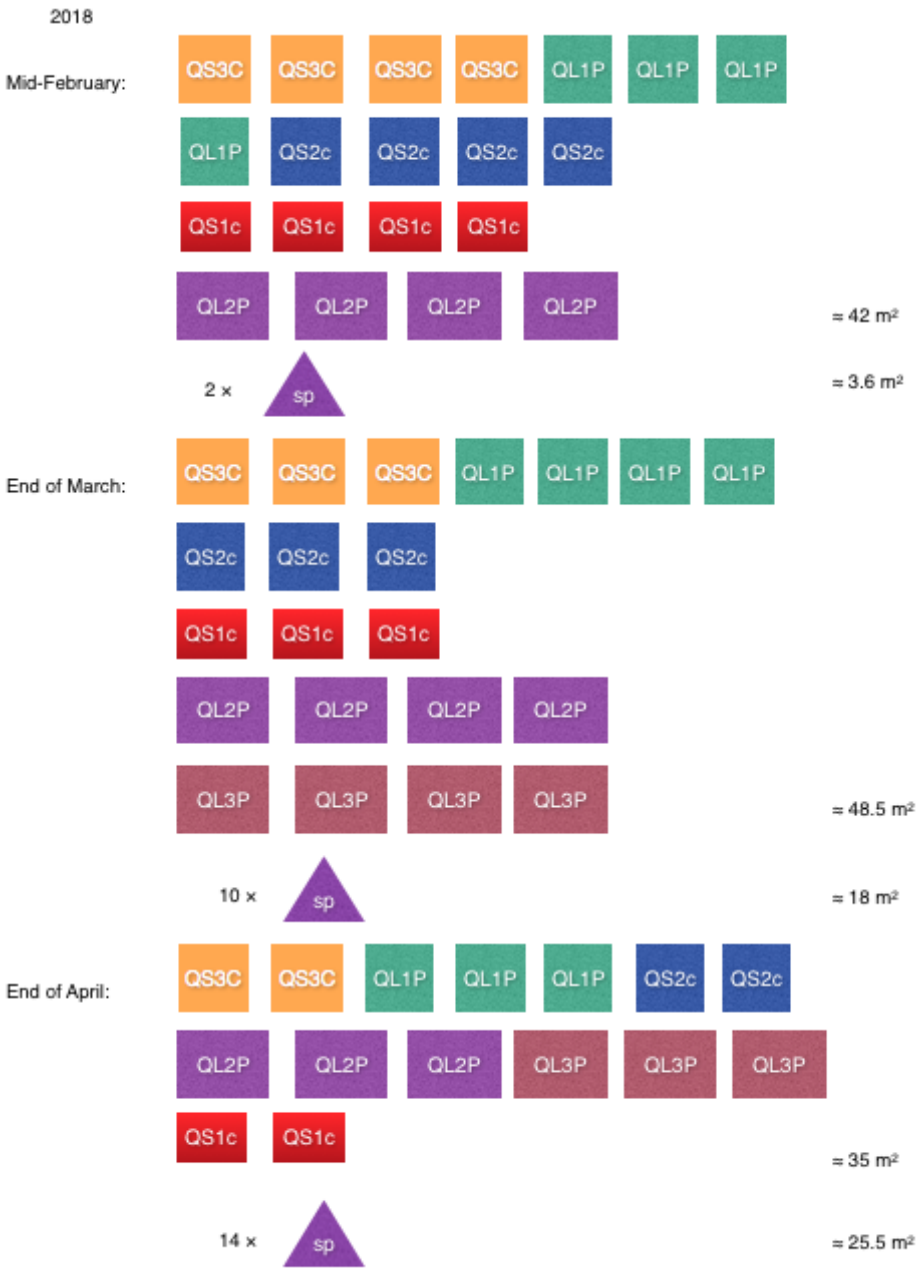


FIGURE A.3: Potential pile-up of quadruplet crates based on estimated arrival dates, while triangular shapes refer to completed sTGC wedges. The total approximated amount of necessary storage space is shown in the right-most column.


FIGURE A.4: Potential pile-up of quadruplet crates based on estimated arrival dates, while triangular shapes refer to completed sTGC wedges. The total approximated amount of necessary storage space is shown in the right-most column.

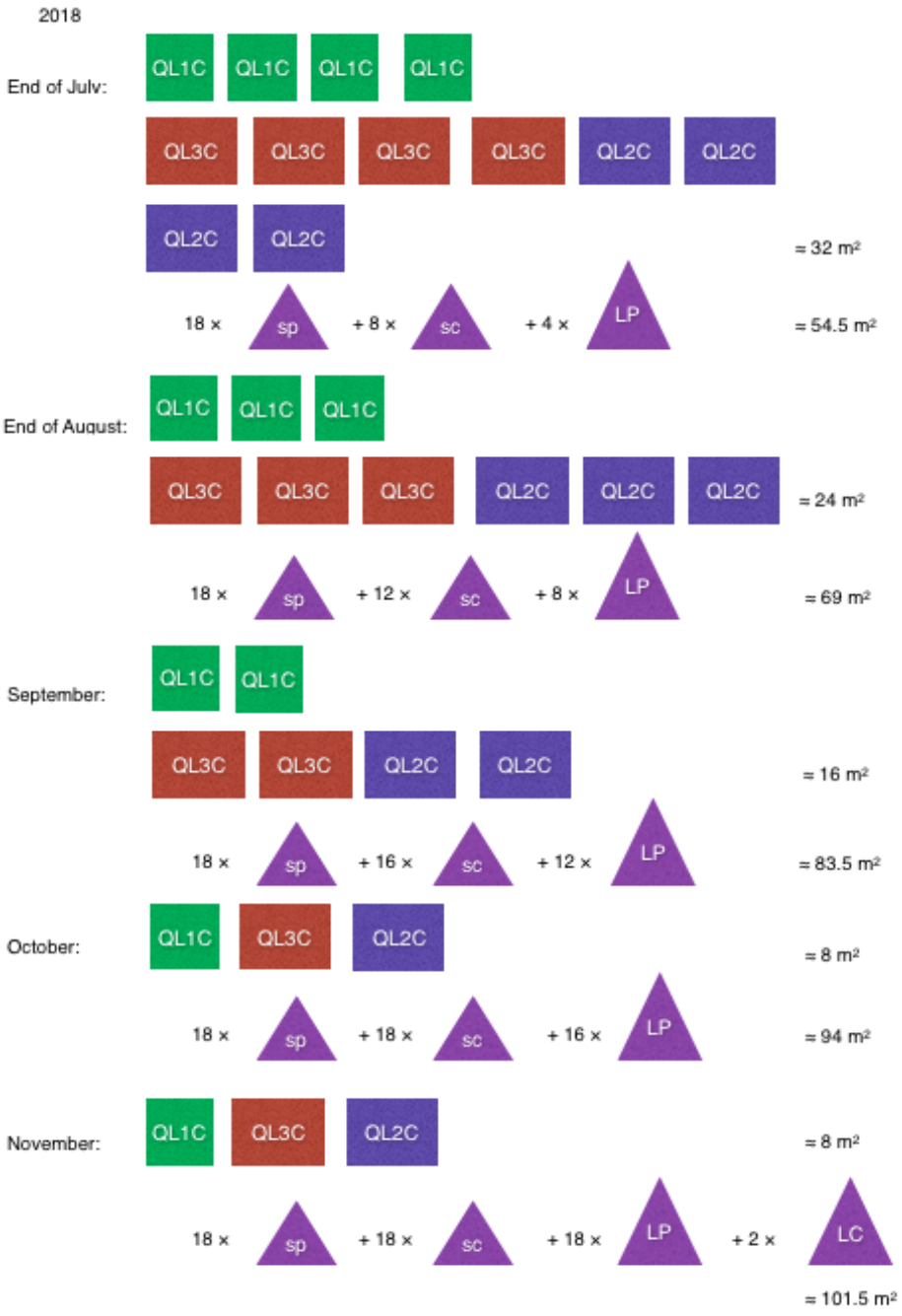


FIGURE A.5: Potential pile-up of quadruplet crates based on estimated arrival dates, while triangular shapes refer to completed sTGC wedges. The total approximated amount of necessary storage space is shown in the right-most column.

# Appendix B

# Additional material for HL-LHC $W^{\pm}W^{\pm}$ studies

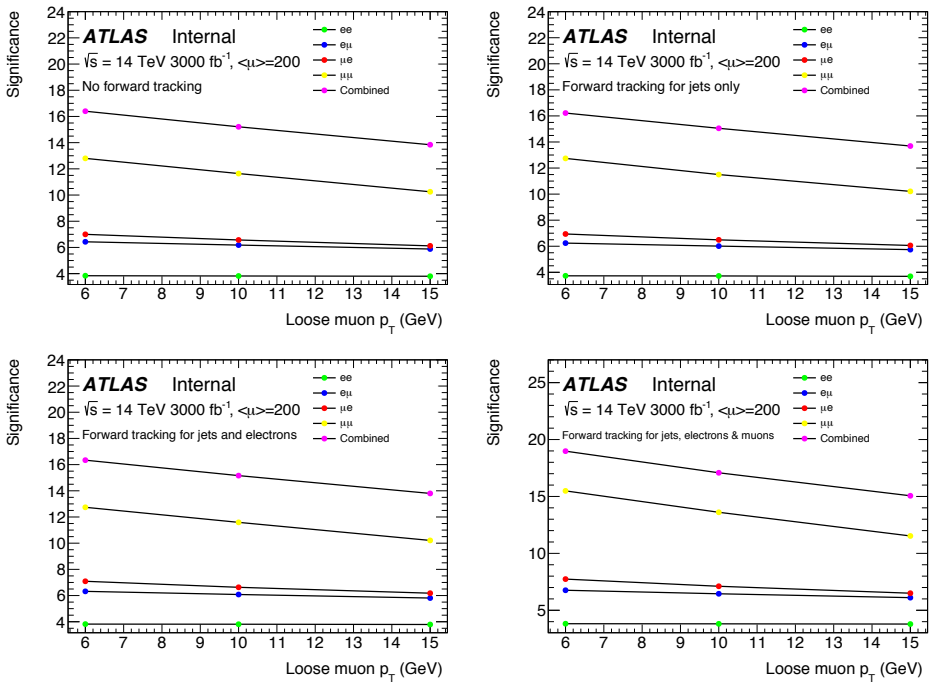


FIGURE B.1: Effect of varying the loose muon $p_T$ on the signal significance per channel for each of the four scenarios.

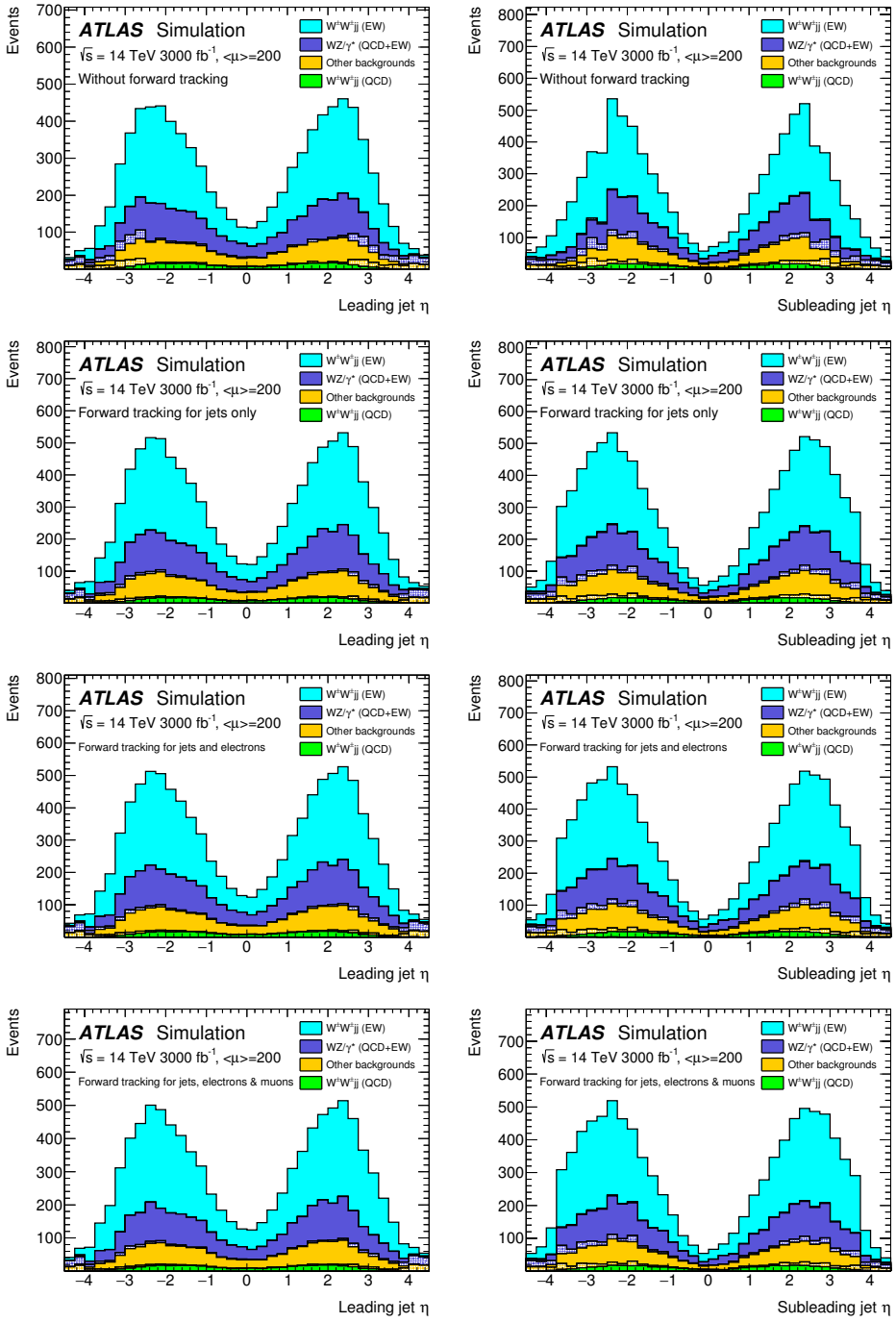


FIGURE B.2: Pseudorapidity ($\eta$) distributions of the leading (left) and sub-leading (right) jets after all analysis criteria have been applied, for the four track confirmation scenarios. Solid lines indicate jets originating from hard scatter events, while the hashed fills indicate jets originating from pileup events.

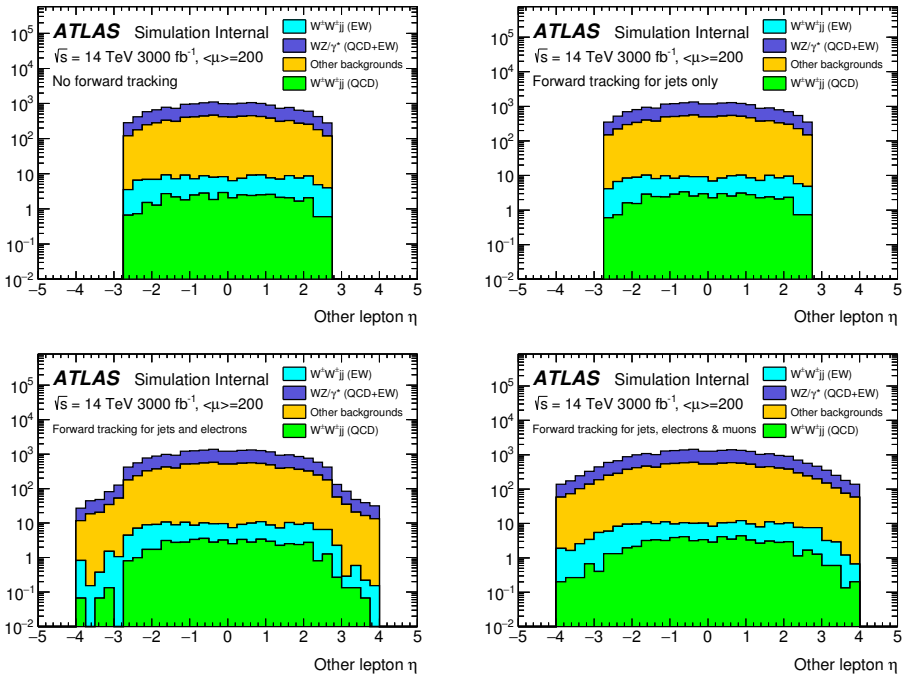


FIGURE B.3: Pseudorapidity ($\eta$) distributions of the loose leptons after all analysis criteria have been applied, for the four track confirmation scenarios.

TABLE B.1: Expected events yields foe signal and background for each individual channel after all selection criteria have with the four tracking scenarios.

| Channel | Track confirmation range | Lepton $\|\eta\|$ range | $W^{\pm}W^{\pm}jj$ EW | $W^{\pm}W^{\pm}jj$ QCD | WZ QCD + EW | ZZ background | Total |
|---|---|---|---|---|---|---|---|
| $ee$ | $\|\eta\|_{jet} \leq 2.5$ | $\|\eta\|_{e,\mu} \leq 2.7$ | 841 | 51 | 606 | 24 | 1165 |
| | $\|\eta\|_{jet} \leq 3.8$ | $\|\eta\|_{e,\mu} \leq 2.7$ | 943 | 55 | 343 | 28 | 1349 |
| | $\|\eta\|_{jet} \leq 3.8$ | $\|\eta\|_{e} \leq 4.0$, $\|\eta\|_{\mu} \leq 2.7$ | 970 | 58 | 706 | 27 | 1352 |
| | $\|\eta\|_{jet} \leq 3.8$ | $\|\eta\|_{e,\mu} \leq 4.0$ | 968 | 58 | 705 | 27 | 1350 |
| $e\mu$ | $\|\eta\|_{jet} \leq 2.5$ | $\|\eta\|_{e,\mu} \leq 2.7$ | 1329 | 80 | 684 | 23 | 1346 |
| | $\|\eta\|_{jet} \leq 3.8$ | $\|\eta\|_{e,\mu} \leq 2.7$ | 1498 | 86 | 804 | 26 | 1568 |
| | $\|\eta\|_{jet} \leq 3.8$ | $\|\eta\|_{e} \leq 4.0$, $\|\eta\|_{\mu} \leq 2.7$ | 1516 | 88 | 801 | 26 | 1566 |
| | $\|\eta\|_{jet} \leq 3.8$ | $\|\eta\|_{e} \leq 4.0$ | 1542 | 90 | 754 | 22 | 1481 |
| $\mu e$ | $\|\eta\|_{jet} \leq 2.5$ | $\|\eta\|_{e,\mu} \leq 2.7$ | 1077 | 70 | 491 | 19 | 990 |
| | $\|\eta\|_{jet} \leq 3.8$ | $\|\eta\|_{e,\mu} \leq 2.7$ | 1224 | 76 | 572 | 21 | 1142 |
| | $\|\eta\|_{jet} \leq 3.8$ | $\|\eta\|_{e} \leq 4.0$, $\|\eta\|_{\mu} \leq 2.7$ | 1247 | 78 | 567 | 21 | 1138 |
| | $\|\eta\|_{jet} \leq 3.8$ | $\|\eta\|_{e} \leq 4.0$ | 1262 | 79 | 515 | 18 | 1046 |
| $\mu\mu$ | $\|\eta\|_{jet} \leq 2.5$ | $\|\eta\|_{e,\mu} \leq 2.7$ | 1514 | 101 | 520 | 12 | 1082 |
| | $\|\eta\|_{jet} \leq 3.8$ | $\|\eta\|_{e,\mu} \leq 2.7$ | 1722 | 107 | 611 | 12 | 1248 |
| | $\|\eta\|_{jet} \leq 3.8$ | $\|\eta\|_{e} \leq 4.0$, $\|\eta\|_{\mu} \leq 2.7$ | 1720 | 107 | 611 | 12 | 1247 |
| | $\|\eta\|_{jet} \leq 3.8$ | $\|\eta\|_{e} \leq 4.0$ | 1777 | 112 | 482 | 7 | 1028 |

TABLE B.2: Variations of the signal and background, signal significance and measured precision obtained with the upgraded detector with respect to the current detector. Results for each individual channel are shown.

| | Channel | Signal variation | Background variation | $Z_{\sigma}$ variation | $\frac{\Delta_{\mu}}{\mu}$ variation |
|---|---|---|---|---|---|
| Pileup rejection | $ee$ | +11% | +14% | -2.7% | +2.7% |
| | $e\mu$ | +11% | +11% | -2.7% | +2.8% |
| | $\mu e$ | +12% | +13% | -0.8% | -7% |
| | $\mu\mu$ | +12% | +13% | -0.4% | +0.6% |
| Additional lepton veto | $ee$ | +2.6% | +0.1% | +2.5% | -2.5% |
| | $e\mu$ | +2.9% | -5.9% | +8.7% | -8% |
| | $\mu e$ | +3% | -9.2% | +12% | -10% |
| | $\mu\mu$ | +3.1% | -21% | +12% | -18% |
| Combined | $ee$ | +13% | +14% | -0.5% | +0.1% |
| | $e\mu$ | +14% | -5.3% | +5.8% | -5.4% |
| | $\mu e$ | +15% | +5.3% | +11% | -17% |
| | $\mu\mu$ | +15% | -5.3% | +22% | -18% |

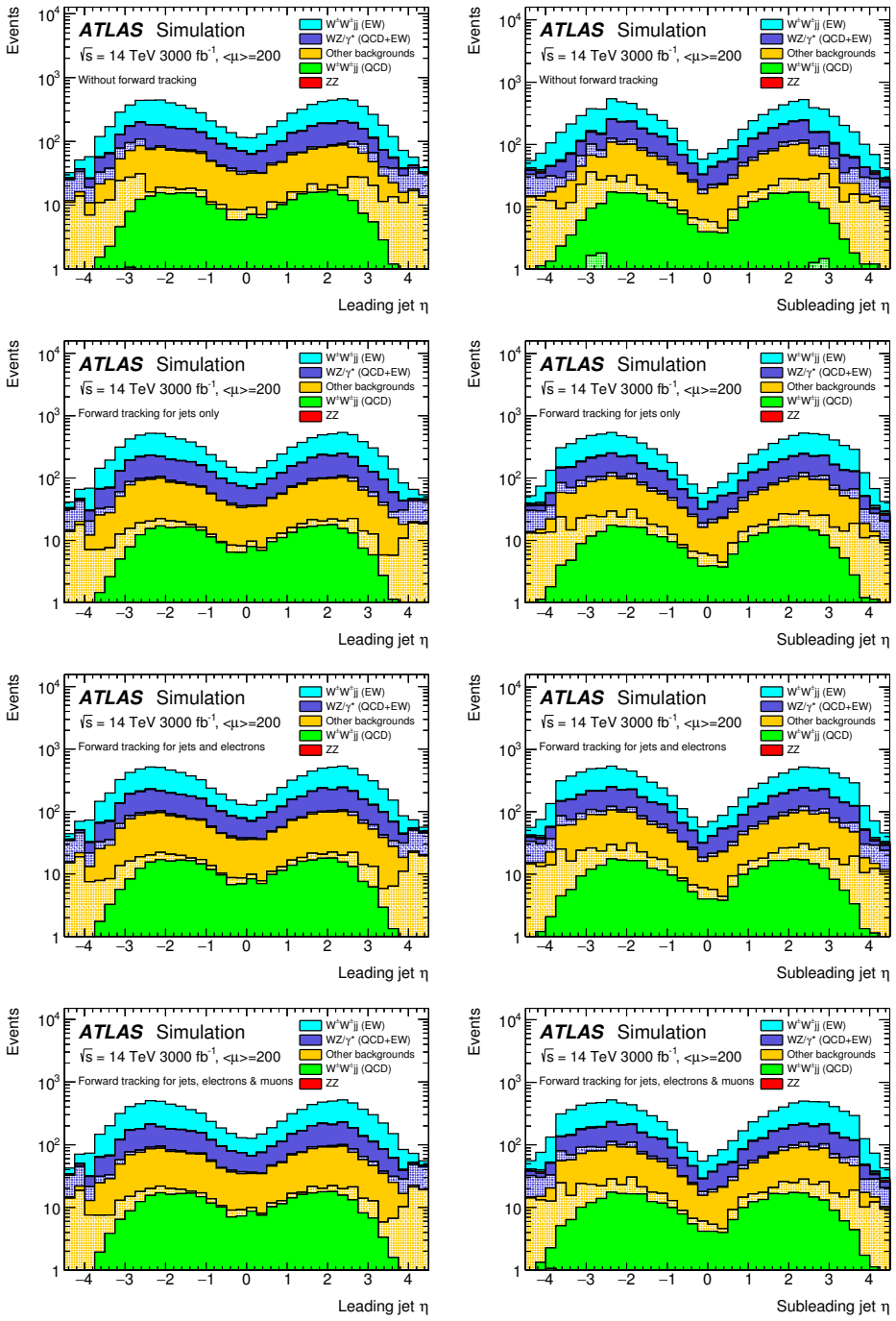


FIGURE B.4: Pseudorapidity ($\eta$) distributions of the leading (left) and sub-leading (right) jets after all analysis criteria have been applied, for the four track confirmation scenarios with the new ZZ sample. Solid lines indicate jets originating from hard scatter events, while the hashed fills indicate jets originating from pileup events.

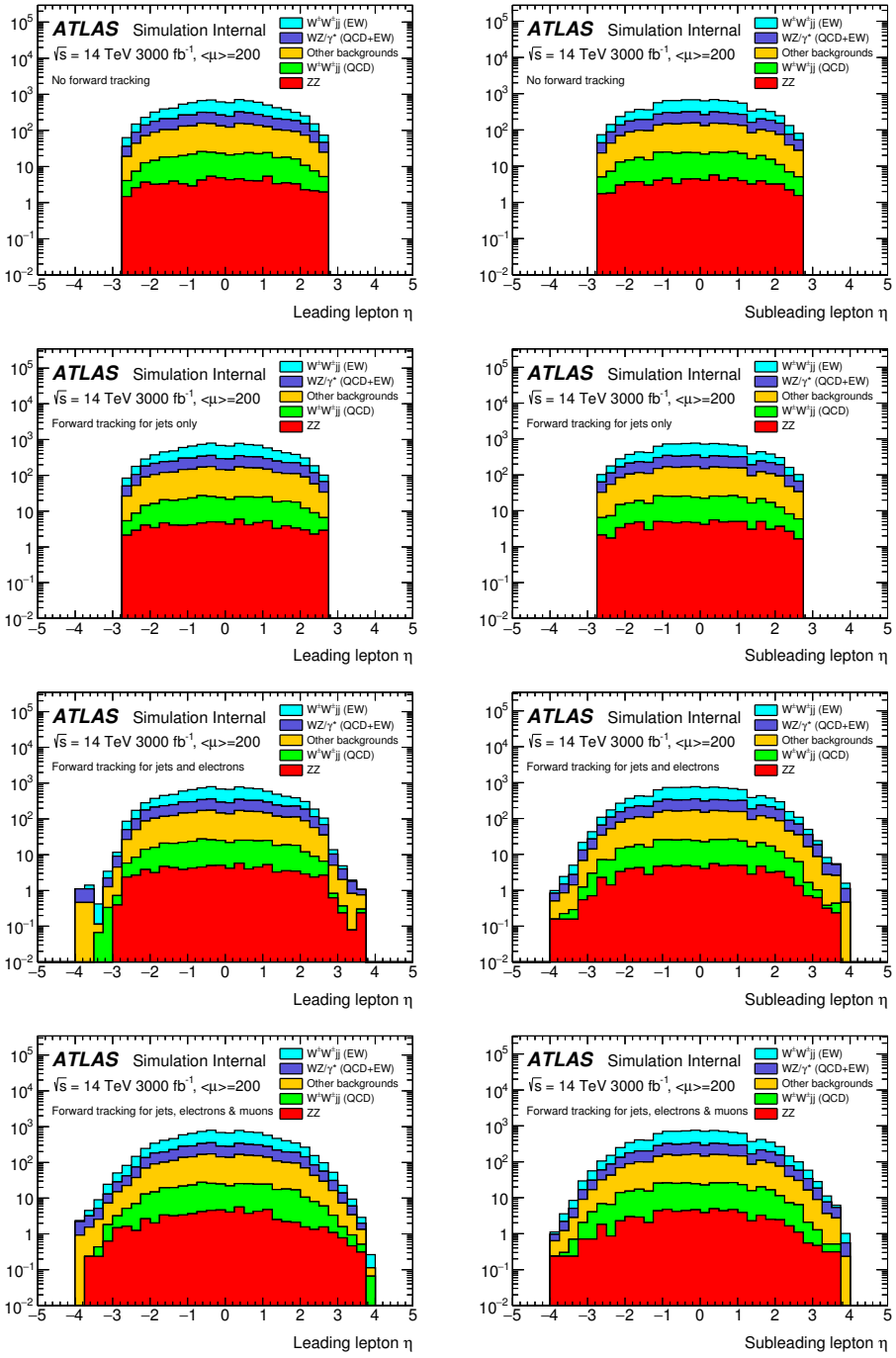


FIGURE B.5: Pseudorapidity ($\eta$) distributions of the leading (left) and sub-leading (right) leptons after all analysis criteria have been applied for the four track confirmation scenarios with the new ZZ sample.

# Appendix C

# Implementation of a logbook based on ELisA

ATLAS utilises and electronic logbook to share information concerning the maintenance and deployment of the ATLAS detector as well as its subsystems with members of the international collaboration. This electronic logbook for the information storage of ATLAS (ELisA) is a web based tool containing messages concerning the daily operation and data taking activities of the experiment [137]. The primary purpose of ELisA is to enable users to chronologically store information online as short, time-stamped messages known as "entries". The logbook has many additional features allowing users to edit or reply to these entries or even add additional attachments such as images. A few subsystems of the ATLAS experiment, notably the Fast TracKer (FTK) subsystem, requested the setup of their own ELisA based logbook for their private usage. Particularly, this new FTK logbook was required to be separated from the main ATLAS logbook and only have access to CERN's general public network.

The implementation, testing and modification of a new ELisA based logbook for the FTK sub-system was completed as a CERN Summer Student project during 2016. In the following sections the ELisA logbook will first be described, followed by the technology used to create this electronic logbook. Detailed discussions on the ELisA interface and the various implemented softwares can be found in [137] and [138].

## C.1 The ELisA interface

Since the stored log messages are useful to the entire ATLAS community, the ELisA logbook must meet a set of strict requirements. The web tool must enable fast and efficient manipulation of logbook entries with high availability and scalability. In order to enable users to quickly access stored information, the ELisA web interface makes use of several built-in features. Specifically, these built-in features allow users to easily browse entries, update or reply to relevant entries. Additional features enable the user to upload attachments, including images or documents, to entries. Conversely, these attachments can also be downloaded from existing entries. Furthermore, fast searches of log message can be performed by making use of a filter to select data in a singular column or all columns. The option to perform an advanced search also exists, where a custom query form can be filled in to select data in multiple columns or within a specific time interval. Additionally, the user can also format various aspects of the appearance of

the page by specifying the visible columns or by changing the length of the page. The user's changes are stored after the page has been redrawn with the use of cookies.

In order to use the logbook the user must be authenticated. The authentication procedure for usage in the General Private Network is based on CERN's Shibboleth Single Sign-On, while LDAP is used for usage within the restricted experiment network, ATLAS Control Network (ATCN). The user's credentials are verified with the relevant process based on the location from which the request originated from.

## C.2 Software

The ELisA web tool is based on the Spring Web MVC framework, which provides a Model-View-Controller architecture. The Model-View-Controller approach is a design pattern that separates different aspects of a web application (input logic, business logic and navigation logic), while maintaining a coupled link between these elements. Therefore, the Spring MVC approach [139] provides the necessary architecture used to build flexible and loosely coupled web applications. In this framework there are three main processes that are responsible for building a web application: models, views and controllers. Models are responsible for encapsulating application data. Views use information from the model object to render responses to the user, which creates the HTML output interpreted by a browser. Lastly, controllers process requests received from the user by building the model associated with the specific request and passing it to the view. The flow of request processing in a MVC web application has been illustrated in Figure C.1.

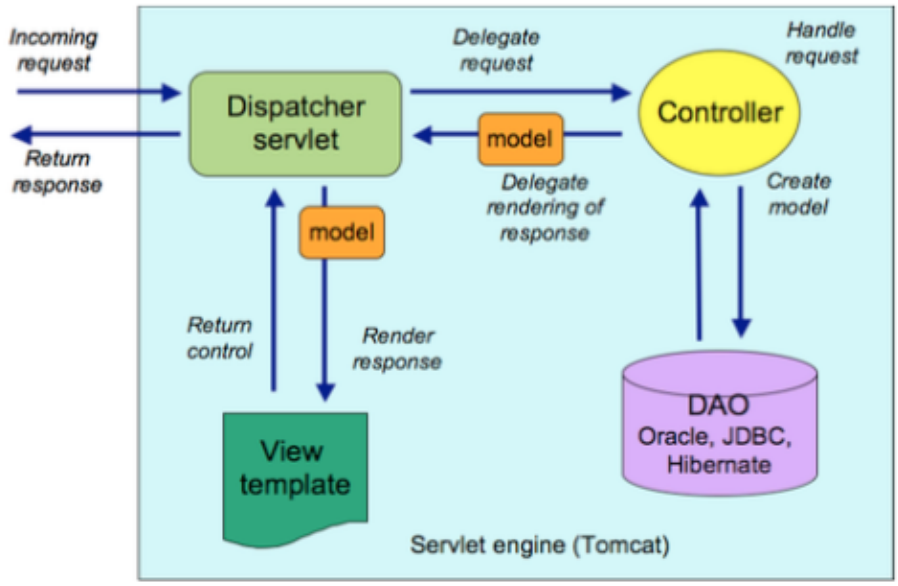


FIGURE C.1: Request processing in a Spring MVC [137].

First, a request sent to the Spring MVC framework is received by the DispatcherServlet, which handles all HTTP requests and responses. Once the DispatcherServlet has consulted the HandlerMapping, the appropriate Controller associated with the request is called. The Controller then processes the request and calls the appropriate service methods. Next, the Controller returns a Model object to the DispatcherServlet. Subsequently, the model objects are mapped to the messages in the logbook and are retrieved from an Oracle database by making use of Spring Data Access tools. In addition, the Model object is passed to a dedicated View by the DispatcherServlet. The final step in the flow is where the View uses the information from the model and returns the result to the user.

The front-end of ELisA is based on JSP technology [140] and makes use of JavaScript and jQueries for client-side processing and data manipulations. It has been designed to be effective, responsive and user-friendly. Improving the responsiveness of the web application is achieved by privileging client-side processing for message visualisation as well as making use of the Ajax method to retrieve data on client-request. The Ajax method achieves a more responsive, interactive web application by exchanging small amounts of data with the server in an asynchronous manner [141]. As a result, the entire page does not have to be reloaded every time changes have been made by the users. The servlet engine Apache Tomcat, which is an open source Java Servlet Container and implements several Java EE specifications [142], hosts the back-end server of the ELisA logbook.

## C.3 Implementation of the FTK logbook

### C.3.1 Setup

Use of the Spring framework requires the preparation of a development environment. Various Spring MVC framework tutorials usually provide detailed instructions to create this environment and the brief outline described below is based on a tutorial from Tutorialspoint [143].

The development environment can be set up by first downloading and installing the latest, or preferred, version of the Java Development Kit (JDK) from Oracle's Java site. It is crucial to correctly set the PATH and JAVA_HOME environment variables to refer to the directory containing Java. Then install Apache Commons Logging API by downloading the latest binaries from the Apache Commons Logging website. Once the binary distribution has been unpacked into a convenient location, care must be taken to set the CLASSPATH variable correctly. After installing the Apache libraries, the latest version of Eclipse IDE was setup. This can be done by downloading the latest binary distribution from the official Eclipse website and, once again, setting the PATH variable to refer to the appropriate directory. In addition, the Eclipse IDE package specifically for Java EE developers was installed for this project. Finally, the Spring Framework libraries may be installed, which are available from the Spring website. Once all these steps have been completed, the development environment would be setup correctly and the Spring framework may be used to start developing web applications.

The machine that will host the completed web application requires Apache Tomcat. A step-by-step guide[144] on installing Apache Tomcat on a Linux machine was closely followed. Apache Tomcat can be setup quite easily by downloading and extracting the latest binaries from the Apache project site. After unpacking the binaries, the CATALINA_HOME environment variable should be set to point to the main Tomcat directory. If the previous steps have been followed correctly, then Tomcat can be started with its startup script. The server is running correctly if the Tomcat welcome page can be accessed at http://localhost:8080/. Web applications can then be deployed by exporting the application as a WAR file to the web apps folder, which is located inside the Tomcat folder on the host machine. The application can then be accessed by connecting to the local host and selecting the application from the Tomcat manager page.

The FTK logbook was setup by creating two new accounts, ATLAS_ELISA_LOG and ATLAS_ELISA_CONF_LOG on the ATLR database. These accounts were specifically created to contain information regarding the data and the logbook configuration, respectively. The existing ELisA configurations were then imported to the ATLAS_ELISA_CONF_LOG in order to create a new, blank logbook that can be seen in Figure C.2. This logbook was first installed on a local machine and a test logbook was used to perform various tests to ensure that all the features of the ELisA tool were still functioning as expected. Various modifications were also made. Some of these modifications were done to increase the usability of the web application, while other modifications were specified by the FTK users to make the new logbook more relevant to the FTK subsystem. The following sections will discuss the testing and modifications of the new logbook.

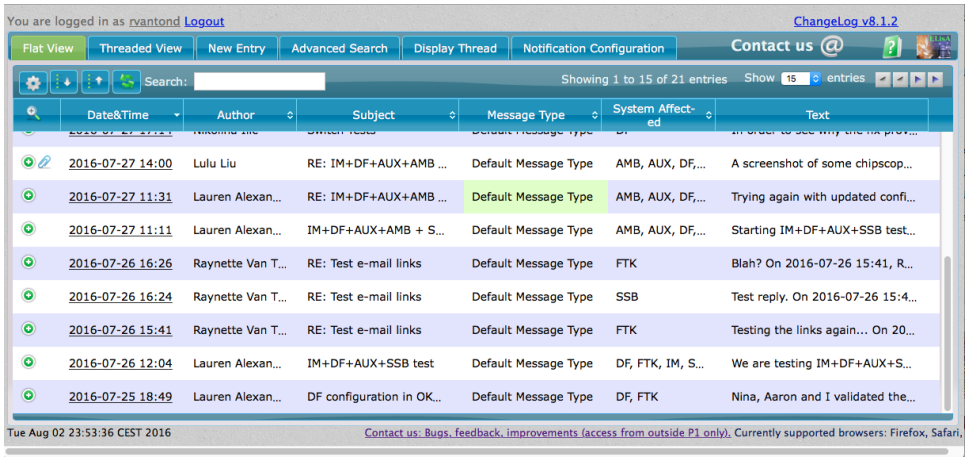


FIGURE C.2: Screenshot of the new ELisA based logbook.

### C.3.2 Testing and modifications

A blank test logbook was created, together with the new FTK logbook, to ensure that all the features of the ELisA web tool were still functioning as expected in the new logbook. This test logbook was used to check whether a


FIGURE C.3: Screenshot of the switch page.

user would still be able to add new entries to the logbook as well as editing, replying and adding attachments to the entries. Similarly, the test logbook was also used to ensure that the search and advanced search tools were still functioning correctly. Various modifications were made to the new logbook to avoid the possibility of users confusing the FTK logbook with the main ATLAS logbook. Additionally, specific changes were implemented for the logbook to provide specific features relevant only to the FTK system. The new modifications have been described in the following sections.

### Welcome page

A "switch page" was created for the user to select which logbook they wish to use. The page was also necessary to ensure that the user would not accidentally be redirected to a different logbook, for example the main ATLAS logbook, which would confuse the user or might result in entries being added to the incorrect logbook. The switch page was drawn which redirects users to a new welcome page after the user's credentials have been authenticated. The user selects the desired logbook via a choice of radio buttons and then clicking on the "Continue" button to proceed. Figure C.3 shows a screenshot of the switch page. Script, written in jsp and jstl, was used in order to redirect the user to the correct logbook once the "Continue" button had been clicked. In the case where a dedicated server machine, prepared by the FTK group, was being used to access the FTK logbook, then the switch page will not be drawn and the user will be automatically redirected to the FTK logbook.

### E-mail notification modifications

Various modifications were made to the e-mail notification settings of the logbook. Firstly, the recipients of the logbook's automatic e-mail notifications were changed in the case where the FTK logbook is being used. A notification from the FTK logbook would only be sent to the mailing list specified by the FTK users. In order to avoid confusion with notifications sent from the main ATLAS logbook, generally of interest to P1, an extra line was added to

the e-mail notification's subject line stating that the notification is from Lab 4. The logbook was then installed on a different machine to test whether the e-mail notifications were still sent to the proper recipients for each separate logbook that may be selected from the welcome page.

Since it is now possible to have many different logbooks installed on multiple machines, the URL links given in a notification should refer the reader to the correct logbook. These URL links give the option to display, edit or reply to the entry in the notification, as well as view attachments, and had to be changed to refer to the correct logbook. In Figure C.4 the default links for the main ATLAS logbook can be seen. Figure C.5 and Figure C.6 show the new links for the FTK logbook where it has been installed on a dedicated machine for FTK use, as well as a case where the logbook has been installed on a local machine. Note that the URL still points to the FTK logbook in the latter case.

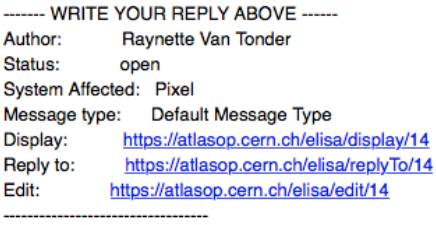


FIGURE C.4: Screenshot of the default e-mail notification links for the main ATLAS logbook.

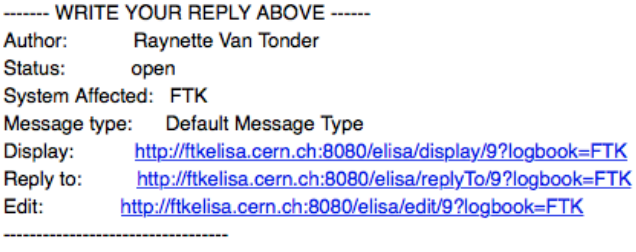


FIGURE C.5: Screenshot of the new e-mail notification links for the FTK logbook.

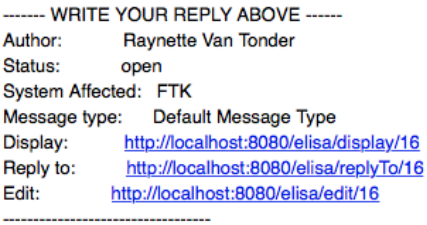


FIGURE C.6: Screenshot of the new e-mail notification links for the FTK logbook in the case where it has been installed on a local machine.

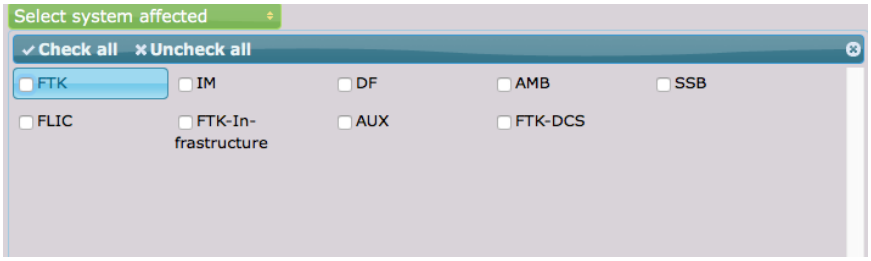


FIGURE C.7: Screenshot of the new SA relevant to the FTK.

### Relevant System Affected

As specified by the FTK users, new System Affected options relevant to the FTK were added to the ATLR database. The System Affected list was then filtered, depending on the logbook name, in order to only show the relevant System Affected to the user. Figure C.7 is a screenshot of the new System Affected options.

# References


[1] M. J. G. Veltman. "Second threshold in weak interactions". In: *Acta physica Polonica Series B* 8.6 (1977), pp. 475–492.

[2] B. W. Lee, C. Quigg, and H. B. Thacker. "Strength of weak interactions at very high energies and the higgs boson mass". In: *Physical Review Letters* 38.16 (1977), p. 883.

[3] B. W. Lee, C. Quigg, and H. B. Thacker. "Weak interactions at very high energies: The role of the Higgs-boson mass". In: *Physical Review D* 16.5 (1977), p. 1519.

[4] A. Alboteanu, W. Kilian, and J. Reuter. "Resonances and unitarity in weak boson scattering at the LHC". In: *Journal of High Energy Physics* 2008.11 (2008), p. 010.

[5] B. Zhu, P. Govoni, Y. Mao, et al. "Same sign WW scattering process as a probe of Higgs boson in $pp$ collision at $\sqrt{s} = 10\,\mathrm{TeV}$". In: *The European Physical Journal C* 71.1 (2011), pp. 1–5.

[6] ATLAS Collaboration. "Measurement of $W^{\pm}W^{\pm}$ vector-boson scattering and limits on anomalous quartic gauge couplings with the ATLAS detector". In: *arXiv preprint arXiv:1611.02428* (2016).

[7] ATLAS Collaboration. "Evidence for electroweak production of $W^{\pm}W^{\pm}jj$ in $pp$ collisions at $\sqrt{s} = 8\,\mathrm{TeV}$ with the ATLAS detector". In: *Physical Review Letters* 113.14 (2014), p. 141803.

[8] CMS Collaboration. "Study of vector boson scattering and search for new physics in events with two same-sign leptons and two jets". In: *Physical Review Letters* 114.5 (2015), p. 051801.

[9] CMS Collaboration. *Observation of electroweak production of same-sign W boson pairs in the two jet and two same-sign lepton final state in proton-proton collisions at 13 TeV*. Tech. rep. CMS-PAS-SMP-17-004. CMS private communication. Geneva: CERN, 2017.

[10] ATLAS Collaboration. *ATLAS Phase-II Upgrade Scoping Document*. Tech. rep. CERN-LHCC-2015-020. LHCC-G-166. Geneva: CERN, 2015.

[11] D. Cinca. *ATLAS Upgrades Towards the High Luminosity LHC: extending the discovery potential*. Tech. rep. ATL-COM-UPGRADE-2014-014. Geneva: CERN, 2014.

[12] R. P. Feynman. "Mathematical formulation of the quantum theory of electromagnetic interaction". In: *Physical Review* 80.3 (1950), p. 440.

[13] S. L. Glashow. "Partial-symmetries of weak interactions". In: *Nuclear Physics* 22.4 (1961), pp. 579–588.

[14] S. Weinberg. "A model of leptons". In: *Physical Review Letters* 19.21 (1967), p. 1264.

[15] A. Salam and J. C. Ward. "Electromagnetic and weak interactions". In: *Physics Letters* 13.2 (1964), pp. 168–171.

[16] H. D. Politzer. "Reliable perturbative results for strong interactions?" In: *Physical Review Letters* 30.26 (1973), p. 1346.

[17] D. J. Gross and F. Wilczek. "Ultraviolet behavior of non-abelian gauge theories". In: *Physical Review Letters* 30.26 (1973), p. 1343.

[18] G. 't Hooft and M. J. G Veltman. "Regularization and renormalization of gauge fields". In: *Nuclear Physics B* 44.1 (1972), pp. 189–213.

[19] F. Englert and R. Brout. "Broken symmetry and the mass of gauge vector mesons". In: *Physical Review Letters* 13.9 (1964), p. 321.

[20] P. W. Higgs. "Broken symmetries and the masses of gauge bosons". In: *Physical Review Letters* 13.16 (1964), p. 508.

[21] G. S. Guralnik, C. R. Hagen, and T. W. B. Kibble. "Global conservation laws and massless particles". In: *Physical Review Letters* 13.20 (1964), p. 585.

[22] *Wikipedia*. https://en.wikipedia.org. Accessed: 5-11-2016.

[23] C. Yang and R. L. Mills. "Conservation of isotopic spin and isotopic gauge invariance". In: *Physical Review* 96.1 (1954), p. 191.

[24] A. Salam and J. C. Ward. "Gauge theory of elementary interactions". In: *Physical Review* 136.3B (1964), B763.

[25] E. Noether. "Invariant variation problems". In: *Transport Theory and Statistical Physics* 1.3 (1971), pp. 186–207.

[26] ATLAS Collaboration. "Observation of a new particle in the search for the Standard Model Higgs boson with the ATLAS detector at the LHC". In: *Physics Letters B* 716.1 (2012), pp. 1–29.

[27] CMS Collaboration. "Observation of a new boson at a mass of 125 GeV with the CMS experiment at the LHC". In: *Physics Letters B* 716.1 (2012), pp. 30–61.

[28] D. Griffiths. *Introduction to Elementary Particles*. Portland, USA: WILEY-VCH, 2008.

[29] A. Bettini. *Introduction to Elementary Particle Physics*. Cambridge University Press, 2014.

[30] R. Mann. *An Introduction to Particle Physics and the Standard Model*. CRC press, 2011.

[31] Particle Data Group. "Review of Particle Physics". In: *Chinese Physics C* 38.9 (2014), p. 090001.

[32] N. Moser. "A sensitivity study for Higgs boson production in vector boson fusion in the $H \rightarrow \tau\tau \rightarrow lh + 3\nu$ final state with ATLAS". PhD thesis. University of Bonn, 2011.

[33] Y. Nambu. "Quasi-particles and gauge invariance in the theory of superconductivity". In: *Physical Review* 117.3 (1960), p. 648.

[34] J. Goldstone. "Field theories with "superconductor" solutions". In: *Il Nuovo Cimento* 19.1 (1961), pp. 154–164.

[35] S. D. Rindani. "Strong gauge boson scattering at the LHC". In: *Physics at the Large Hadron Collider*. Springer, 2009, pp. 145–155.

[36] J. Chang et al. "WW scattering in the era of post-Higgs-boson discovery". In: *Physical Review D* 87.9 (2013), p. 093005.

[37] K. Cheung, C. Chiang, and T. Yuan. "Partially strong WW scattering". In: *Physical Review D* 78.5 (2008), p. 051701.

[38] S. Mandelstam. "Determination of the pion-nucleon scattering amplitude from dispersion relations and unitarity. General theory". In: *Physical Review* 112.4 (1958), p. 1344.

[39] J. Bagger, V. Barger, K. Cheung, et al. "Strongly interacting WW system: Gold-plated modes". In: *Physical Review D* 49.3 (1994), p. 1246.

[40] D. Espriu and B. Yencho. "Longitudinal WW scattering in light of the "Higgs boson" discovery". In: *Physical Review D* 87.5 (2013), p. 055017.

[41] V. Barger, K. Cheung, T. Han, et al. "Strong $W^+W^+$ scattering signals at $pp$ supercolliders". In: *Physical Review D* 42.9 (1990), p. 3052.

[42] T. Gleisberg, S. Höche, F. Krauss, et al. "Event generation with SHERPA 1.1". In: *Journal of High Energy Physics* 2009.02 (2009), p. 007.

[43] P. Anger et al. *Same Sign $W^{\pm}W^{\pm}$ Production and Limits on Anomalous Quartic Gauge Couplings*. Tech. rep. ATLAS private communication. ATL-COM-PHYS-2013-990, CERN, Geneva, 2013.

[44] E. Accomando, A. Ballestrero, S. Bolognesi, et al. "Boson-boson scattering and Higgs production at the LHC from a six fermion point of view: four jets+ $l\nu$ processes at $\mathcal{O}(\alpha_{em}^6)$". In: *Journal of High Energy Physics* 2006.03 (2006), p. 093.

[45] M. Szleper. "The Higgs boson and the physics of WW scattering before and after Higgs discovery". In: *arXiv:1412.8367* (2014).

[46] O. S. Brüning et al. *LHC Design Report, volume 1: the LHC Main Ring*. Tech. rep. CERN-2004-003-V-1.

[47] ATLAS Collaboration. "The ATLAS experiment at the CERN Large Hadron Collider". In: *Journal of Instrumentation* 3.S08003 (2008).

[48] CMS Collaboration. "The CMS experiment at the CERN LHC". In: *Journal of Instrumentation* 3.08 (2008), S08005.

[49] ALICE Collaboration. "The ALICE experiment at the CERN LHC". In: *Journal of Instrumentation* 3.08 (2008), S08002.

[50] LHCb Collaboration. "The LHCb detector at the LHC". In: *Journal of Instrumentation* 3.08 (2008), S08005.

[51] G. Anelli et al. "The TOTEM experiment at the CERN Large Hadron Collider". In: *Journal of Instrumentation* 3.08 (2008), S08007.

[52] O. Adriani et al. "The LHCf detector at the CERN Large Hadron Collider". In: *Journal of Instrumentation* 3.08 (2008), S08006.

[53] *CERN Document Server*. http://cds.cern.ch/record/40525. Accessed: 7-11-2016.

[54] L. Evans and P. Bryant. "LHC machine". In: *Journal of Instrumentation* 3.08 (2008), S08001.

[55] G. Barr et al. *Particle Physics in the LHC Era*. Vol. 24. Oxford University Press, 2016, pp. 62–64.

[56] W. Herr and B. Muratori. "Concept of luminosity". In: *CERN Accelerator School: Intermediate Course on Accelerator Physics*. CERN. 2006, pp. 361–378.

[57] *CERN Document Server*. https://cds.cern.ch/record/1260465?ln=en. Accessed: 11-11-2016.

[58] *Luminosity results*. https://twiki.cern.ch/twiki/bin/view/AtlasPublic/LuminosityPublicResultsRun2. Accessed: 22-02-2017.

[59] M. Schott and M. Dunford. "Review of single vector boson production in $pp$ collisions at$\sqrt{s} = 7\,\mathrm{TeV}$". In: *The European Physical Journal C* 74.7 (2014), p. 2916.

[60] ATLAS Collaboration. *ATLAS insertable B-layer technical design report*. Tech. rep. ATLAS-TDR-019, 2010.

[61] M. Aharrouche et al. "Energy linearity and resolution of the ATLAS electromagnetic barrel calorimeter in an electron test-beam". In: *Nuclear Instruments and Methods in Physics Research Section A: Accelerators, Spectrometers, Detectors and Associated Equipment* 568.2 (2006), pp. 601–623.

[62] ATLAS Collaboration. *Tile Calorimeter Technical Design Report*. Tech. rep. CERN-LHCC-96-42, 1996.

[63] B. Dowler et al. "Performance of the ATLAS hadronic end-cap calorimeter in beam tests". In: *Nuclear Instruments and Methods in Physics Research Section A: Accelerators, Spectrometers, Detectors and Associated Equipment* 482.1 (2002), pp. 94–124.

[64] J. P. Archambault et al. "Energy calibration of the ATLAS liquid argon forward calorimeter". In: *Journal of Instrumentation* 3.02 (2008), P02002.

[65] ATLAS Collaboration. *New Small Wheel technical design report*. Tech. rep. CERN-LHCC-2013-006 ATLAS-TDR-020, 2013.

[66] N. Metropolis and S. Ulam. "The monte carlo method". In: *Journal of the American Statistical Association* 44.247 (1949), pp. 335–341.

[67] Particle Data Group. "Review of Particle Physics". In: *Phys. Rev. D* 86 (1 2012), p. 010001.

[68] M. A Dobbs et al. "Les Houches guidebook to Monte Carlo generators for hadron collider physics". In: *arXiv preprint hep-ph/0403045* (2004).

[69] A. Buckley et al. "General-purpose event generators for LHC physics". In: *Physics Reports* 504.5 (2011), pp. 145–233.

[70] T. Sjöstrand, . Mrenna, and P. Skands. "PYTHIA 6.4 physics and manual". In: *Journal of High Energy Physics* 2006.05 (2006), p. 026.

[71] T. Sjöstrand, S. Mrenna, and P. Skands. "A brief introduction to PYTHIA 8.1". In: *Computer Physics Communications* 178.11 (2008), pp. 852–867.

[72] T. Sjöstrand et al. "An introduction to PYTHIA 8.2". In: *Computer Physics Communications* 191 (2015), pp. 159–177.

[73] S. Gieseke, P. Stephens, and B. Webber. "New formalism for QCD parton showers". In: *Journal of High Energy Physics* 2003.12 (2004), p. 045.

[74] J. Alwall, P. Demin, S. Visscher, et al. "MadGraph/MadEvent v4: the new web generation". In: *Journal of High Energy Physics* 2007.09 (2007), p. 028.

[75] J. Alwall, R. Frederix, S. Frixione, et al. "The automated computation of tree-level and next-to-leading order differential cross sections, and their matching to parton shower simulations". In: *Journal of High Energy Physics* 2014.7 (2014), pp. 1–157.

[76] W. Kilian, T. Ohl, and J. Reuter. "WHIZARD:simulating multi-particle processes at LHC and ILC". In: *The European Physical Journal C-Particles and Fields* 71.9 (2011), pp. 1–29.

[77] M. Moretti, T. Ohl, and J. Reuter. "O'Mega: An Optimizing matrix element generator". In: *arXiv preprint hep-ph/0102195* (2001).

[78] K. Arnold et al. "VBFNLO: A parton level Monte Carlo for processes with electroweak bosons". In: *Computer Physics Communications* 180.9 (2009), pp. 1661–1670.

[79] S. Alioli et al. "A general framework for implementing NLO calculations in shower Monte Carlo programs: the POWHEG BOX". In: *Journal of High Energy Physics* 2010.6 (2010), p. 43.

[80] *CERN Document Server*. https://cds.cern.ch/record/1505342. Accessed: 14-01-2017.

[81] A. Sood. "Evidence for the production of two W bosons with the same electric charge and two jets in $20.3\,\mathrm{fb}^{-1}$ of $pp$ collisions at $\sqrt{s} = 8\,\mathrm{TeV}$ using the ATLAS detector". PhD thesis. University of California, Berkeley, 2014.

[82] ATLAS Collaboration. "Performance of primary vertex reconstruction in proton-proton collisions at $\sqrt{s} = 7\,\mathrm{TeV}$ in the ATLAS experiment". In: ATLAS-CONF-2010-069. 2010.

[83] G. P. Salam. "Towards jetography". In: *The European Physical Journal C* 67.3-4 (2010), pp. 637–686.

[84] M. Cacciari, G. P. Salam, and G. Soyez. "The anti-$k_t$ jet clustering algorithm". In: *Journal of High Energy Physics* 2008.04 (2008), p. 063.

[85] ATLAS Collaboration. "Jet energy measurement and its systematic uncertainty in proton–proton collisions at $\sqrt{s} = 7\,\mathrm{TeV}$ with the ATLAS detector". In: *The European Physical Journal C* 75.1 (2015), pp. 1–101.

[86] ATLAS Collaboration. "Jet energy scale measurements and their systematic uncertainties in proton-proton collisions at $\sqrt{s}$= 13 TeV with the ATLAS detector". In: *arXiv preprint arXiv:1703.09665* (2017).

[87] ATLAS Collaboration. "Commissioning of the ATLAS high-performance $b$-tagging algorithms in the $7\,\mathrm{TeV}$ collision data". In: ATLAS-CONF-2011-102. 2011.

[88] ATLAS Collaboration. "Calibration of the performance of $b$-tagging for $c$ and light-flavour jets in the 2012 ATLAS data". In: ATLAS-CONF-2014-046. 2014.

[89] ATLAS Collaboration. "Electron efficiency measurements with the ATLAS detector using 2012 LHC proton-proton collision data". In: *arXiv preprint arXiv:1612.01456* (2016).

[90] W. Lampl et al. *Calorimeter Clustering Algorithms*. Tech. rep. 2008.

[91] T. Cornelissen et al. *Concepts, design and implementation of the ATLAS New Tracking (NEWT)*. Tech. rep. 2007.

[92] ATLAS Collaboration. "Electron and photon energy calibration with the ATLAS detector using LHC Run 1 data". In: *The European Physical Journal C* 74.10 (2014), p. 3071.

[93] ATLAS Collaboration. *Electron identification measurements in ATLAS using $\sqrt{s} = 13\,\mathrm{TeV}$ data with $50\,\mathrm{ns}$ bunch spacing*. Tech. rep. ATL-PHYS-PUB-2015-041, 2015.

[94] ATLAS Collaboration. "Measurement of the muon reconstruction performance of the ATLAS detector using 2011 and 2012 LHC proton–proton collision data". In: *The European Physical Journal C* 74.11 (2014), pp. 1–34.

[95] ATLAS Collaboration. *Muon reconstruction performance in early Run II*. Tech. rep. ATL-PHYS-PUB-2015-037, 2015.

[96] S. Hassani et al. "A muon identification and combined reconstruction procedure for the ATLAS detector at the LHC using the (MUONBOY, STACO, MuTag) reconstruction packages". In: *Nuclear Instruments and Methods in Physics Research Section A* 572.1 (2007), pp. 77–79.

[97] ATLAS Collaboration. "Performance of missing transverse momentum reconstruction in ATLAS studied in proton-proton collisions recorded in 2012 at $8\,\mathrm{TeV}$". In: ATLAS-CONF-2013-082. 2013.

[98] ATLAS Collaboration. *Performance of missing transverse momentum reconstruction for the ATLAS detector in the first proton-proton collisions at at $\sqrt{s} = 13\,\mathrm{TeV}$*. Tech. rep. ATL-COM-PHYS-2015-710, 2015.

[99] C. A. Lee. "Measurement of track-based missing transverse momentum in proton-proton collisions at $\sqrt{s} = 8\,\mathrm{TeV}$ centre-of-mass energy with the ATLAS detector". PhD thesis. University of Johannesburg, 2014.

[100] B. Stelzer for the ATLAS Muon Collaboration. "The New Small Wheel Upgrade Project of the ATLAS experiment". In: *Nuclear and Particle Physics Proceedings* 273 (2016), pp. 1160–1165.

[101] "ECFA High Luminosity LHC Experiments Workshop: Physics and Technology Challenges. 94th Plenary ECFA meeting". In: (2013).

[102] ATLAS Collaboration. *Letter of Intent for the Phase-II Upgrade of the ATLAS Experiment*. Tech. rep. CERN-LHCC-2012-022. LHCC-I-023. Geneva: CERN, 2012.

[103] ATLAS Collaboration. *Studies of Vector Boson Scattering and Triboson Production with an Upgraded ATLAS Detector at a High-Luminosity LHC*. Tech. rep. ATL-PHYS-PUB-2013-006. Geneva: CERN, 2013.

[104] S. L. Barnes et al. *Summary Report on the Expected Impact of a Large Eta Detector in ATLAS on Standard Model Physics Analyses*. Tech. rep. ATL-COM-UPGRADE-2015-001. ATLAS private communication. Geneva: CERN, 2015.

[105] *The HL-LHC Project*. http://hilumilhc.web.cern.ch/about/hl-lhc-project. Accessed: 3-06-2017.

[106] ATLAS Collaboration. *Expected Performance of the ATLAS Inner Tracker at the High-Luminosity LHC*. Tech. rep. ATL-PHYS-PUB-2016-025. Geneva: CERN, 2016.

[107] S. Agostinelli, J. Allison, K. Amako, et al. "GEANT4-a simulation toolkit". In: *Nuclear instruments and methods in physics research section A: Accelerators, Spectrometers, Detectors and Associated Equipment* 506.3 (2003), pp. 250–303.

[108] ATLAS Collaboration. *Performance assumptions for an upgraded ATLAS detector at a High-Luminosity LHC*. Tech. rep. ATL-PHYS-PUB-2013-004, 2013.

[109] ATLAS Collaboration. *Performance assumptions based on full simulation for an upgraded ATLAS detector at a High-Luminosity LHC*. Tech. rep. ATL-PHYS-PUB-2013-009, 2013.

[110] R. Aleksan, P. Braun-Munzinger, P. Chomaz, et al. *Physics briefing book: input for the strategy group to draft the update of the European strategy for particle physics*. Tech. rep. CERN-ESG-005, 2013.

[111] U. Schnoor. "Vector Boson Scattering and electroweak production of two like-charge W Bosons and two jets at the current and future ATLAS detector". PhD thesis. IKTP TU Dresden, 2014.

[112] B. Bittner et al. "Tracking and Level-1 triggering in the forward region of the ATLAS Muon Spectrometer at sLHC". In: *Journal of Instrumentation* 7.01 (2012), p. C01048.

[113] E. Perez Codina for the ATLAS Muon Collaboration. "Small-strip Thin Gap Chambers for the muon spectrometer upgrade of the ATLAS experiment". In: *Nuclear Instruments and Methods in Physics Research Section A: Accelerators, Spectrometers, Detectors and Associated Equipment* 824 (2016), pp. 559–561.

[114] Y. Giomataris et al. "MICROMEGAS: a high-granularity position-sensitive gaseous detector for high particle-flux environments". In: *Nuclear Instruments and Methods in Physics Research Section A* 376.1 (1996), pp. 29–35.

[115] S. Majewski et al. "A thin multiwire chamber operating in the high multiplication mode". In: *Nuclear Instruments and Methods in Physics Research* 217.1 (1983), pp. 265–271.

[116] S. Dado et al. "A new high gain thin gap detector for the OPAL hadron calorimeter". In: *Nuclear Instruments and Methods in Physics Research Section A* 252.2-3 (1986), pp. 511–516.

[117] ATLAS Collaboration. "ATLAS Muon Spectrometer Technical Design Report". In: *CERN/LHCC* 97.22 (1997), p. 281.

[118] *sTGC assembly and testing manual*. VI. Maintained by Dr. I. Trigger. ATLAS-sTGC.

[119] V. Smakhtin et al. "Thin Gap Chamber upgrade for SLHC: Position resolution in a test beam". In: *Nuclear Instruments and Methods in Physics Research Section A* 598.1 (2009), pp. 196–200.

[120] I. Trigger. Private communication.

[121] L. Liu. "Evidence for electroweak production of $W^{\pm}W^{\pm}jj$ in proton-proton collisions at $\sqrt{s} = 8\,\mathrm{TeV}$ with the ATLAS detector at the LHC". PhD thesis. University of Michigan, 2015.

[122] D. W. Miller, A. Schwartzman, and D. Su. "Jet-vertex association algorithm". In: *ATL-COM-PHYS* 8 (2008), p. 2008.

[123] ATLAS Collaboration. "Performance of $b$-jet identification in the ATLAS experiment". In: *Journal of Instrumentation* 11.04 (2016), P04008.

[124] ATLAS Collaboration. "The ATLAS simulation infrastructure". In: *The European Physical Journal C* 70.3 (2010), pp. 823–874.

[125] H. Lai, M. Guzzi, J. Huston, et al. "New parton distributions for collider physics". In: *Physical Review D* 82.7 (2010), p. 074024.

[126] M. L. Mangano, F. Piccinini, M. Moretti, et al. "ALPGEN, a generator for hard multiparton processes in hadronic collisions". In: *Journal of High Energy Physics* 2003.07 (2003), p. 001.

[127] J. Pumplin, D. R. Stump, J. Huston, et al. "New generation of parton distributions with uncertainties from global QCD analysis". In: *Journal of High Energy Physics* 2002.07 (2002), p. 012.

[128] C. Gumpert. "Measurement of electroweak gauge boson scattering in the channel $pp \to W^{\pm}W^{\pm}jj$ with the ATLAS detector at the Large Hadron Collider". PhD thesis. IKTP TU Dresden, 2014.

[129] X. O. Thusini. *Characterising the sources of fake leptons from top quarks in same sign W boson scattering with the ATLAS detector at* $13\,\mathrm{TeV}$. University of Cape Town. 2017.

[130] L. H. McConnell. *Suppression of the fake lepton background in same-sign W-boson scattering with the ATLAS experiment*. University of Cape Town. 2017.

[131] ATLAS Collaboration. *Studies of vector boson scattering with an upgraded ATLAS detector at a High-Luminosity LHC*. Tech. rep. ATL-COM-PHYS-2012-1532, 2012.

[132] C. A. Lee et al. *Studies on the impact of an extended Inner Detector tracker on $W^{\pm}W^{\pm}$ scattering in pp collisions at the High-Luminosity LHC with the ATLAS experiment*. Tech. rep. ATL-COM-UPGRADE-2016-036. Geneva: CERN, 2016.

[133] D. Rainwater and D. Zeppenfeld. "Observing $H \to W(*)W(*) \to e^{\pm}\mu^{\mp}p_T$ in weak boson fusion with dual forward jet tagging at the CERN LHC". In: *Physical Review D* 60.11 (1999), p. 113004.

[134] G. Weiglein et al. "Physics interplay of the LHC and the ILC". In: *Physics Reports* 426.2 (2006), pp. 47–358.

[135] V. Barger et al. "Studying a strongly interacting electroweak sector via longitudinal gauge-boson scattering at a muon collider". In: *Physical Review D* 55.1 (1997), p. 142.

[136] B. Jager et al. "Physics Opportunities for Vector-Boson Scattering at a Future 100 TeV Hadron Collider". In: *arXiv preprint arXiv:1704.04911* (2017).

[137] A. Corso Radu, G. Lehmann Miotto, and L. Magnoni. “The electronic logbook for the information storage of ATLAS experiment at LHC (ELisA)”. In: *Journal of Physics: Conference Series*. Vol. 396. IOP Publishing. 2012, p. 012014.

[138] A. Corso Radu, L. Magnoni, and R. M. Garcia. “The ELisA facility-RESTful API and client libraries”. In: *2013 IEEE Nuclear Science Symposium and Medical Imaging Conference (2013 NSS/MIC)*. IEEE. 2013, pp. 1–4.

[139] *Spring Framework*. http://static.springsource.org. Accessed: 20-11-2016.

[140] H. Bergsten. *JavaServer Pages*. "O’Reilly Media", 2003.

[141] J. J. Garrett. *Ajax: A new approach to web applications*. http://adaptivepath.org/ideas/ajax-new-approach-web-applications. 2005.

[142] *Apache Tomcat*. http://tomcat.apache.org. Accessed: 20-11-2016.

[143] *Tutorialspoint Spring MVC Tutorial*. http://www.tutorialspoint.com/spring/index.htm. Accessed: 2-08-2016.

[144] *Mulesoft*. https://www.mulesoft.com/tcat/tomcat-linux. Accessed: 26-11-2016.